Petrophysical properties of deformation bands and their influence on fluid flow in carbonate grainstones: insights from the Maghlaq Fault, Malta.

Master thesis in Petroleum/Structural Geology

Heidi Synnøve Solli Fossmark

Department of Earth Science

University of Bergen

June, 2015

Abstract

Deformation bands are tabular, sub- centimeter thick zones, which accommodates shear and/or volumetric deformation. Only a few examples of deformation bands have been documented in porous carbonate rocks, and the knowledge about how petrophysical properties and fluid flow interacts in such settings is thus limited. Motivated by this, the current study focus on deformation bands found in carbonate grainstones in the hangingwall of an extensional fault on the southwestern coast of Malta, the Maghlaq Fault, in an attempt to elucidate their petrophysical properties and their dynamic effect on fluid flow by means of reservoir modeling and flow simulations. The studied deformation bands are hosted in the porous Globigerina Limestone Formation, where structural data were recorded along deformation band frequency scanlines to characterize the bands and their spatial distribution. Moreover, porosity and permeability were determined for both host rock and deformation bands using gas-transfer techniques and image analysis.

By applying an inflated modeling approach, deformation bands are represented by semi-discrete means, closely reproducing the observed spatial distribution pattern and structural geometries. Flow simulations of the inflated models, where deformation band permeability is the main variable tested, are compared to a reference case where deformation bands are absent. The results from the flow simulation show that increasing permeability contrast between host rock and deformation bands causes fluid flow complexity, reflected by variations in the shape and propagation speed of the waterfronts from the injection wells. In turn, slow water front propagation results in delayed water break-through in the production wells. With low initial host rock permeability, deformation bands have an effect on fluid flow even when the contrast of permeability between them and host rock is 1 order of magnitude. Alternatively, with high initial host rock permeability, the permeability contrast needs to be 2 orders of magnitude, or more, to significantly affect fluid flow across the grid. The results of the present study demonstrate that the inflated modeling approach is well suited to capture details of flow in the presence of small-scale flow baffles. Understanding how geological heterogeneity and fluid flow interacts in reservoirs is important for the prediction of flow and optimization of production strategies. Thus, the modeling approach presented herein can improve the incorporation of small-scale features into conventional sized reservoir models.

Acknowledgements

Bergen, 24th of May 2015

Heidi Synnøve Solli Fossmark

Heidi Synnøve Solli Fossmark

Table of contents

1. Introduction

1.1 Project framework

This study is one of two interrelated MSc projects investigating deformation bands in porous carbonate grainstones along the Maghlaq Fault, Malta. Together, the two projects aim to improve the knowledge of deformation bands in porous carbonate rocks in terms of the micro-deformation mechanisms involved in the development of the bands, their structural style, petrophysical properties and influence on fluid flow. Whereas this thesis focuses on the part that deals with the effect of deformation bands on petrophysical properties and their influence on fluid flow in carbonate reservoir rocks, the related sister MSc project (Elin Thorsheim) focuses on the deformation mechanisms, kinematics and origin of the bands. As such, these latter topics are beyond the scope of the present thesis.

1.2 Rationale

Strain localization due to failure in porous granular rocks results in characteristic millimeter- to centimeter thick tabular structures called deformation bands (Aydin 1978, Aydin & Johnson 1978). Deformation bands are generally associated with porosity and permeability reduction and are, therefore, relevant for the compartmentalization of hydrocarbon- or groundwater reservoirs (e.g Matthäi et al. 1998, Sternlof et al. 2006, Kolyukhin et al. 2010). However, in the geological literature the majority of the deformation bands are reported from porous siliciclastic rocks (Fossen et al. 2007, and references therein), and only a few deformation bands are described from porous carbonate rocks (e.g. Tondi et al. 2006, Tondi 2007, Rath et al. 2011, Antonellini et al. 2014). Carbonate rocks account for approximately half of the world´s hydrocarbon reserves, thus understanding how geological heterogeneity and fluid flow interacts in such settings is important for the prediction of flow and optimization of production strategies (e.g. Mazzullo 2004). Since seismic resolution normally is inadequate to reveal small-scale features, studies of outcrops analogues are essential to make predictions of subsurface reservoirs (Rotevatn et al. 2009a). Nonetheless, sub-centimeter deformation bands are well below the resolution of conventional field-scale reservoir models, and their implementation requires implicit representation with upscaled

permeabilities (e.g. Fachri et al. 2013a). However, such an approach does not fully resolve the orientation and distribution of deformation bands (Rotevatn et al. 2009b, Fachri et al. 2013a). The current study addresses aspects of the impact of deformation bands on fluid flow properties, and their implementation in flow models, by characterizing the deformation bands accommodated in extensionally faulted carbonate rocks, along the Maghlaq Fault, Malta. Specific aims and objectives are outlined in the following subsection.

1.3 Aims and Objectives

The main aims of this study are to better understand the impact of deformation bands on fluid flow in carbonate rocks and to improve the representation of deformation bands in geocellular reservoir models. Specifically, this study sets out to i) establish a method for (semi)discrete representation of small-scale heterogeneities in reservoir models, ii) assess the effect of deformation bands on reservoir permeability and porosity distribution and iii) quantify the dynamic effect of deformation bands on fluid flow. These aims are achieved through detailed outcrop investigation performed in the hangingwall of the extensional Maghlaq Fault, Malta, which exhibits great exposures of deformation bands in carbonate grainstones (See section 1.4). The aims are achieved through following objectives:

- Document and describe the spatial distribution, structural characteristics and orientation of deformation bands in the field.
- Determine the petrophysical properties of deformation bands and host rock in the study area using a combination of image-based and laboratory techniques.
- Use collected outcrop and petrophysical data, supplemented by petrophysical data from the literature, to construct a deterministic reservoir model that includes the studied deformation bands.
- Test the effects of deformation bands dynamically by means of flow simulations of the outcrop model for a high-permeable host rock case and a low-permeable host rock case, where the deformation band permeability is the main variable tested.

1.4 Study area

The Maltese archipelago is situated in the Central Mediterranean, on the northern flank of the Late Miocene to Quaternary WNW-ESE trending Pantelleria Rift system. The islands are affected by two sets of normal faults, oriented ENE-WSW and WNW-ESE, where the majority of faults trend ENE-WSW. The Maghlaq Fault, located on the southwestern shore of

Malta is the only major fault onshore that has a similar trend as the offshore Pantelleria Rift (WNW-ESE; Fig. 1.1). There is an almost continuous exposure of the footwall of the Maghlaq Fault over a 4 kilometer long coastal outcrop, with the hangingwall preserved for 2.5 kilometers (Dart et al. 1993, Bonson et al. 2007). The fault offsets an Oligo-Miocene pre- to syn-rift carbonate succession by a minimum of 210 meters (Bonson et al. 2007). The study area of this master thesis is located in the eastern part of the Maghlaq Fault, where excellent exposure of the hangingwall allows for detailed studies of structural features, in particular deformation bands. The studied deformation bands are hosted in carbonate grainstones of the Aquitanian to Serravallian age, Globigerina Limestone Formation. Details about the geological setting of the Maltese islands and the study area will be presented in Chapter 3 and Chapter 4, respectively.
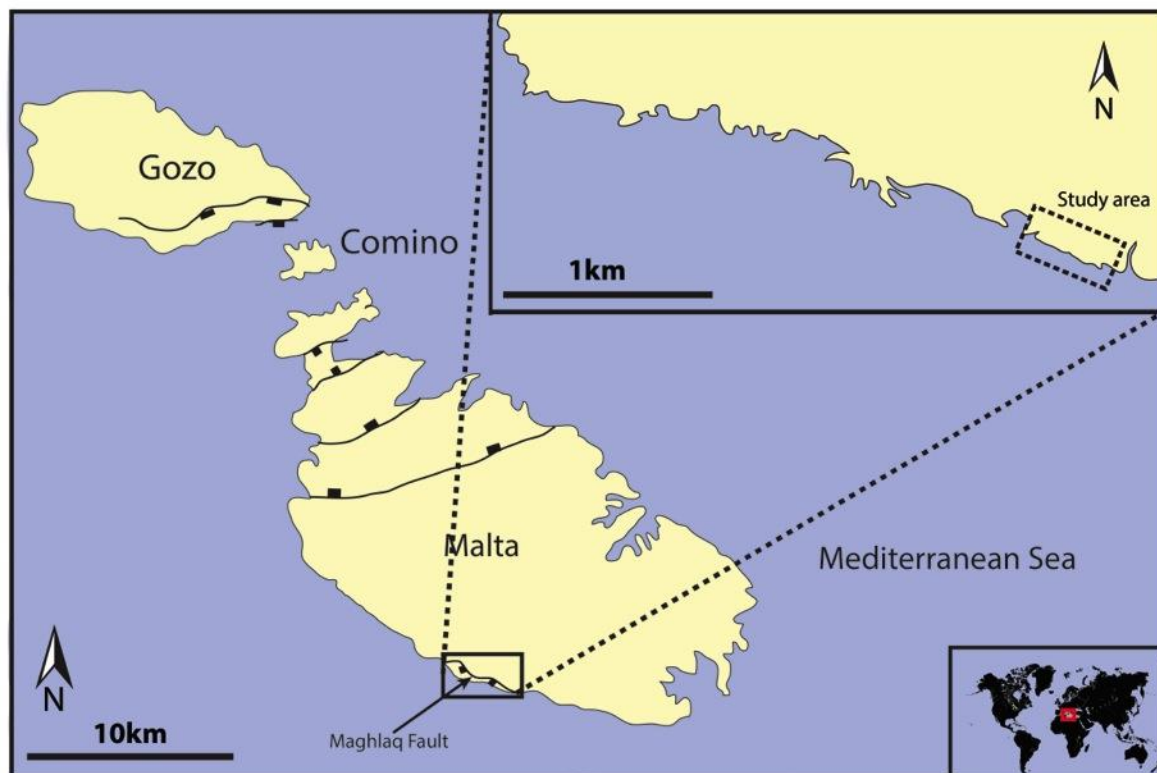
Figure 1.1: The Maltese archipelago is situated in the Central Mediterranean. The study area is located in the southwest Malta, in the eastern part of the WNW-ESE trending Maghlaq Fault. Here, the exposed hangingwall, composing the Miocene Globigerina Limestone Formation, allows for detailed studies of deformation bands. Note that the study area is outlined with a dashed box. Fault map modified from Dart et al. (1993).

1.5 Methodology

1.5.1   Field work
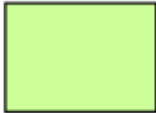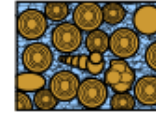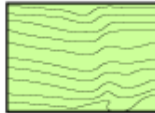
Fieldwork was conducted during two periods, 3 weeks in May and 3 weeks in October 2014. Data were collected by the use of traditional field methods including deformation band frequency scanlines along limestone beds within the wall of the Maghlaq Fault, where a total of 15 scanlines was recorded (see Chapter 4 and Appendix I). Data collected along the scanlines included lithofacies type as well as measurements of deformation bands frequency, - orientation and thickness. The collected data were analyzed and presented using programs such as Excel 2010, Adobe illustrator CS6, Stereonet 9.2 and Google Earth.

The localities for the scanlines were selected with the purpose to document spatial distribution and characteristics of the deformation bands within two limestone intervals (Lower and Middle Globigerina Limestone Members) with variable distances from the Maghlaq Fault.

To evaluate petrophysical properties of the deformation band as well as the undeformed host rock, a total of ten samples were obtained from the Middle Globigerina Limestone Member, of which five where used for core plug sampling. Methods used for permeability and porosity determinations are further explained in subsection 1.5.2.

Lithofacies classification

Lithofacies were classified using the Dunham (1962) and Embry and Klovan (1971) classification scheme based on depositional texture. This classification scheme is used to describe the composition of carbonate rocks in hand sample, defining carbonates depending on whether they are matrix-supported or grain-supported (Dunham 1962). A Lithostratigraphic column was made using this classification, in order to capture the variations in lithofacies for the examined units as well as the overlying and underlying beds. Note that this kind of classification does not differentiate between types of carbonate grains (Fig. 1.2).

Figure 1.2: Dunham classification of carbonate rocks, from SEPM (2013) modified after Dunham (1962).

Collection of deformation band frequency scanline data

Deformation band frequencies were mapped by counting the number of deformation band intersections per meter along fault perpendicular scanlines. Additionally, the orientation and thickness was recorded for the counted deformation bands. Uncertainties regarding the counting of deformation bands are related to the accuracy of the amount of deformation bands in clusters, as they are difficult to separate. Thus, in such cases, the deformation bands were registered as a cluster, rather than counting all the single deformation bands comprising the cluster.

Deformation band orientation measurements

Orientation data were measured by the use of a Silva Ranger compass with clinometer. In this study, Stereonet 9 version 9.2.0 was selected for the stereonet plots, where the data are plotted in the lower hemisphere in an equal-area projection. Limited exposures of deformation band planes made it problematic to measure the dip of the deformation bands, thus making it convenient to present the dataset in a Rose diagram. The Rose diagram illustrates the amount of deformation bands with a given orientation trend.

Deformation band thickness measurements

The deformation bands thickness was measured, both of individual deformation bands and clusters. Usually thickness variations occur along the bands, hence in cases with large variations, the estimated average thickness was considered.

1.5.2 Permeability and porosity measurements

Permeability and porosity measurements were conducted by the use of various laboratory and image analysis techniques, the specifics of which are outlined below.

A total of ten samples from Middle Globigerina Limestone Member were obtained in the field, of which five were used to drill inch-size core plugs for laboratory porosity and permeability measurements (see Appendix II for sample localities and plug details). Of these, three were host rock samples and two were samples with deformation bands. One of the plugs containing deformation bands was divided in two, resulting in a total of three core plugs with deformation bands. The core plugs are oriented bed-parallel, i.e. perpendicular to the deformation bands. Laboratory measurements of the core plugs were carried out at the School of Earth, Atmospheric and Environmental Science at the University of Manchester, determining both the porosity and permeability by gas-transfer techniques.

Gas permeability estimates were obtained by flowing gas through the core plug samples, determining the Klinkenberg-corrected gas permeability by the steady state technique (Klinkenberg 1941). This technique takes into account the discrepancies between permeabilities measured with gases and liquids as flowing fluids, i.e. deviations from Darcy's law (Rushing et al. 2004, Florence et al. 2007). For porosity estimates, a Helium porosimeter were used. This instrument works based on the principle of Boyle´s law (i.e. PV= constant, where V is the volume and P is the pressure). Note that the resolution of plug measurements is constrained by the plug length and diameter, whereas single deformation bands are only around 1 millimeter thick. Thus, laboratory plug measurements represent the effective permeability of the whole sample, which includes a deformation bands and its host rock.

In a parallel Msc-project at the Department of Earth Science in Bergen, polished thin sections of deformation bands and host rock from collected samples in the field (see Appendix II for sample localities) have been studied using optical and scanning electron microscopy (SEM). Here, backscattered electron (BSE) images of thin sections from SEM have been used for estimating the porosity of selected locations in the deformation bands and host rock within the thin sections. Porosity estimations (2D) were conducted by the use of the image analysis program ImageJ. See Grove and Jerram (2011) for details on this method.

Additionally, Anita Torabi (Uni CIPR in Bergen), provided porosity and permeability estimates using image-based processing of selected BSE-SEM images from thin sections (with 1000x magnification), developed in a function in MATLAB. Here, porosity and permeability is estimated using spatial correlation functions and a modified version of the Kozeny-Carman relation (i.e. relation between grain size and permeability; Torabi et al. 2008). The use of this image processing method provides an estimate of the porosity and permeability of deformation bands on the microscale in 2D, mapping out the variations in properties along and across deformation bands. Using such method eliminated the size limitations on the permeability and porosity estimations of deformation bands inflicted by traditional approaches (Torabi et al. 2008, Torabi & Fossen 2009).

1.5.3   3D Geocellular Reservoir Modeling

Reservoir models based on outcrop analogues (outcrop models) can contribute to better understanding of specific reservoir types, forming a base for generic models (e.g. Dreyer et al. 1993, Bryant et al. 2000, Pringle et al. 2006, Enge et al. 2007, Rotevatn et al. 2009a). The aim of this study is to build a deterministic model that represents carbonate reservoirs comprising deformation bands, based on the spatial structural data collected in the field, within the hangingwall of the Maghlaq Fault. For this purpose, the Reservoir Modeling System (RMS) 2013 was used. RMS is a commercial reservoir suite by Roxar Software Solutions, which allows a complete modeling workflow, from grid construction to flow simulation of property-filled grids (e.g. Rotevatn et al. 2009a). Concepts and background regarding 3D geocellular reservoir modeling is presented in Chapter 2, section 2.2.

The workflow of building the deterministic model will be described in more detail in Chapter 6. However, the main steps involved will be briefly described below:

1. The first stage of the RMS modeling workflow is to create surfaces. The surfaces form the framework and zone boundaries of the reservoir model, representing limits where changes in petrophysical properties and lithology occur.
2. When surfaces have been generated, they are used to create modeling zones. A 3D grid is created within each of the zones, representing the geocellular framework in which all of the property and facies modeling within RMS takes place.

3. The grid is further populated with properties, such as facies and petrophysical properties (i.e. porosity and permeability).

4. The final model can further be analyzed dynamically, involving simulating the flow through the model in order to understand how it would behave in a reservoir setting (Enge et al. 2007).

2. Theoretical background

In the following chapter terminology and theory related to deformation bands will be presented. Since most examples of deformation bands in the geological literature are reported from porous siliciclastic rocks, theory, classification schemes and formation conditions for deformation bands in sandstones will be presented first. Further, work done on deformation bands in carbonates will be presented, followed by petrophysical properties of deformation bands both in porous carbonate- and siliciclastic rocks. Lastly, a short introduction to 3D geocellular modeling will be given.

2.1 Deformation bands

2.1.1   Introduction

Extensional fractures and shear fractures (slip surfaces) generally form the principal deformation elements in low/non-porosity rocks. Such structures usually represent mechanically weak discontinuities that are prone to reactivation during subsequent stress build-up (Fossen et al. 2007). In porous granular rocks, the deformation processes are notably different from those of non- porous rocks. The existence of pore space allows grain reorganization, repacking, compaction, shear and/or dilation with subsequent changes in porosity. In addition to this, the grain contacts become stress focal points, which endorse grain fracturing and cataclasis when confining pressures are sufficiently high. The resulting strain is accommodated by formation of deformation structures known as deformation bands (Aydin 1978, Aydin & Johnson 1978).

Deformation bands are tabular zones, millimeter to centimeter- thick, which accommodates shear and/or volumetric deformation in porous rocks and sediments (Antonellini et al. 1994, Aydin et al. 2006, Fossen et al. 2007). They are confined to highly porous rocks, particularly sandstones with porosity in excess of *c*. 15% (Aydin & Johnson 1978, Fossen & Bale 2007). Further, in sandstones, deformation bands can occur as individual bands or as cluster zones of bands, generally characterized by enhanced cohesion, reduced permeability and limited amount of offset compared to ordinary fractures (Antonellini et al. 1994, Fossen et al. 2007). Their tendency to occur in zones and the accommodation of limited offset suggest that they

are associated with strain hardening (Aydin & Johnson 1983, Antonellini et al. 1994, Rotevatn & Fossen 2012).

In general, deformation bands in extensional settings are found in the damage zone of larger offset faults (Shipton & Cowie 2001), and are normally oriented parallel to sub-parallel to the main slip zone and reveal antithetic and synthetic orientations. However, oblique orientations can occur locally (Shipton & Cowie 2001, 2003, Berg & Skar 2005), e.g. in zones of fault overlap and linkage (Antonellini et al. 1994, Rotevatn et al. 2007).

2.1.2   Classification

Deformation bands can be classified in terms of either kinematic framework or dominating deformation mechanism.

Based on the kinematic framework, the deformation bands can be classified as compaction bands, (simple) shear bands, dilation bands or hybrids of these types (Fig. 2.1). Shear bands have displacement parallel to the band, while compaction/dilation bands are characterized by displacement perpendicular to the bands, resulting in subsequent volume decrease in compaction bands and volume increase in dilation bands (Aydin et al. 2006, Fossen et al. 2007). In terms of orientation of the deformation bands relative to the maximum principal stress (σ_1), compaction band form perpendicular to σ_1 and dilation band form parallel to σ_1. Shear bands on the other hand, may develop at angles ranging between that of compaction bands and dilation bands (Bésuelle 2001, Eichhubl et al. 2010).

The majority of the deformation bands show a prevailing component of shear displacement, typically a few millimeters or centimeters across single deformation bands. However, some attendant compaction caused by grain reorganization with or without cataclasis across the band is common (Fossen & Bale 2007, Fossen et al. 2007). Pure compaction bands are less common (Mollema & Antonellini 1996) and examples of dilations bands are rare (Du Bernard et al. 2002).
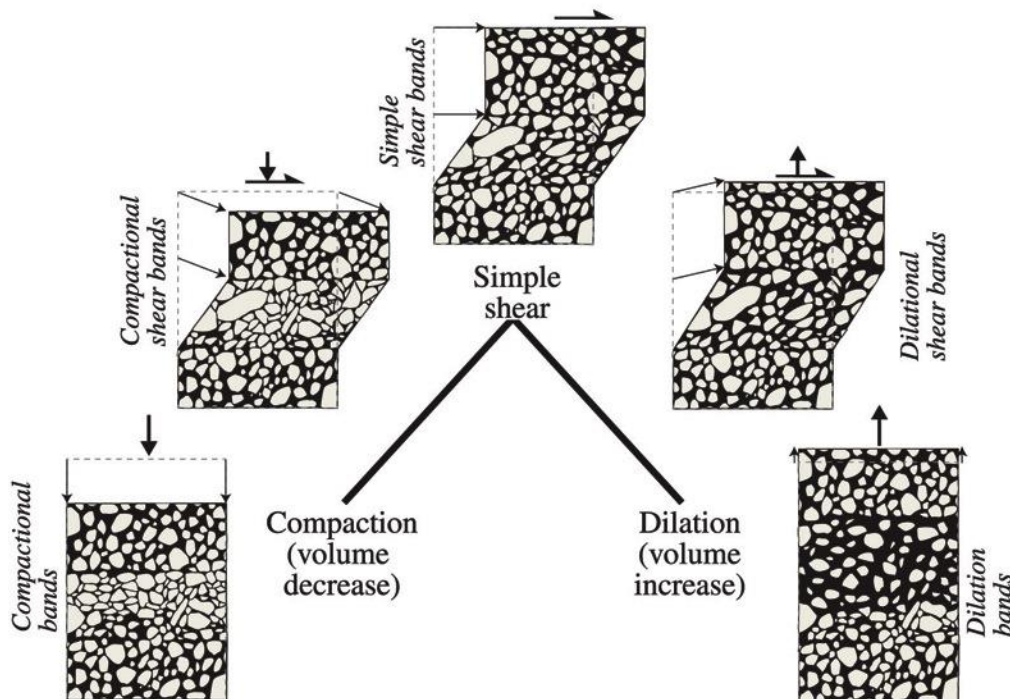
Figure 2.1: Kinematic classification of deformation bands. Shear bands have displacement parallel to the band, whereas compaction/dilation bands are characterized by displacement perpendicular to the bands, resulting in subsequent volume decrease in compaction bands and volume increase in dilation bands. From Fossen et al. (2007).

In terms of dominating deformation mechanism, the deformation bands can be classified into disaggregation bands, phyllosillicate bands, cataclastic bands or solution and cementation bands (Fig. 2.2). The dominant mechanisms are: 1.Granular flow (grain rotation and grain boundary sliding), 2.Phyllosilicate smearing, 3.Cataclasis (grain fracturing and abrasion or grinding), and 4. Dissolution and cementation, respectively (Fossen et al. 2007). For the purpose of this study, only the disaggregation- and cataclastic deformation bands will be further emphasized.

Disaggregation bands

Disaggregation bands forms as a result of granular flow, by means of grain boundary sliding, grain rolling and breaking of grain bonding cements. The grain reorganization may lead to dilation, or more frequently, compaction. Disaggregation bands are usually found at shallow burial depths (< 1 kilometer) in poorly consolidated sandstones (Mandl et al. 1977, Du Bernard et al. 2002). In general, the disaggregation bands have true offset up to some centimeters, length less than a few tens of meters and varying thickness depending on the grain size of the rock (Exner & Grasemann 2010). Fine-grained rocks typically develop 1-

millimeter thick bands, while coarse- grained rocks may reach thicknesses of at least 5 millimeters (Fossen et al. 2007).

Cataclastic bands

The cataclastic deformation bands are associated with mechanical grain fracturing and grain crushing, and are typically observed in rocks that have been buried to depths greater than *c.* 1,5 kilometers (Aydin 1978, Aydin & Johnson 1983, Fossen et al. 2007). Characteristic of this type of deformation band is the central cataclastic core, commonly with a wide grain-size distribution, angular grains, absence of pore space and high content of matrix due to grain-size reduction (e.g. Antonellini et al. 1994, Fossen et al. 2007). The grain crushing during cataslasis results in grain interlocking and reduced porosity, which in turn endorse strain hardening (Aydin 1978). Strain hardening might explain the smaller displacement observed on cataclastic deformation bands (<4 centimeters), compared with disaggregation bands with similar lengths (Fossen et al. 2007).
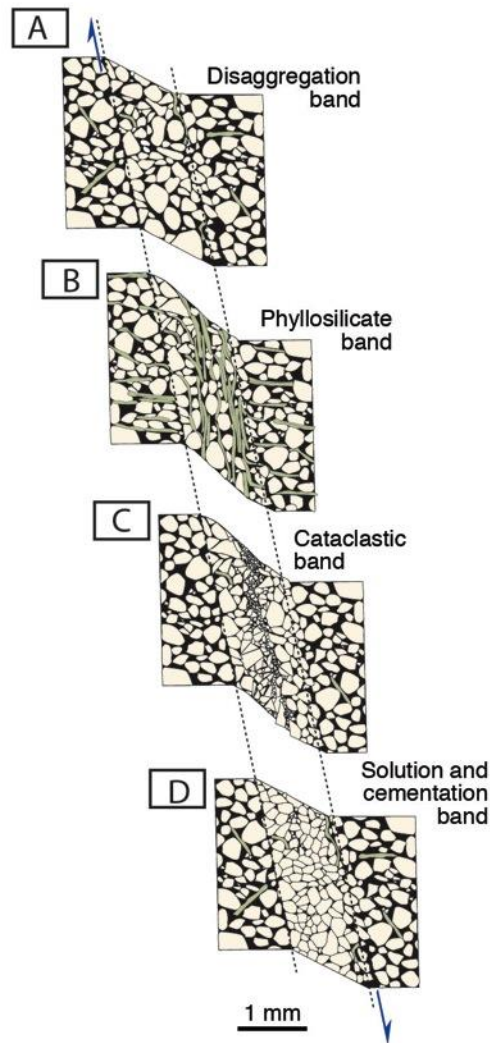
Figure 2.2: In terms of dominating deformation mechanism, deformation bands can be classified into: A) disaggregation bands, where the dominant mechanism is granular flow (grain rotation and grain boundary sliding), B) Phyllosillicate bands dominated by phyllosillicate smearing, C) Cataclastic bands where cataclasis dominate (i.e. grain fracturing) and D) Dissolution and cementation bands, dominated by dissolution and cementation. From Fossen (2010), modified after Fossen et al. (2007).

2.1.3   Formation conditions

Factors such as burial depth (confining pressure), tectonic environment (stress state) and host rock properties (i.e. degree of lithification, grain size, grain shape, sorting, mineralogy and porosity) control the deformation mechanism of the bands (Fossen & Bale 2007, Fossen et al. 2007). For a given sedimentary rock layer, some of these factors may be more or less constant. However, variations might occur, causing prompt changes in deformation bands style. Other factors, such as confining pressure, stress state, permeability, porosity and cementation are likely to change with time. As a result, deformation band style may change with for example increased burial depth (Fig 2.3) (Fossen et al. 2007).

In sandstones, the initial forming deformation bands are typically disaggregation bands or phyllosilicate bands. These structures form at shallow burial depths with low confining pressures (>1 kilometer), when grain bindings are weak and grain contact surfaces are low (Fossen et al. 2007). Cataclastic deformation bands can also form at low confining pressure, preferentially in poorly consolidated sands where well-sorted and well-rounded grains lead to high stresses being focused at grain contact points (Cashman & Cashman 2000, Rawling & Goodwin 2003, Fossen et al. 2007). However, high confining pressure is favorable for the formation of cataclastic bands (> 1,5 kilometers), resulting in more intense cataclasis compared to those formed at shallower depths (Fossen et al. 2007, Rotevatn et al. 2008). Further, when a rock becomes a cohesive lithology with lower porosity, deformation tends to occur in terms of crack propagation instead of pore space collapse. Thus, subsequent slip surfaces, joints and mineral-filled factures can form (Fossen et al. 2007).
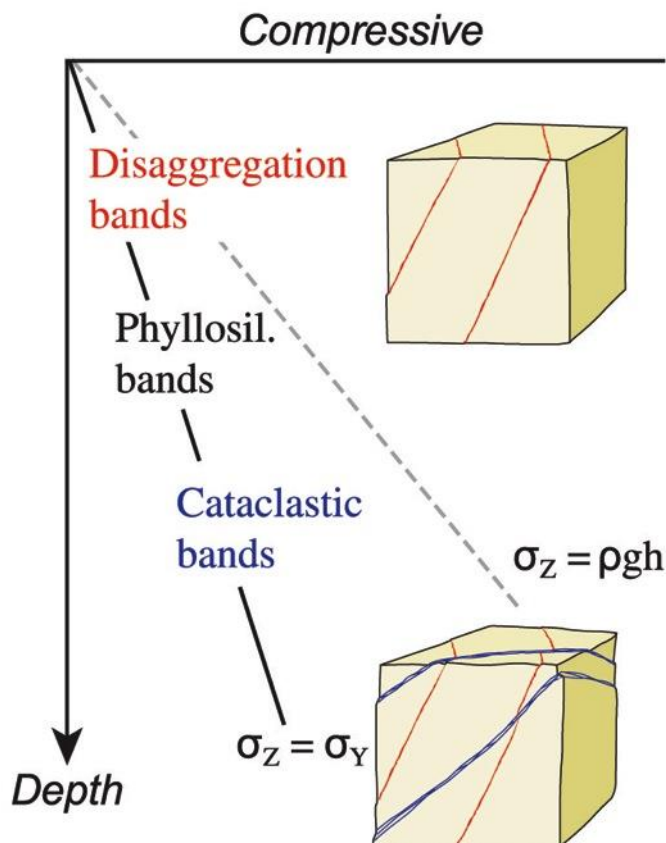
Figure 2.3: Different types of deformation bands form at different stages during burial. At shallow burial depths (low confining pressures) the earliest forming deformation bands in sandstones are typically disaggregation bands or phyllosilicate bands. Further, at greater burial depths (higher confining pressures) cataclastic bands usually forms. Modified from (Fossen 2010).

2.1.4   Deformation bands in porous carbonate rocks

In the geological literature the majority of the deformation bands are reported from porous siliciclastic rocks, and only a few examples have been documented in porous carbonate rocks. The knowledge about the deformation mechanisms and petrophysical properties of deformation bands in porous carbonates is thus limited (e.g. Tondi et al. 2006, Tondi 2007, Rath et al. 2011, Rustichelli et al. 2012, Antonellini et al. 2014).

The majority of reported field examples of deformation bands in carbonates rocks are from grainstones, where bioclastic fragments and sparite ooids usually form the framework of the rock (Antonellini et al. 2014, and references therein). In terms of dominating micro-mechanism, development of deformation bands in carbonates includes pore collapse, grain sliding with rotation and pressure solution (Tondi et al. 2006, Tondi 2007, Rath et al. 2011). Cataclasis and grain crushing is generally mediated by pressure solution in natural deformation bands (Micarelli et al. 2006, Tondi et al. 2006). Alternatively, laboratory experiments document grain crushing with no pressure solution as the dominant deformation micro-process (Cilona et al. 2012).

The mechanical responses of carbonates with changing stress conditions and various level of plastic strain have been investigated in laboratory experiments (Cilona et al. 2012, and references therein). For carbonates with a wide range of porosity (3-45%) granular flow involving grain translation and rotation with pore collapse is the prevailing mechanism under low-to-high confining pressures. At the higher end of the porosities, lower confining pressures are required for the compactive process to occur by means of pore collapse (Baud et al. 2000, Vajdova et al. 2004, Tondi et al. 2006). Nevertheless, Baud et al. (2009) showed that at high confining pressures, compaction localization is inhibited, and homogeneous cataclastic flow with grain cracking and crushing becomes dominant mechanism. In some cases, increasing pressure also endorse calcite mechanical twinning (Cilona et al. 2012). Furthermore, in natural examples of deformation bands, with the presence of fluids, dissolution and cementation processes are associated with the development of deformation bands. Further, increasing degree of cementation might results in a change of deformation mechanism from grain rotation and compaction to cataclastic deformation (Rath et al. 2011).

2.1.5   Petrophysical properties

The development of deformation bands is associated with a reduction in permeability and porosity with respect to the host rock that they occur in (Antonellini & Aydin 1994, 1995). Therefore, deformation bands have been a subject of interest for their possible effect on fluid flow in reservoir rocks (e.g. Matthäi et al. 1998, Sternlof et al. 2004, Sternlof et al. 2006, Kolyukhin et al. 2010, Ballas et al. 2012, Ballas et al. 2013). In sandstone reservoirs, studies have shown that the porosity and permeability contrasts in disaggregation bands relative to host rock are relatively low (e.g. Fisher & Knipe 2001, Fossen et al. 2007). Cataclastic bands, on the other hand, reveal a porosity reduction by up to an order of magnitude by grain crushing and associated change in grain-size distribution. The porosity reduction produces a corresponding decrease in permeability of two to three, and occasionally as much as six, orders of magnitude relative to the host rock (e.g. Antonellini & Aydin 1994, Antonellini et al. 1999, Fisher & Knipe 2001, Jourde et al. 2002).

In carbonate rocks, porosity reductions of one order of magnitude is reported from the host rock to the deformation band, while the permeability decrease varies from as much as three orders of magnitude (Rath et al. 2011) to one order of magnitude (Antonellini et al. 2014) in compaction bands. The very low (*c*.1%) porosity core of some well-developed deformation bands with large shear displacement results in permeabilities as low as 0.2 mD (Rath et al. 2011). Nevertheless, concerning sandstones and limestones, cementation and dissolution processes in deformation bands may significantly increase the reduction of porosity and permeability caused by reorganization of grains and mechanical crushing (e.g. Ogilvie & Glover 2001, Rath et al. 2011). Given the highly reactive nature of carbonate minerals, carbonates are less resistant to chemical compaction and associated cementation (Ehrenberg & Nadeau 2005). Thus, development of deformation bands in carbonate rocks are typically associated with dissolution and cementation processes (Cilona et al. 2012).

The influence of deformation bands on fluid flow depends not only on the permeability contrast, but other factors such as number of bands (collective thickness), orientation and continuity, and the variation in porosity and permeability in three dimensions (Fossen et al. 2007). Commonly, deformation bands show variations in thickness, internal microstructure, porosity and permeability along the bands at millimeter-centimeter scale. Estimated permeability variations can thus change from zero to two or three orders of magnitude over a

short distance within a single band. The rapid variations in properties along bands can make the deformation bands leaky, and thus reduce their ability to act as barriers to fluid flow (Torabi & Fossen 2009). Based on mathematical considerations in sandstone reservoirs, Fossen and Bale (2007) concluded that permeability reduction must be very high (more than three orders of magnitude) and/or the band concentration must be exceptionally high before representing a substantial barrier to fluid flow.

2.2 3D Geocellular Reservoir Modeling

2.2.1   Background and concepts

A reservoir model is a computer based, three-dimensional quantitative model and a mathematical representation of a volume of rock. In the geocellular model, the volume is divided into cells with assigned properties, such as facies, porosity, permeability, etc. (Enge & Howell 2010). Three-dimensional geocellular modeling is a widely used method for representing and investigating the subsurface environment, both statically (volume, geometry etc.) and dynamically (simulating fluid flow; Rotevatn et al. 2009a). Subsurface reservoir models are based on horizon and fault interpretation of seismic data, supplemented with geological and petrophysical properties sampled from wells. Since wells are commonly widely spaced (> kilometer offshore), interpolation between the wells is subject to a high degree of uncertainty (Rotevatn et al. 2009a, Enge & Howell 2010). Uncertainty is a key factor occurring at all stages of the modeling, and is commonly handled by using stochastic methods (statistic), including multiple plausible realizations to produce a suite of possible outcomes (Haldorsen & Damsleth 1990, Durlofsky 2003).

The use of analogues is essential in geology, especially when working with spatially limited or low-resolution data (Rotevatn et al. 2009a). Porous clastic reservoirs are known to encompass small- scale heterogeneities, such as deformation bands. Given their small-scale nature, far below current seismic resolution, they are largely underrepresented in reservoir models (Zuluaga et al., *in review*). Thus, outcrop data provide significantly better vertical resolution compared to seismic data, and better lateral information than spatially constrained cores and borehole-derived logs as illustrated in Figure 2.4 (Rotevatn et al. 2009a). Nonetheless, the number of grid cells that can be handled by the computer limits the

resolution of the rock heterogeneities. A typical North Sea geocellular model grid resolution is 50 m x 50 m x 1 m (e.g. Fredman et al. 2008), and if such geological details (e.g. deformation bands) were to be included explicitly in conventional field-scale reservoir models, it would require a finer grid, resulting in substantial number of cells in the model. In turn, this is computationally expensive in terms of central processing unit time. Additionally, a large number of cells can in extreme cases render models unmanageable (e.g. Fachri et al. 2011). In general, some type of averaging or upscaling procedures is necessary from the geological model to the simulation grid, in order to reduce the number of cells (Jourde et al. 2002, Pickup & Hern 2002). By upscaling high-resolution models into coarser grids, the detailed heterogeneities distributed over several cells in the original models, is replaced with averaged values in larger cells occupying the same volume. Such implicit representation of small-scale heterogeneities leads to larger uncertainties in the result (e.g. Rotevatn et al. 2009a, Fachri et al. 2011).
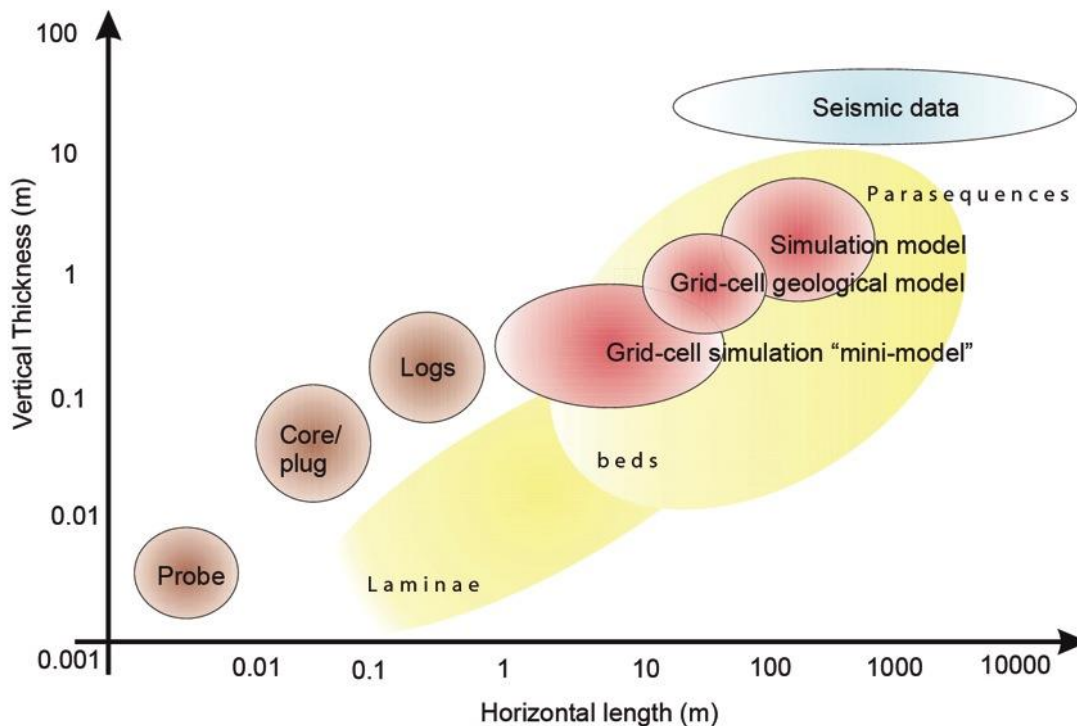
Figure 2.4: Illustration of typical length scales of sedimentary structures in the vertical and horizontal directions, along with scales of commonly used measurements and reservoir model sizes. Modified from Enge et al. (2007), after Pickup and Hern (2002).

3. Geological setting

The following chapter provides an overview of the tectonic evolution of the Central Mediterranean, with main focus on the Pelagian block. Further, the tectonic and stratigraphical setting of the Maltese archipelago will be presented.

3.1 Regional tectonic framework

3.1.1   Tectonic evolution of the Central Mediterranean

Complex interactions between orogenic processes and extensional tectonics characterize the geological evolution of the Mediterranean (Rosenbaum et al. 2002). The Mediterranean is comprised of several basins, and a system of connected fold and thrust belts that developed in a framework of relative movement between the African and European plates, in addition to the smaller Adriatic and Iberian plates (Casero & Roure 1994, Cavazza & Wezel 2003, Carminati et al. 2012). The formation of the fold and thrust belts vary in terms of both timing and tectonic setting, and are considered to be a result of the closure of different oceanic basins of variable age and size (Cavazza & Wezel 2003).

Based on geomorphology, significant differences can be recognized between the western and eastern part of the Mediterranean basin (Morelli 1985, Vanney & Gennesseaux 1985). In the western part of the Mediterranean, several sub-basins can be recognized including the Alboran, Valencia, Provençal, Algerian and Tyrrhenian basins (Gueguen et al. 1998, Carminati et al. 2012).These basins are related to back- arc extension due to roll-back of the hangingwall in the Apennine- Maghrebian subduction zone. From east to west, the basins have a progressively younger age; with the oldest Alboran, Valencia, Provençal and Algerian basins of Oligo- Miocene age in the west, and Tyrrhenian basin of late Mioce to Plio-Pleistoncene age in the east (Kastens et al. 1988, Gueguen et al. 1998). The eastern Mediterranean comprises the relatively stable region of the basin (e.g Pelagian block), and results principally from deformation of the northern perimeter of the African plate (Vanney & Gennesseaux 1985). It is geologically older than the western part, and the basin is probably underlain by remnants of Mesozoic oceanic crust (Neotethys) below the sediments (Rosenbaum et al. 2002).

3.1.2   The Pelagian block

The Pelagian block composes the northern part of the African continental plate, and consists of a Mesozoic- Cenozoic carbonate succession overlying continental basement of unknown age (Reuther & Eisbacher 1985, Civile et al. 2010). Four structural domains can be recognized in the block (Fig. 3.1): 1. The Malta Escarpment to the east, 2. Apennine-Maghrebian fold- and thrust belt along the northern and western margin, 3. Shallow shelves (e.g. Hyblean- Malta Plateau) and 4. The Pantelleria Rift system (Micallef et al. 2013).

The Malta Escarpment in the east separates the Pelagian block from the Ionian abyssal plain, in an ocean-continent transition (Granath & Casero 2004). The escarpment is a NNW-SSE trending extensional fault system that probably follows an older crustal fracture zone (Reuther & Eisbacher 1985, Micallef et al. 2013). Argnani and Bonazzi (2005) interpreted the escarpment to be a feature inherited from Mesozoic or possibly earlier (Permo-Triassic) times, and later reactivated during the convergent movement between the African and European plates from the latest Cretaceous.

From late Cretaceous to Early Pleistocene, the European and the westward- subducting Ionian and Adria plates collided, resulting in the formation of the Apennine- Maghebian fold-thrust belt that runs along North Africa and Sicily, forming the northern and western margin of the Pelagian platform (Elter et al. 2003). Caught in the middle of the collision front is the more buoyant continental crust of the Hyblean- Malta Plateau, which cannot be subducted that easily. As a result the crust of the plateau is thicker and structurally elevated relative to its surroundings (Gardiner et al. 1995).

A period of extension initiated in the Oligocene, simultaneously with the mountain belt formation, and several basins evolved adjacent to the convergent margin (Elter et al. 2003). In the central part of the Pelagian block, between Tunisia and Sicily is the ENE-WNW striking Pantelleria Rift (or Sicily Channel Rift Zone) (Cello et al. 1985). The rift system comprises a complex horst and graben structure about 100 km wide and 600km long (Grasso et al. 1986). Three elongate troughs make up the rift system: Malta, Linosa and Pantelleria grabens (Dart et al. 1993), in which the maximum water depth ranges between 1300 and 1700 meters (Reuther & Eisbacher 1985). Beneath the rift, the crust is less than 20 km thick, with relatively high heatflow values (100 mw/m-2) and gravimetric data showing Bouguer

anomalies varying between +40 and +80 mGal (Cello et al. 1985). The rift axis comprise two volcanic islands (Linosa and Pantelleria), where the volcanic rocks reveal ages of 10 Ma to the present (Dart et al. 1993).

Based on the above data, Illies (1981) interpreted the rift as being a result of intra- continental rifting associated with NE oriented displacement of Sicily away from the African continent. Jongsma et al. (1987) on the other hand stated that the formation of the Pantelleria rift involved a large scale E-W or NW-SE trending dextral wrench system with the troughs initiating as pull-apart (transtensional) basins. This model is largely based on recognition of a strike-slip zone in seismic data from the Medina Channel Wrench, in addition to interpretation of E-W strike-slip fault movement from the southeastern part of Gozo. Argnani (1990) suggested an alternative model, with an N-S oriented extensional regime associated with the back-arc extension in the Tyrrhenian Sea and compression in the Apennine- Maghrebian fold-thrust belt. In this model, an N-S trending transfer fault separates the Pantelleria trough from the Malta and Linosa troughs, characterized by a line of volcanic centers and localized basins and highs.
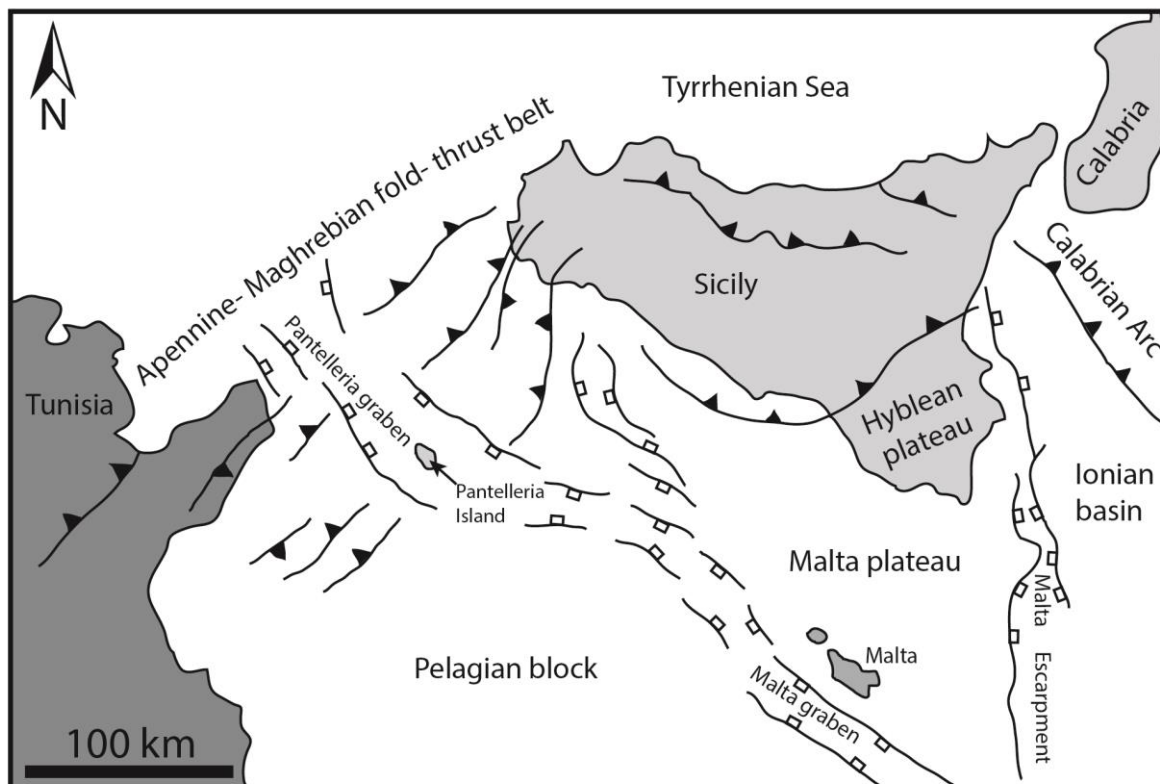
Figure 3.1: Four structural domains can be recognized in the Pelagian block: 1. Malta escarpment to the east, 2. Apennine-Maghrebian fold-thrust belt along the northern and western margin, 3. Shallow shelves (Hyblean and Malta plateau), and 4. The Pantelleria Rift system. Modified from Granath and Casero (2004).

3.1.3   The Maltese islands

The Maltese archipelago (Malta, Gozo, Comino and some smaller uninhabited isles) is located on the northern shoulder of the Pantelleria rift system, forming one on the few emergent areas of the Pelagian block (Fig. 3.2A). The islands and its surrounding area are dominated by the Maltese graben system, a series of Miocene to Pliocene rifts (Dart et al. 1993). The graben architectures feature graben and half-graben geometries, generally with planar faults systems with average dips of 64° to 73°. Five tectonic units construct the Maltese graben system: The Pantelleria Rift, North Malta Graben, Malta Horst, North Gozo Graben and Gozo Horst. The ENE- WSW trending North Malta Graben and Nort Gozo graben (and the intervening Malta and Gozo Horsts) dissect the ESE-WNW trending Pantelleria rift at acute angles of 32° and 66° respectively (Dart et al. 1993). Both fault trends were active in Miocene to Recent time (Illies 1981), with the most active period during Plio-Quaternary times (Dart et al. 1993). Uplift of the northern rift flank of the Pantelleria rift, combined with a falling sea- level, caused the emergence of the archipelago during early Messinian times (Bonson et al. 2007).

Onshore exposures of the Malta Graben reveal mainly two extensional fault trends: ENE-WSW and WNW-ESE, where the majority trends ENE-WSW (Fig. 3.2B). In addition to the North Malta Graben exposed on the northern part of the Maltese island, there are several minor ENE- WSW trending faults (Dart et al. 1993). The WNW-ESE striking Maghlaq Fault located on the coast of southwest Malta is the only major fault onshore with a Pantelleria Rift trend (Dart et al. 1993, Bonson et al. 2007).

Illies (1980, 1981) suggested that rifting in two stages controlled the tectonic evolution of the island. The oldest rift generation, composing the ENE-WSW trending faults of the North Malta Graben was active during the Early Miocene. This interpretation is based on observed syn-kinematic strata in addition to the presence of sedimentary dikes parallel to the future rift. Further, the older rift generation trending ENE-WSW was cut by younger WNW-ESE trending faults related to the Pantelleria rift during the second phase from Miocene/Early Pliocene to present. This superimposition of two different fault trends was interpreted to be a result of a rotation of the controlling stress regime approximately 10 m.y. ago.

Based on analysis of fault related changes in sediment thickness from offshore 2D seismic data, Dart et al. (1993) on the other hand stated that both fault trends were coeval, although the two fault sets are almost orthogonal. By the use of fault slip data from stratigraphic offset and fault planes, both fault trends were interpreted to form in response to N-S directed extension, with the fault kinematics remaining homogenous throughout the deformation. This interpretation in consistent with Argnani's (1990) characterization of a major N-S oriented transfer fault between the Pantelleria trough and the Malta and Linosa troughs.
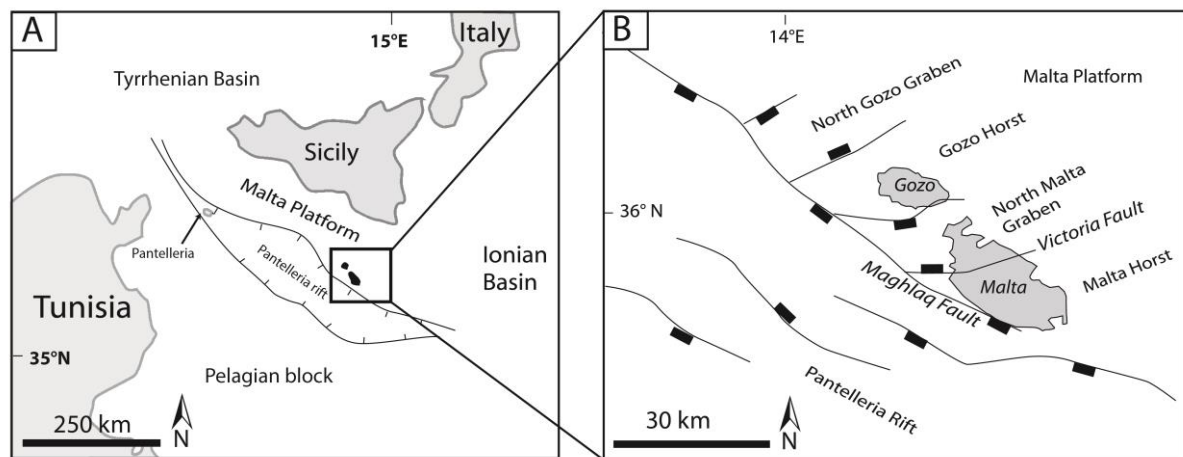
Figure 3.2: Illustration of the location of the Maltese Archipelago. A) The Maltese island is located in the Central Mediterranean, on the northern shoulder of the Pantelleria Rift system, south of Sicily. B) Main structures of the Maltese island, oriented ENE-WSW and WNW-ESE, where the majority trends ENE-WNW. The Maghlaq Fault is the only major fault onshore with Pantelleria Rift trend. Modified from Missenard et al. (2014).

3.2 Regional stratigraphic framework

The stratigraphy on the Maltese island is presented in Figure 3.3, and is subdivided into four Oligo-Miocene lithostratigraphic units; pre-rift, early syn-rift, late syn-rift and post-rift (Dart et al. 1993). The pre-rift formations overlie continental crust of African origin of unknown age (Jongsma et al. 1985, Civile et al. 2010). Nevertheless, basement rocks are not observed in the study area and will not be further discussed here.
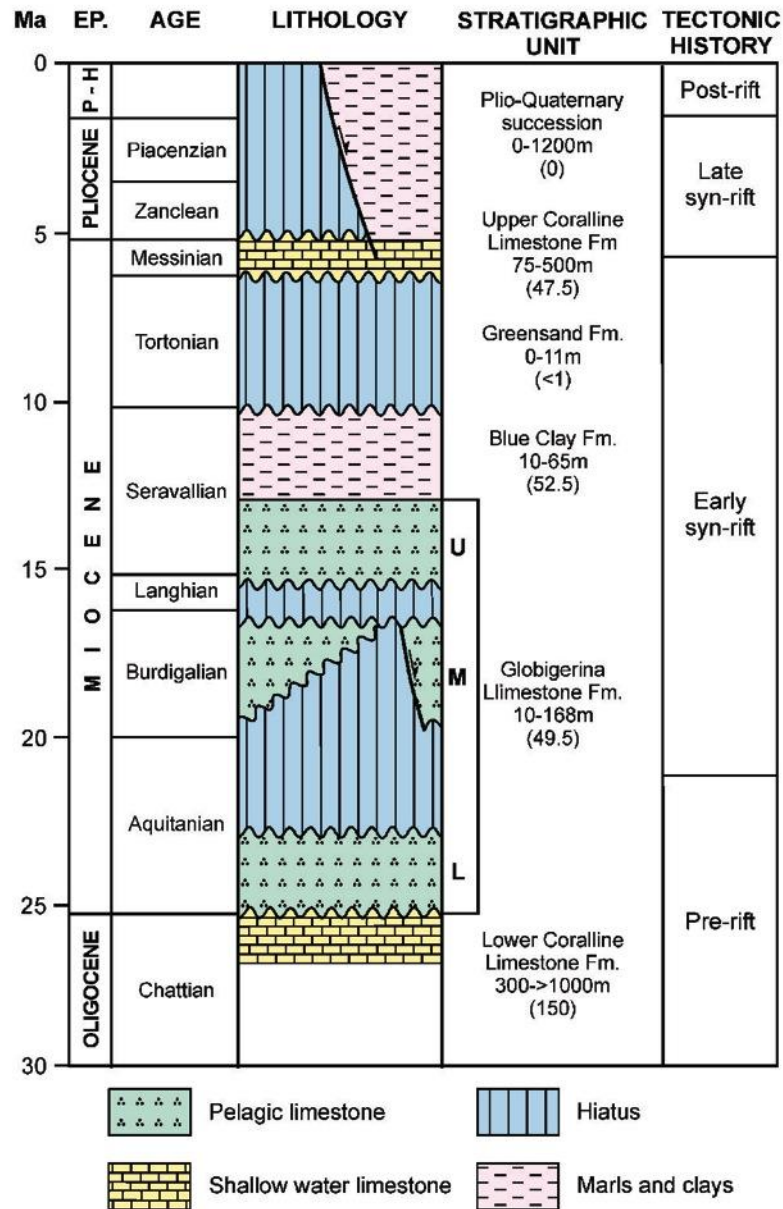
Figure 3.3: The stratigraphy of the Maltese island can be divided into four Oligo-Miocene lithostratigraphic units: pre-rift, early syn-rift, late syn-rift and post-rift. Note that EP. denotes "Epoch", where P-H represents Pleistocene to Holocene, which is otherwise referred to as Quaternary in the text. Modified from Bonson et al. (2007).

3.2.1   Pre- rift

Lower Coralline Limestone Formation platform carbonates and Lower Globigerina Limestone Member pelagic carbonates compose the pre- rift stratigraphy onshore Malta. The pre-rift strata are defined by parallel stratal geometries, which have been tilted by later tectonic motions. There is no sign of fault related thickness changes, and the lateral facies margins display no relationship to fault traces (Dart et al. 1993).

The Oligocene (Chattian) Lower Coralline Limestone Formation can be up to 1000 meters thick, although less than 140 m are exposed on the Maltese mainland (Pedley et al. 1976, Bonson et al. 2007). The outcropping sedimentary successions predominantly comprise shallow water algal limestones overlaid by a hardground surface (Dart et al. 1993).

On the basis of the variety of sedimentary facies, Pedley (1978) subdivided the Lower Coralline Limestone Formations into four members (older to younger): 1) The Maghlaq Member, comprising inner ramp wackestones and mudstones; 2) The Attard Member, characterized by rhodolitic algal packstones; 3) The Xlendi Member, represented by an upward shallowing succession of bioclastic units, together with *Scutella* beds and cross-bedded biosparites; and 5) The Il Mara Member, composed of outer ramp wackestones, including bryozoan and Lepidocyclina beds.

The depositional environment envisaged for the Lower Coralline Limestone bed is initially in a shallow gulf, changing progressively to open marine conditions, and finally a shallow marine shoal situation comprising at least one area of protected deeper water (Alexander 1988).

The subsequent Aquitanian Lower Globigerina Limestone Member can attain thicknesses up to 100 meters, and is mainly composed of outer shelf pelagic foraminiferal wackestones, recording an upward increase in water depth. The pelagic wackestones are capped by a second hardground surface that formed in a period of shallowing. Further, this hardground is cut by Neptunian dykes, marking the onset of the early syn-rift phase (Dart et al. 1993). The Neptunian dykes, i.e. sedimentary dykes formed by sediment infilling of submarine cavities/fissures (e.g. Lehner 1991), descend approximately 3 meters into the Lower Globigerina Limestone Member from its terminal hardground (Dart et al. 1993). The dykes can be up to 50 centimeters wide, and encompass infill of hardground blocks and phosphatic conglomerate material corresponding to the basal unit of the Middle Globigerina Limestone Formation (Dart et al. 1993).

3.2.2   Syn- Rift

The early syn-rift strata of the Maltese mainland consist of Middle and Upper Globigerina Limestone Members, Blue Clay Formation, Greensand Formation and the lower sequences of

the Upper Coralline Limestone Formation. Strata of the early syn-rift phase are characterized by minor fault related thickness changes, Neptunian dykes and some evidence for minimal fault related bathymetric relief (Dart et al. 1993). The late syn-rift phase commenced with the uppermost sequence of the Upper Coralline Limestone Formation, and ceased within the Plio-Quaternary succession. Fault controlled facies distribution; areas of non- deposition and major fault growth causing divergent fanning strata define the late syn-rift phase. Severe fault activity resulted in seabed surface breaks of several tens to several hundred meters (Dart et al. 1993).

The early syn-rift succession

The Burdigalian to Serravallian Middle and Lower Globigerina Limestone Members comprises a rather uniform succession of pelagic wackestones and marls and have thicknesses of up to 100 meters and 14-18 meters respectively (Dart et al. 1993, Bonson et al. 2007). Phosphoritic conglomeratic layers that averages less than 1 meter in thickness form marker beds, overlying well-developed hardgrounds (Bonson et al. 2007). Phosphorites in marine carbonate shelf environments are associated with depositional hiatus and subsequent submarine lithification, often resulting in hardground development (Pedley & Bennett 1985). Two principal phosporite levels divide the Globigerina Limestone Formation; The C1 bed separates the Lower Globigerina Limestone from the overlying Middle Globigerina Limestone, and the C2 bed separates the Middle Globigerina Limestone from the Upper Globigerina Limestone (Pedley & Bennett 1985). Regionally, based on field and exploration well-data, the Globigerina Limestone Formation, as a whole, gradually thickens to the south: from 10 meters to 168 meters (Dart et al. 1993).

Pteropods and massive units of moderately consolidated plaktonic foraminifera (*Globigerina*) compose the Globigerina Limestone Formation. The deposits represent a deepening to outer shelf conditions (Bonson et al. 2007), in water depth ranging from 40-150 meters (Pedley et al. 1978). According to Pedley et al. (1978), accumulation of sediments with high planktonic foraminiferal content on a shallow shelf area is probably related to the location of Malta during Miocene, on a submarine rise (i.e. Hyblean Plateau).

The deepening upward trend in the Globigerina Limestone Formation reaches its maximum during the deposition of the Blue Clay Formation (Jacobs et al. 1996) that may have been

deposited in water depths up to 150 meters within an open muddy marine environment (Pedley et al. 1976).

A rapid transitional change from globigerinid biomicrites to globigerinid marls characterizes the conformable boundary between the Globigerina Limestone Formation, and the overlying Blue Clay Formation (Pedley et al. 1976). The maximum- recorded thickness of the formation is 65 meters, and corresponds to the Serravallian stage (Pedley et al. 1976, Föllmi et al. 2008). Across Gozo, the formation thin southwards (60-10 meters), and in rift margin areas of eastern Malta, the formation is absent (Dart et al. 1993). Alternating pale-grey and dark-grey banding characterize the Blue Clay formation, predominantly composed of kaolinite and glauconite (Bonson et al. 2007). According to Murray (1890) the formation contains less than 30 per cent carbonate material. Jacobs et al. (1996) suggested that the deepening of the shelf resulted in a change in the carbonate content of the deposits, with the low carbonate content of the Blue Clay Formation reflecting a combination of increased dilution by detrital clay, decreased carbonate production and increased dissolution of carbonate.

A distinct boundary marks is recognized between the Blue Clay Formation and the overlying Greensand Formation, or directly with the Upper Coralline Limestone Formation (Föllmi et al. 2008). The boundary is characterized by a modest angular unconformity, and a substantial hiatus (Dart et al. 1993). In Late Miocene, the deepening upward trend of the Malta shelf reversed, and the Greensand Formation and the Upper Coralline Formation represents a shallowing upward of the Maltese shelf and the re-establishment of carbonate platform conditions (Jacobs et al. 1996). The Tortonian Greensand formation consists of poorly-cemented bioclastic, glauconitic limestones (Alexander 1988), which is rarely greater than 1 meter thick throughout Malta (Pedley et al. 1976, Dart et al. 1993). Intense bioturbation, abundance of *Heterostegina*, and the presence of large echinoids indicate a shallow marine environment of water depths less than 70 meters (Pedley et al. 1976, Jacobs et al. 1996).

The Late Tortonian to Messinian Upper Coralline Limestone Formation represents a carbonate platform growing in water depths of less than 50 meters with epibenthic foraminifera and calcareous algae (Jacobs et al. 1996) that may reach thicknesses of more than 100 meters (e.g. Micallef et al. 2013). Three depositional sequences can be recognized within the formation, exhibiting a transition from coralline algal biostrome facies at the basal unit, to coral and algal patch reefs, and lastly to platform and slope facies at the top of the

formation (Bonson et al. 2007). The three depositional sequences represents the principal syn-faulting depositional packages, with the latter sequence showing significant changes in both thickness and facies type across faults (Dart et al. 1993, Bonson et al. 2007).

The late syn-rift succession

The platform and slope facies at the top of the Upper Coralline Limestone Formation compose the late syn-rift phase strata on the Maltese mainland. The formation is exposed in the hangingwall of the westernmost 2,5 kilometers of the Maghlaq Fault outcrop (Southwest Malta). Here, significant facies differences between the footwall and the hangingwall can be recognized; with platform facies deposited on the footwall, and a 30 meters thicker succession of slope facies deposited in the hangingwall depression. Based on these facies, the palaeo-fault scarp relief is estimated to tens of meters (Dart et al. 1993, and references therein).

Offshore, the notable reflector marking the top of the Upper Coralline Limestone interval is a regional erosional unconformity recognizable throughout the Mediterranean. This inconformity marks a significant hiatus, related to the Messinian salinity crisis, during which the Maltese region possibly formed an upland karst plateau. In the Pantelleria Rift, the Upper Coralline Limestone reflector interval expands, and exhibits thickness increase in the hangingwall of up to 400 meters (Dart et al. 1993).

Thick Pliocene- Quaternary successions are present offshore Malta, where marls and carbonate mudstones overlies the Upper Coralline Limestone interval. The succession was deposited when the central Mediterranean reflooded, and shows significant stratal growth of several hundred meters down hangingwall dip slopes in major faults (Dart et al. 1993). However, Pliocene deposits are absent onshore Malta, and patchy Quaternary marine deposits are restricted to the northwest and southeast margins of Malta (Bonson et al. 2007). Caves and karstic surface depressions containing land-dwelling mammals (Pedley et al. 1976) and the lack of significant sediment thicknesses, suggests that the Post-Messinian Malta remained emergent to present day (Dart et al. 1993, Bonson et al. 2007).

3.2.3   Post- Rift

During the late Quaternary, biogenic, hemi- pelagic and turbiditic muds were deposited in the Pantelleria Rift. The present- day seabed shows no indication of significant fault movement,

indicating that deposition today occurs in the post- rift phase. Onshore Malta, fault scarps have retreated remarkably, resulting in deposition of Quaternary alluvial fan and tallus sediments (Dart et al. 1993). These deposits in addition to caliche soil profiles, conglomerated and calcrete breccias compose the youngest deposits on the island (Pedley et al. 1976, Pedley et al. 1978).

4. Field observations and data

The purpose of this chapter is to present and analyze data collected in the field. This chapter starts with a brief introduction of the structural and stratigraphic framework of the area. Further, as the main focus of this chapter, field characteristics of the deformation bands recorded along scanlines will be presented, including their thickness, orientation and frequency, respectively. The data is analyzed using steronets, graphs and histograms.

4.1 Geology of study area

4.1.1   Structural framework

The large-scale structure of the Maghlaq Fault is described by Bonson et al. (2007); a brief summary will be presented in the following as context for the present study.

The Maghlaq Fault is exposed along a 4 kilometer long coastal outcrop in southwest Malta, where the fault offset the Oligo-Miocene pre- to syn-rift carbonate succession by a minimum of 210 meters (Fig. 4.1). Based on stratigraphic thickness of the exposed footwall (above present-day outcrop), together with preserved fault rock porosity and lack of significant pressure solution features (e.g. stylolites), the burial depth at the time of faulting in Miocene was probably very shallow, i.e. less than 300 meters.

In term of geometry, the Maghlaq Fault is a left-stepping, en echelon normal fault array, comprised of relatively straight WNW-ESE trending fault segments. Based on movement striations, corrugations and polish marks of the footwall slip surface, the normal displacement is mostly perfectly dip-parallel, sometimes with a minor sinistral component. Over most of its length, the Maghlaq Fault is a relatively simple structure, composed of two principal slip surfaces that bound deformed rocks stacked in stratigraphic order from footwall to hangingwall. Nevertheless, areas of more complex geometry are found at branch-lines and bends in the fault trace. These are interpreted to be sites of linkage of the fault segments that initially were arranged in an en echelon geometry.

The study area is located between Ghar ix-Xaghra and Ras il-Bajjada, where a large segment of Globigerina Limestone Formation is bounded by two principal fault traces of the Maghlaq Fault, trending approximately NW-SE with dip towards SW (Fig. 4.1). Nevertheless, only the northern fault trace is observable in the field, whereas the trace of the southern fault segment is interpreted to be located offshore, and will thus not be further emphasized here. In the western boundary of the study area, a smaller NE-SW trending fault intersects the northern fault segment. As a result, the Oligocene (Chattian) Lower Coralline Limestone Formation is juxtaposed against the Miocene (Aquitanian) Globigerina Limestone Formation in both extremes of the study area. The stratigraphic relationship across the Maghlaq Fault in the study area, suggests a minimum displacement of 50 meters. In the hangingwall of the Maghlaq Fault, an approximately 350 meters long, and 20 meters wide outcropping section of Globigerina Limestone Formation was studied, throughout which deformation bands are nicely exposed. The outcropped formation is frequently disrupted by smaller intrablock faults, which offsets the strata by less than 3 meters. The faults in the study area are further described in section 4.1.2.
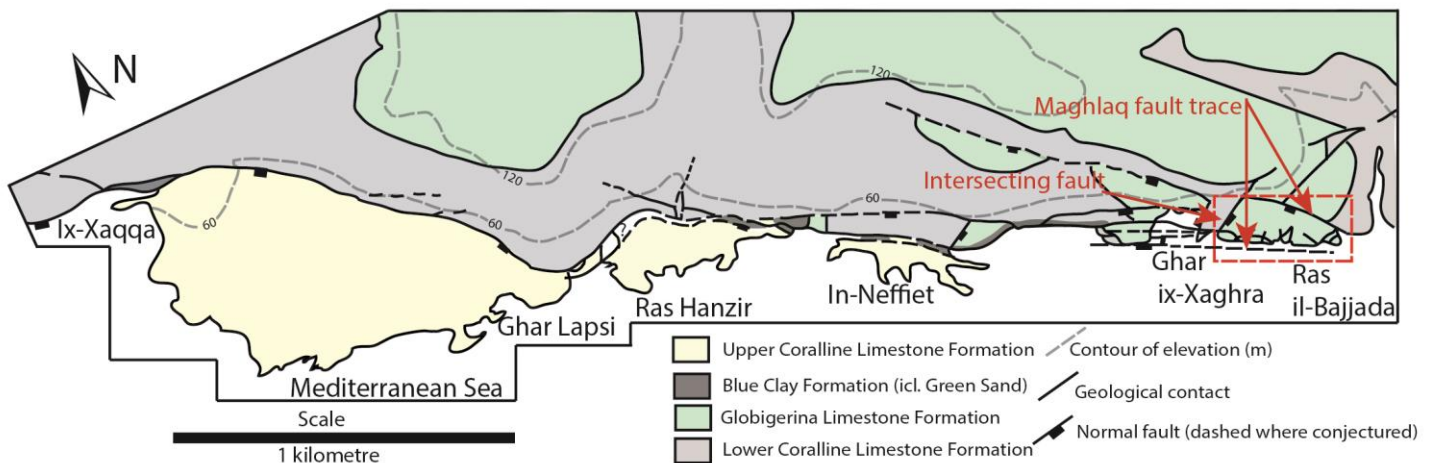
Figure 4.1: Geological map of the Maghlaq Fault, modified from Bonson et al. (2007). Topographic intervals are in meters above sea level. Note that the individual members of the stratigraphic formations are not distinguished on the map. The location of the study area is marked with a dashed red square, between Ghar ix-Xaghra and Ras il-Bajjada. The two fault traces of the Maghlaq Fault, and the intersecting fault are shown with a red arrow.

4.1.2   Fault orientation trends

Principally, two larger faults bound the study area: i) The Maghlaq Fault (MF) in the eastern part (MF in Fig. 4.2A), and ii) a intersecting fault (*sensu* Fossen et al. 2005) in the western part (IF in Fig. 4.2B). In addition to these larger faults in the eastern and western periphery of the study area, several smaller intrablock faults (IBF) frequently offset the exposed strata by less than 3 meters (IBF1-4 in Fig. 4.2C, D, E and F). The measured fault orientations were plotted in equal area stereonet (lower hemisphere), and will be presented below.

The tip region of the Maghlaq Fault segment is well exposed in the eastern part of the study area, and is oriented WNW-ESE with average dip of 66° towards SSW (MF in Fig. 4.3). The intersecting fault in the western boundary, is striking NE-SW with dip towards SE (IF in Fig. 4.3 and Fig. 4.1). Nevertheless, due to topographic difficulties, precise measurements of this fault could not be carried out.

The majority of the smaller intrablock faults are oriented with an angle to the overall Maghlaq Fault trend (IBF1-4 in Fig. 4.3), where IBF1, IBF2 and IBF3 reveal similar trends, striking ENE-WSW with 55°-60° dip towards SE. Consequently, these are oriented sub-parallel to the intersecting fault (IF in Fig. 4.3). In contrast, IBF4 is oriented NW-SE with 71° dip towards SW, equivalent to the trend of the Maghlaq fault segment (IBF4 in Fig. 4.3). See Appendix III for more detailed fault data.
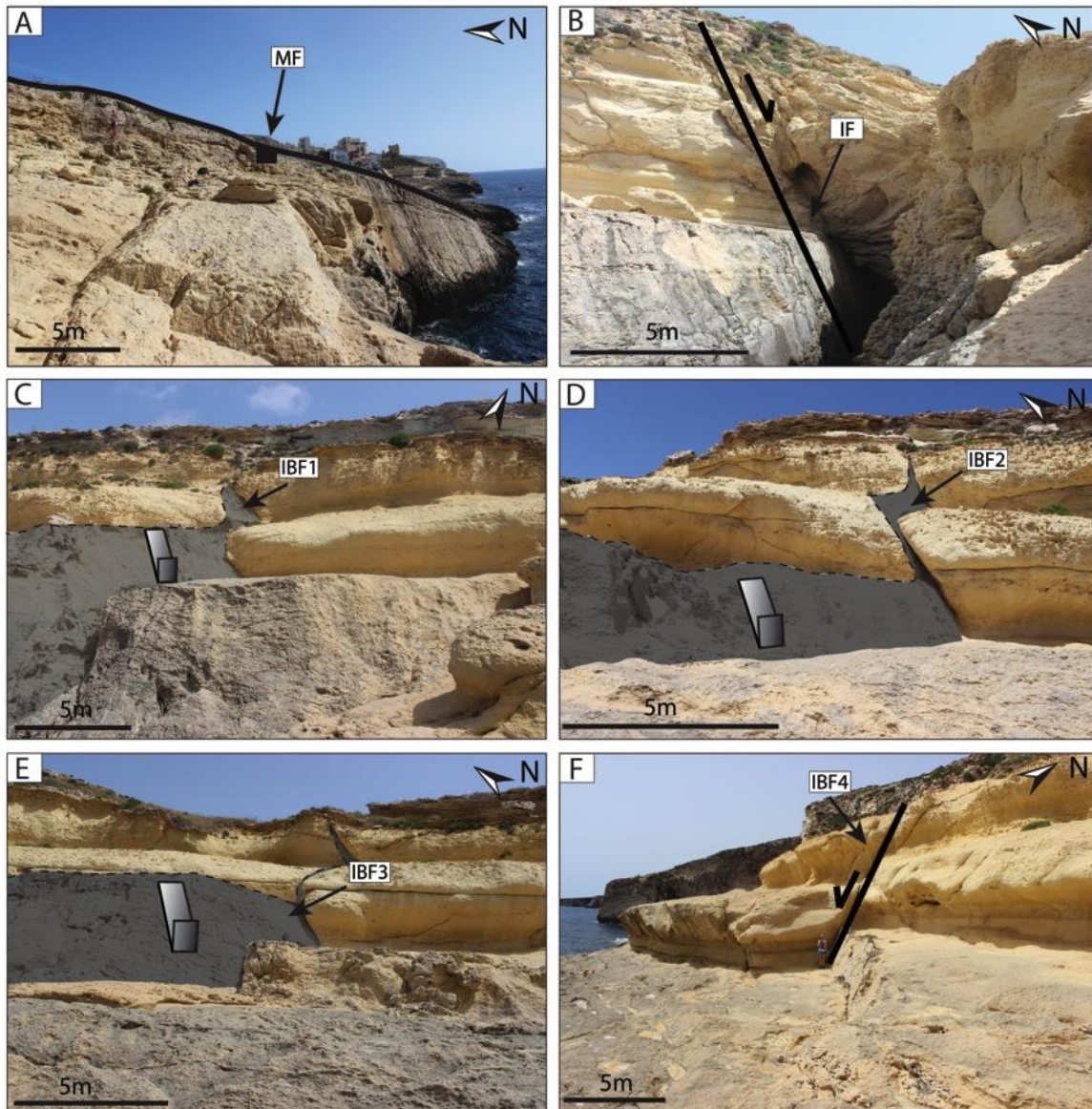
Figure 4.2: Two larger faults bound the study area in the eastern and western part. Additionally, several smaller intrablock faults (IBF) offset the exposed strata within the area by less than 3 meters. A) Exposed tip region of the WNW-ESE trending Maghlaq Fault segment (MF), where Lower Coralline Limestone Formation is juxtaposed with Globigerina Limestone Formation. The principal slip surface is well exposed for c. 16 meters. B) NNE-SSW trending fault, intersecting the Maghlaq Fault segment in the western boundary of the study area, referred to as IF. In the proximity of the slip surface the beds are sub-vertical. Note that due to topographic difficulties, it was not possible to obtain precise orientation measurements of this fault. C) Smaller intrablock fault (IBF1) in the eastern most part of the study area, closest to the Maghlaq Fault segment (MF). The fault is oriented NNE-SSW, parallel to the intersecting fault (IF) that bounds the study area in the west. D) Intrablock fault (IBF2), located approximately 50 meters further west from IBF1. This fault is oriented NE-SW, and is thus sub-parallel to the intersecting fault (IF). E) Additional 30 meters west of IBF2, is the NE-SW oriented IBF3. As IBF1 and IBF2, it is oriented sub-parallel to the intersecting fault (IF). F) The NW-SE trending IBF4 is the only intrablock fault within the area that is oriented parallel to the Maghlaq fault segment (MF).
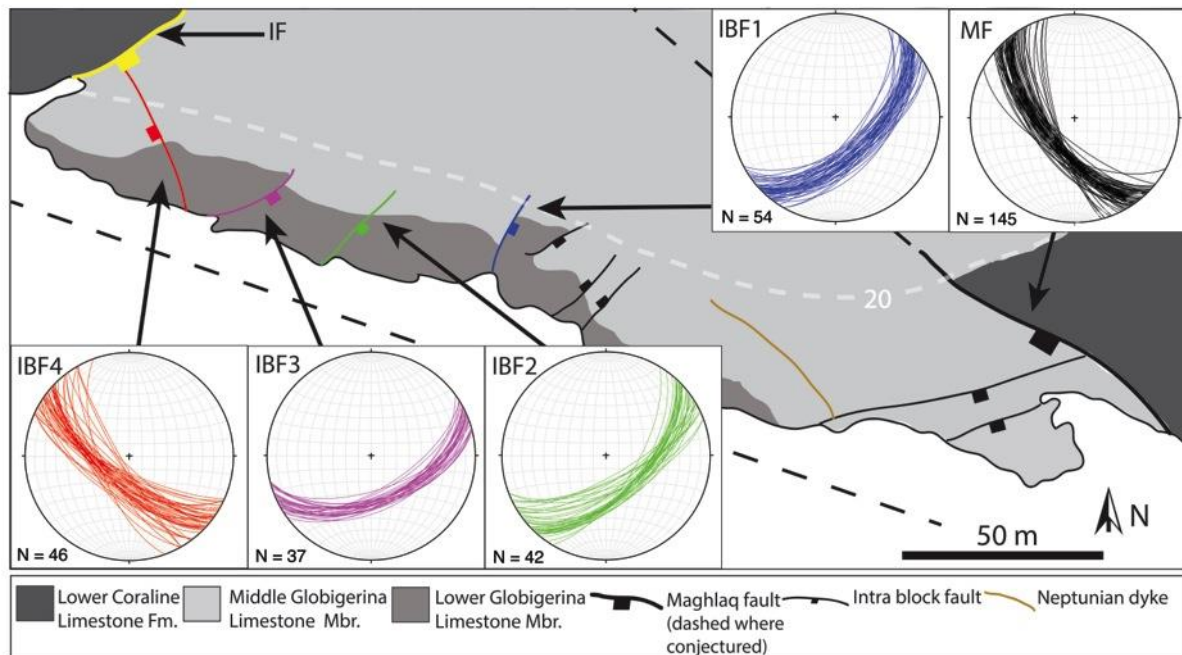
Figure 4.3: Mapped fault orientation trends, based on Bonson et al. (2007) and field observations. Location of this figure is shown with a red, dashed square in **Figure 4.1**. Topographic interval is in meters above sea level. Note that smaller faults with minor/negligible offset (>1 m) indicated with a black line are neglected for this study. As illustrated by the equal area (lower hemisphere) projections, the majority of the smaller intrablock faults (IBF1-3) are oriented approximately ENE-WSW with average dip ranging from 55-60° towards SE. These faults are thus oriented parallel to sub-parallel with the intersecting fault in the western boundary of the study area (IF). Due to topographic difficulties, it was not possible to obtain precise measurements of this intersecting fault. Nevertheless, IBF4 is the only mapped intrablock fault with similar trend as the Maghlaq Fault segment, striking NW-SE with average dip ranging from 65-71° towards SW. The bedding dip in the area is practically horizontal.

4.1.3   Stratigraphic framework

The stratigraphic interval of interest in the present study is the Globigerina Limestone

Formation of Aquitanian to Serravallian age. This formation represents the pre-rift to early-

syn rift period in the area (see section 3.2 for further details). Based on field observations (i.e.

visual change in lithofacies, fossil content and sedimentary/tectonic structures), the exposed

formation can be subdivided into six (from older to younger; Fig.4.4): Unit L1, Unit 1M, Unit

2M, Unit 3M, Unit 4M, Unit 5M, Unit 6M and Unit 7M. Unit L1 represents the Lower part of

the Globigerina Limestone Formation, while Unit 1-7 M represents the Middle part of the

Globigerina Limestone Formation. Since the other formations of the Maltese stratigraphy

(Fig. 3.3) are not present in the study area, they will not be further described in any detail

here.
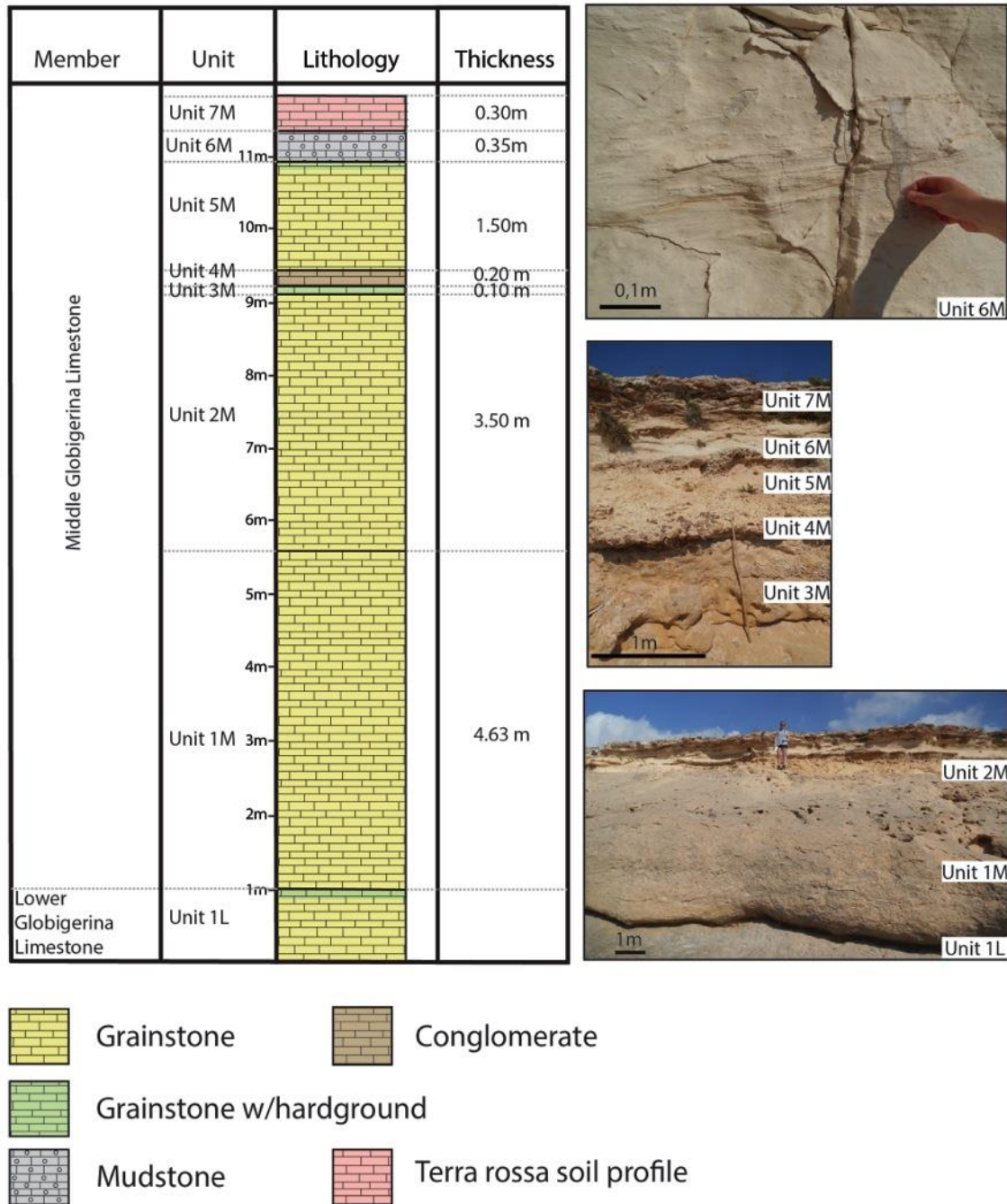
Figure 4.4: Lithostratigraphic column of the study area. From field observations, Middle and Lower Globigerina Members can be divided into sub units based on visual change in lithofacies, (sedimentary and tectonic) structures and fossil content. In general, the dominating lithofacies is grainstone, with occasional increase of mud-content to packstone or mudstone.

Unit 1L

Unit 1L is a part of the Lower Globigerina Limestone Member, representing the pre-rift carbonates exposed in the study area. Thickness measurements of the unit are problematic, due to the boundary between Lower Coralline Limestone Formation and the overlying Globigerina Limestone Formation being below sea level. The unit consists of a rather uniform

succession of pale-grey grainstone, characterized by bioturbation and frequent fragments of macrofossils, specifically bryozoans and coralline algae. In the uppermost part, the grainstone is capped by a 10cm thick hardground surface, marking the boundary between Lower Globigerina Limestone Member and Middle Globigerina Limestone Member. The formation contains small amounts deformation bands (*c.* 1 deformation band per meter).

Unit 1M and Unit 2M

The subsequent Unit 1M comprises the lowermost part of the Middle Globigerina Limestone Member, marking the onset of early syn-rift carbonates in the field area. Thickness measurements of the exposed unit in the area yield a stratigraphic thickness of 4.6 meters. Also this unit is mainly composed of grainstone, but with somewhat brighter yellow color. Bioturbation is evident to some extent in the lower part, distinguished by a grey-yellow color. Moving further upward in the unit, bioturbation becomes absent. However, in the uppermost 40 centimeters of the unit, a transition zone can be recognized, where the amount of bioturbation increases and becomes prevailing at the very top of the unit. The succeeding 3.5 meters thick Unit 2M, is characterized by orange-brown grainstone, also with abundant bioturbation. Here, the bioturbation is phosphorized, and thus more resistant to weathering, forming protruding features. The macrofossil assemblage for the aforementioned units is similar, with the presence of echinoids and bivalves. Within Unit 1M, deformation bands are abundant within the interval where bioturbation is absent, reaching frequencies of approximately 12 deformation bands per meter. The other units, however, do not contain any deformation bands.

Unit 3M, 4M, 5M, 6M and 7M

A distinct boundary can be recognized between Unit 2M and the overlying Unit 3M, characterized by a 10 centimeters thick of patchy hardground within an orange-brown grainstone matrix. The hardground is recognizable by a characteristic honeycomb weathering. Directly over this hardground is a 20 centimeters thick layer with brown phospahtic conglomerates within a massive echinoid-rich pack-to grainstone matrix, composing Unit 4M. The diameter of the clasts ranges from 1-5 centimeters. Additionally, this unit has a high content of macrofossils, specifically molluscs and shark teeth. Smaller pebbles equivalent to the phosphatic conglomerate of Unit 4M is sporadic distributed within yellow grainstone matrix in Unit 5M. This unit is in total 1.5 meters, with a transitional zone from yellow grainstone to pale yellow-white packstone the last 20 centimeters. The very top of this unit is

capped by another 10 cm thick hardground, overlain by cross-bedded white mudstone composing unit 6M. The uppermost unit of the Middle Globigernia Limestone Member is a 30 cm thick limestone derived terra rossa soil profile (Unit 7M). None of these units contains deformation bands.

4.2 Deformation band characterization and spatial distribution

As previously described in section 1.5.2, deformation bands were systematically characterized by data collection along deformation band frequency scalines, oriented perpendicular to sub-perpendicular to the faults within the study area (depending on the outcrop) within the hangingwall of the Maghlaq Fault. Data collected along the scanlines include i) deformation band thickness, ii) deformation band orientation and iii) deformation band frequency, for both Lower and Middle Globigerina Limestone Members (Unit 1L and 1M described in section 4.1.3). Displacement of the deformation bands was generally not possible to record due to outcrop character and lack of marker horizons in the relatively homogenous host rocks. Details of the scanlines and the recorded measurements are found in Appendix I.

4.2.1   Deformation band description

In the investigated outcrops, deformation bands occur as arrays and appear as both single bands and clusters of narrow spaced bands. The deformation bands are bed-perpendicular, and easily distinguished from the host rock by a somewhat brighter color, and the fact that they occur as narrow ridges with positive relief. In general, the relief of a single band is a couple of millimeters, while the clusters might have relief up to some centimeters (compare Fig. 4.5A and B). Within Middle Globigerina Limestone Member, the arrays of deformation bands are uniformly distributed with mean frequencies of 2-9 per meter. Locally, the bands reveal some degree of variable orientation, resulting in a connective and anastomosing pattern (Fig. 4.5C and D). Frequently, deformation bands intersect, with negligible or no observable offset (Fig. 4.5E). Nevertheless, within Lower Globigerina Limestone Member, the majority of the represented deformation bands occur as single bands, generally with 2 bands per meter. Thus, with much larger spacing, the deformation bands within this limestone member comprise a much less complex pattern.

For individual bands, the most frequent thickness is between 1-5 millimeters. Bands thicker than ~10 millimeters are typically composed of many parallel bands, forming deformation band clusters, which occasionally reach thicknesses up to 40 millimeters (Fig. 4.6). The two studied limestone intervals exhibit some differences in average thickness of single deformation bands, where the average thickness in Middle Globigerina Limestone Member (3.3 millimeters) is somewhat larger than what is found in Lower Globigerina Limestone Member (2.9 millimeters; Fig. 4.6).

In thin section (Fig. 4.7A and B), the bands can be distinguished from the adjacent host rock by zones of more densely packed grains, featuring a darker color, with significantly lower porosity than the host rock. Micro-structural analysis performed in a parallel sister project at UiB, reveal granular flow as dominant deformation mechanism, resulting in grain reorganization and subsequent compaction. Additionally, some of the bands show evidence of grain crushing, causing higher content of fine-grained material in the core of the deformation bands. Based on these observations, most of the deformation bands in the field area can be classified as disaggregation bands, with occasionally occurrence of cataclasis.
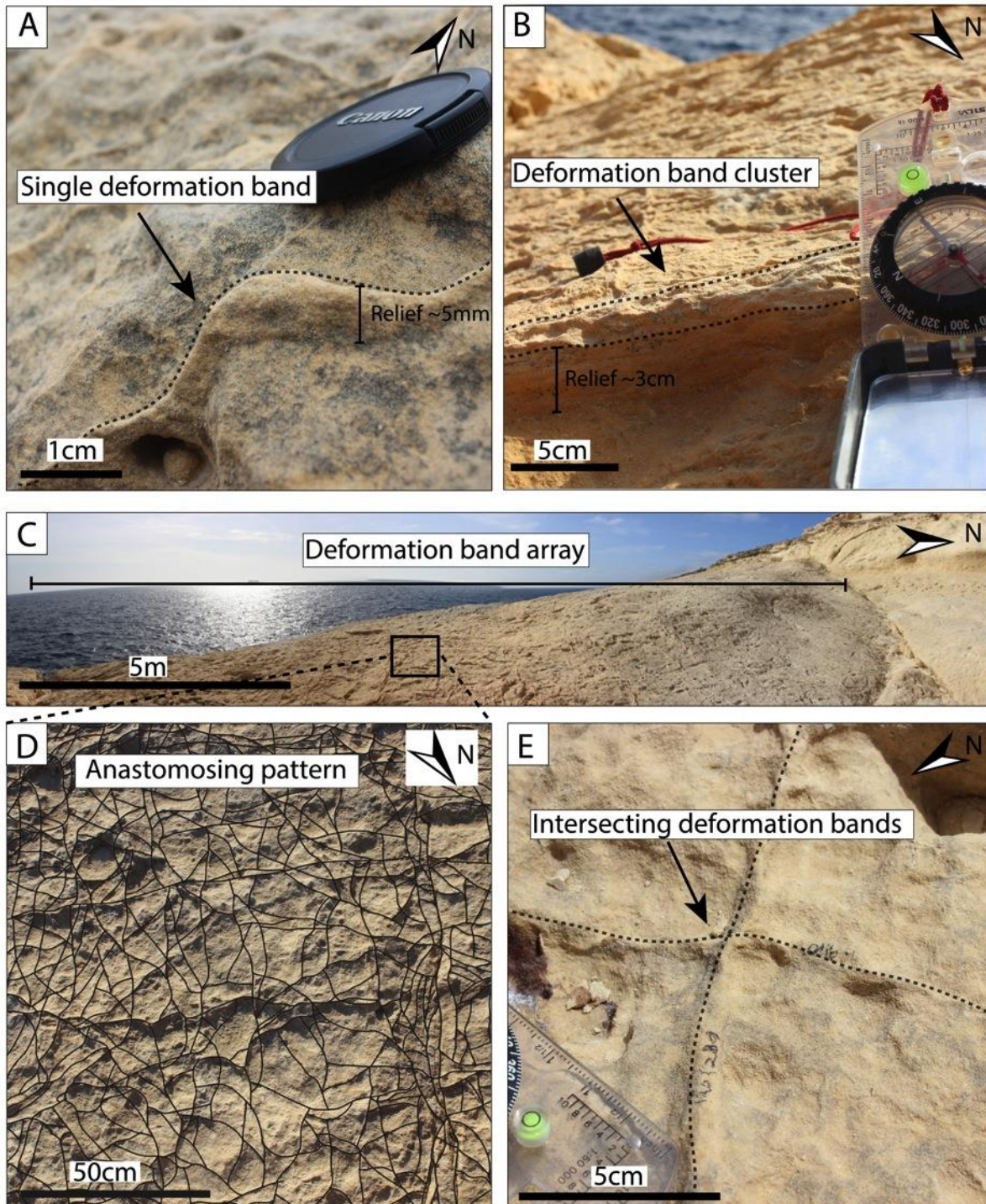
Figure 4.5: Field photos showing different features of the deformation bands. A) The relief of a single band is generally a couple of millimeters. B) Deformation bands clusters of closely spaced parallel bands usually have relief up to some centimeters. C) Deformation band array within Middle Globigerina Limestone Member, where deformation bands are highly abundant. D) Deformation bands mapped within 1 m x 1 m square in the Middle Globigerina Limestone Member, locally varying orientation coupled with close spacing results in a highly connective and anastomosing pattern. E) Two intersecting deformation bands, with no observable offset.
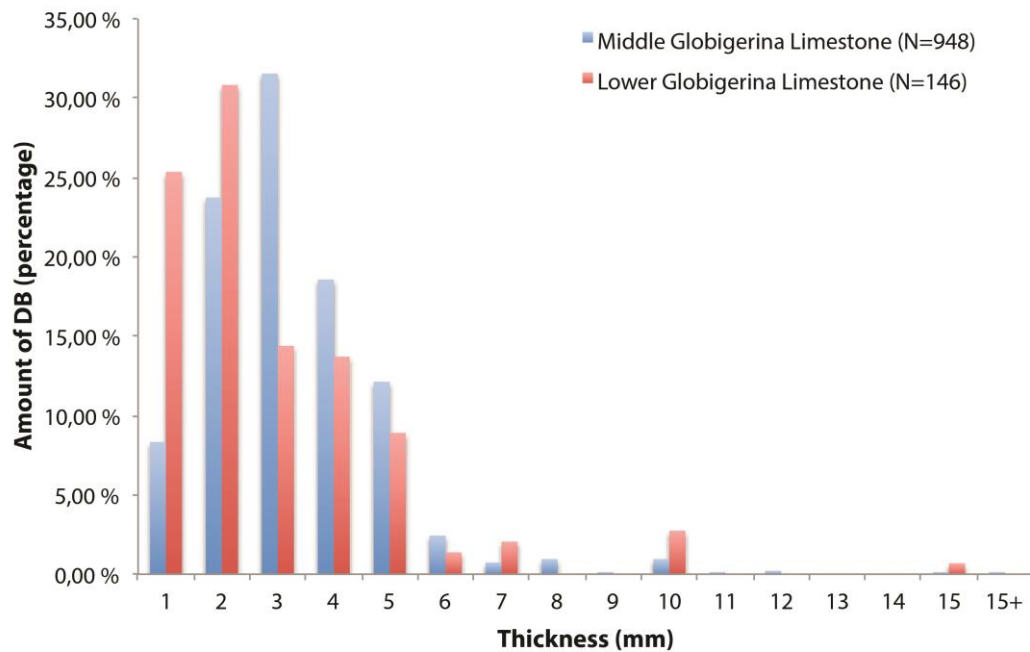
Figure 4.6: Percentage of deformation bands (DB) with varying thickness. The most frequent thickness of individual bands is between 1-5 millimeters, for both Lower and Middle Globigerina Limestone Members. Deformation band clusters are typically thicker than 10 millimeters. Note that single deformation bands are slightly thinner within Lower Globigerina Limestone Member, where average thickness is 2.9 millimeters. For Middle Globigerina Limestone Member the average thickness is 3.3 millimeters.
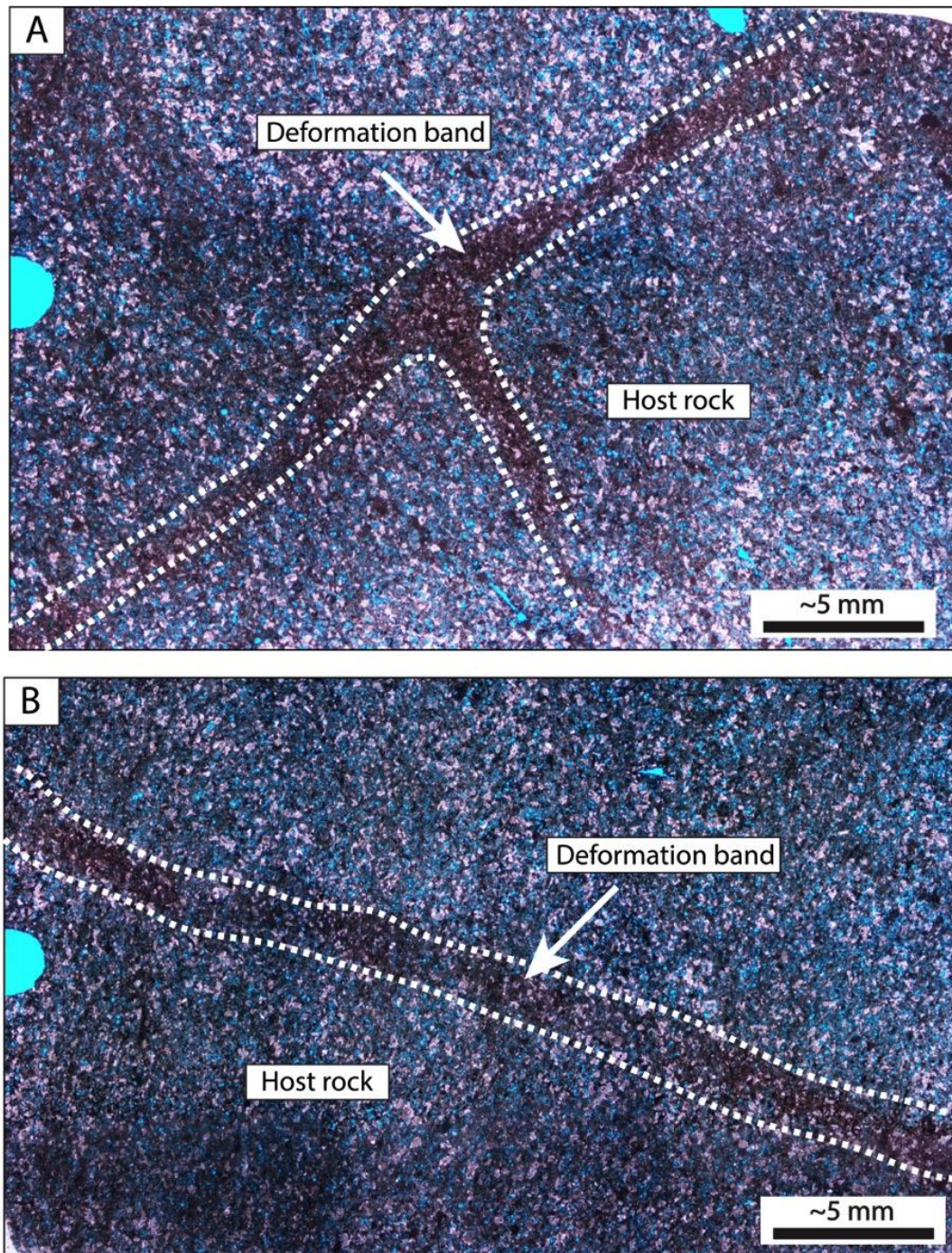
Figure 4.7: Photomicrographs of thin sections of deformation bands; epoxy saturating the pore space is blue. The deformation bands can be distinguished from the host rock by a darker color with more densely packed grains and lower porosity. A) Two deformation bands, where one abuts the other. There is a clear boundary between the host rock and the deformation bands. B) Single deformation band, with some variance in thickness. The photomicrographs of the thin sections were provided by Thorsheim (2015).

4.2.2   Deformation band orientation trends

In porous granular rocks, deformation bands are generally found in the damage zone of larger offset faults, and are commonly are oriented parallel to sub-parallel with the fault (e.g. Shipton & Cowie 2001, 2003). In such cases, where deformation bands have a preferred orientation, some authors have proposed that fluid flow parallel to these structures would be easier than flow across the structures (e.g. Antonellini et al. 1999, Fossen & Bale 2007, Fossen et al. 2007). Thus, complex variations of deformation band orientations have the potential to influence fluid flow in a complicated manner (e.g. Fossen & Bale 2007, Fossen et al. 2007).

Deformation band orientations were systematically measured along the scanlines and projected in lower hemisphere, equal area rose diagrams for both Lower and Middle Globigerina Limestone Members, as illustrated in Figure 4.8 and Figure 4.9, respectively. Further, the deformation band orientation trends were compared with the fault trends in the area (Fig. 4.3).

Deformation band orientations were measured along six scanlines within the Lower Globigerina Limestone Member (denoted SL in Fig. 4.8), where a wide range of deformation band orientations are displayed. However, despite the scatter in orientations data, the vast majority of the deformation bands are oriented ENE-WSW and NE-SE, in the eastern and western part of the exposed unit (SL 1+2, 5 and 6; Fig. 4.8), and is thus oriented sub-perpendicular to the overall NW-SE Maghlaq Fault trend (MF; Fig. 4.3). Contrastingly, the less frequent but yet abundant NW-SE and WNW-ESE striking deformation bands in the central part of the unit (SL 3+4; Fig. 4.8), are parallel to sub-parallel oriented with respect to the Maghlaq Fault. Due to limited exposures of deformation band planes, only 13 measurements were made of the dip. The dip varies between 64° -80° towards SE and SW.

In terms of orientations relative to the smaller intrablock faults in the area, the prevailing ENE-WSW and NE-SW trending deformation bands have parallel to sub-parallel orientations with the predominant intrablock fault trend, and likewise, the larger intersecting fault in the western boundary of the study area (IBF1-3 and IF; Fig. 4.3). Accordingly, the abundant NW-SE and WNW-ESE striking deformation bands are oriented parallel to sub-parallel with the

westerly intrablock fault (IBF4; Fig.4.3), and thus oblique to the intersecting fault and the remaining intrablock faults (IF and IBF1-3; Fig. 4.3).
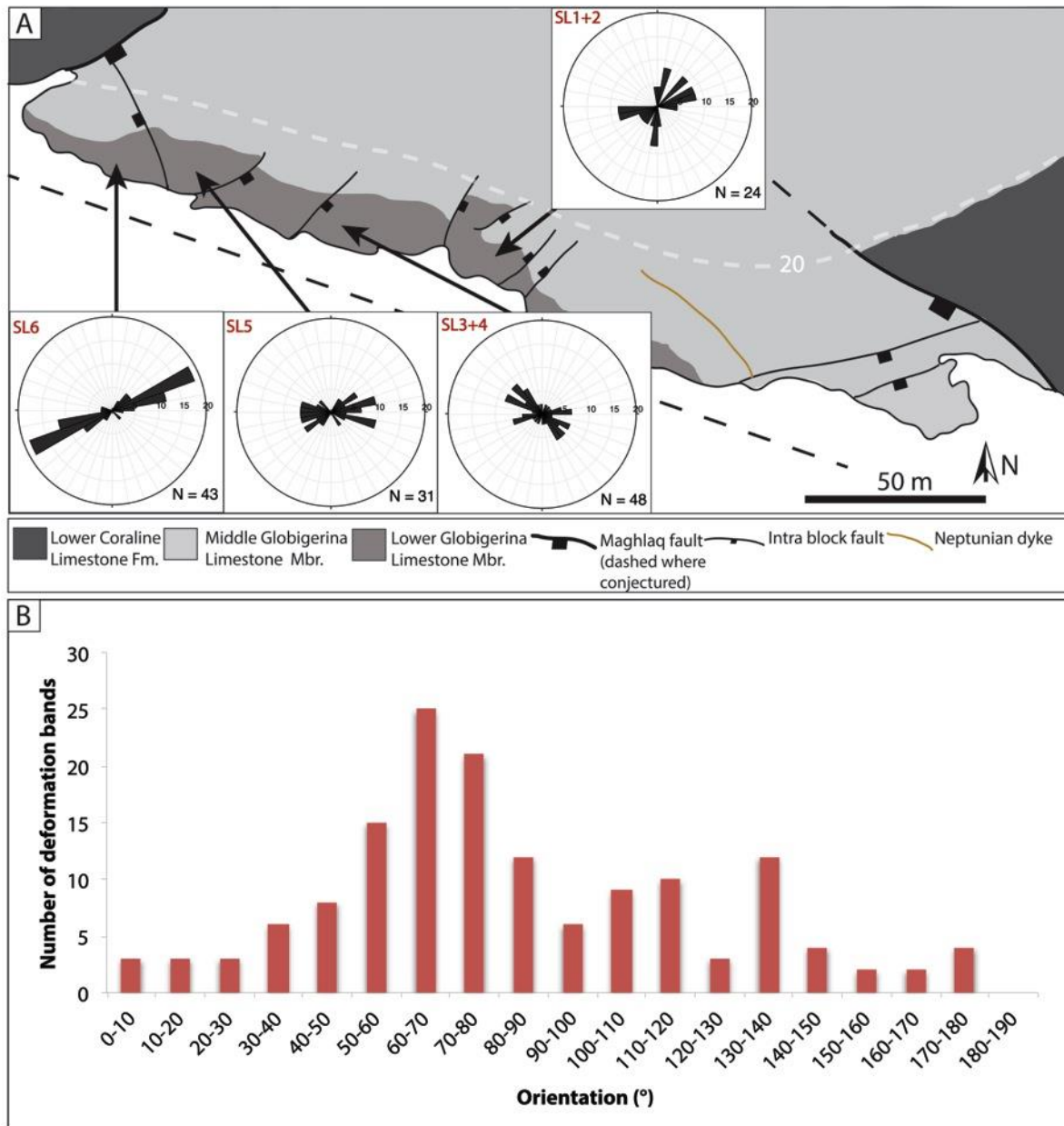
Figure 4.8: Mapped deformation band orientation trends in the field within the Lower Globigerina Limestone Member. A) Location of this figure is shown in **Figure 4.1**. As illustrated by the equal area (lower hemisphere) rose diagrams, there is some scatter in the orientation data. The vast majority of the deformation bands are oriented ENE-WSW and NE-SW. Additionally, NW-SE and WNW-ESE trending deformation bands are frequent. Note that a total of six scanlines (denoted SL) were conducted within the Lower Globigerina Limestone Member, where scanline 1 & 2 and scanline 3 & 4 have been combined in the stereonets (hence denoted SL1+2 and SL 3+4). Lower Globigerina Limestone Member is not exposed for outcrop studies in the westernmost 105 meters of the study area. Topographic intervals are in meters above sea level. B) Histograms with measured orientations of the deformation bands from 0-180° plotted against number of deformation bands. As illustrated in the figure, there is some scatter for the measured orientations of the deformation bands within the Lower Globigerina Limestone Member. Nevertheless, the majority of the deformation bands strikes NE-SW and ENE-WSW (50-90°)**.**

Deformation band orientations were measured along nine scanlines within the Middle Globigerina Limestone Member (denoted SL in Fig. 4.9), where the deformation bands reveal limited variation in strike. The majority of the deformation bands are oriented ENE-WSW to NE-SW, sub-perpendicular to the overall NW-SE Maghlaq Fault trend. Additionally, in the eastern most part of the study area (SL1; Fig. 4.9A), a small amount of the deformation bands are oriented NW-SE, and are hence parallel to sub-parallel with the Maghlaq Fault. Only a restricted number of measurements were made of the band dip, due to limited exposure of deformation band planes. However, a total of 20 measurements were made, revealing 60°-86° dip towards SE.

In general, the Middle Globigerina Limestone Member display similar deformation band orientation trends as the Lower Globigerina Limestone Member, i.e. trending ENE-WSW to NE-SW, sub-perpendicular to the Maghlaq Fault and the westerly intrablock fault (MF and IBF4; Fig. 4.3). Anomalously, the NW-SE trending deformation bands in the eastern part of the study area are oriented parallel/sub-parallel with the Maghlaq fault, and are thus sub-perpendicular to the IF and the majority of the smaller intrablock faults (IBF1-3 and IF; Fig. 4.3).
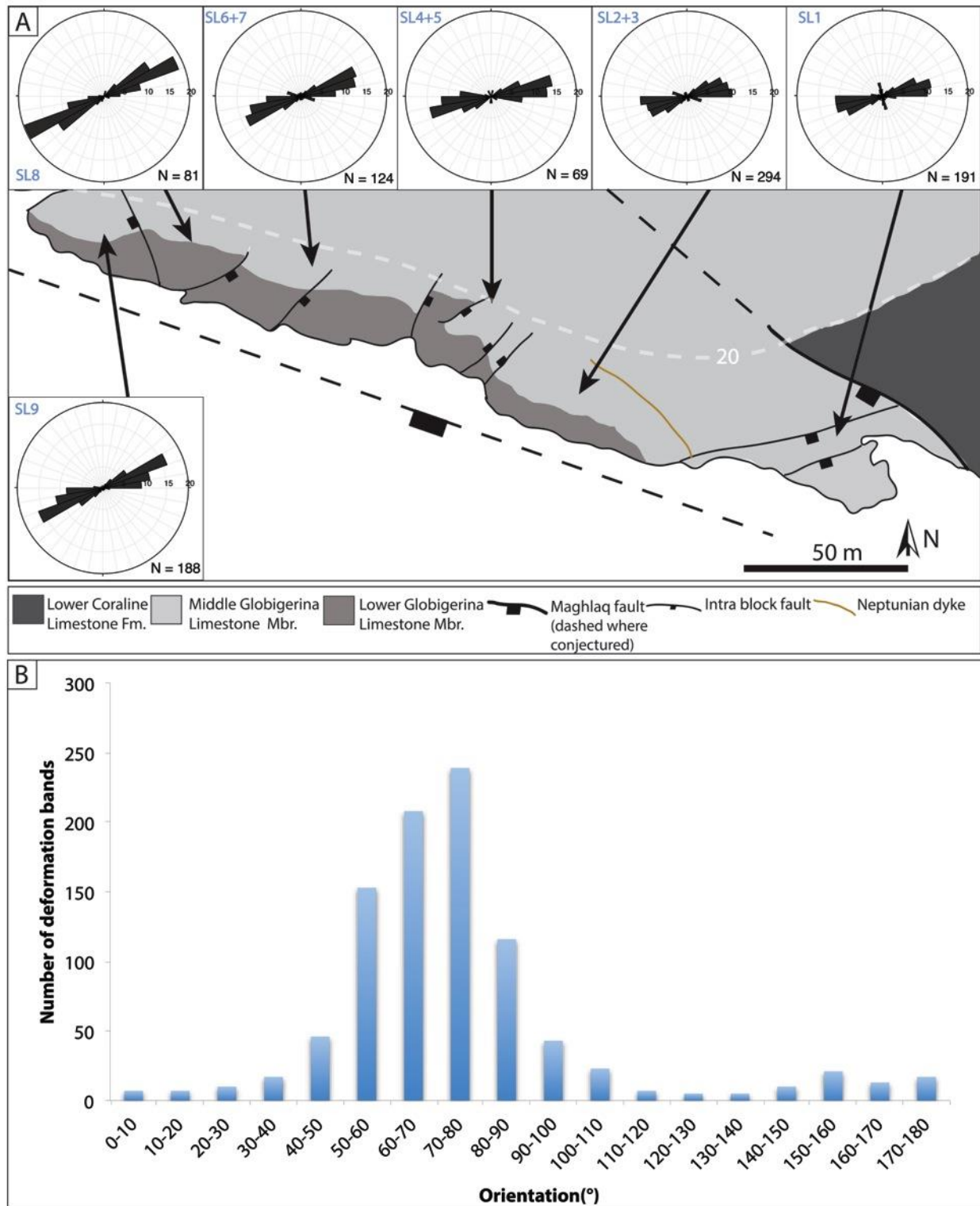
Figure 4.9: Mapped deformation band orientation trends in the field within the Middle Globigerina Limestone Member. A) Location of this figure is shown in **Figure 4.1**. The equal area (lower hemisphere) rose diagrams reveal a predominating ENE-WSW to NE-SW orientation trend of the deformation bands. Additionally, in the eastern most part of the study area (SL1), a subordinate trend of NW-SE is apparent. Note that a total of nine scanlines (denoted SL) were conducted within the Middle Globigerina Limestone Member, where scanline 2&3, 4&5 and 6&7 have been combined in the stereonets (hence denoted SL2+3, SL4+5 and SL 6+7). Topographic intervals are in meters above sea level. B) Histograms with measured orientation of the deformation bands from 0-180° plotted against number of deformation bands. As illustrated in the figure, there is a clear trend, where the majority of the deformation bands are striking NE-SW to ENE-WSW (50-90°)

4.2.3   Deformation band frequency variations

In order to characterize spatial distribution of deformation bands, the deformation band frequencies were systematically mapped by counting the number of deformation band intersection per meter along the aforementioned scanlines. The frequency variations is presented by comparing i) deformation band frequency for Lower and Middle Globigerina Limestone Members (LGLM and MGLM) and ii) frequency variation with distance from Maghlaq Fault.

Average deformation band frequency (with max and min values) recorded throughout LGLM is displayed in Table 4.1. The highest recorded frequency is 4 deformation bands per meter, whereas the average frequency is 1.5 bands per meter. Figure 4.10A presents the average deformation band frequency for all the scanlines, from east to west within this limestone member. There is no significant frequency variation along the measured profile, and for all scanlines there are generally 2 deformation bands per meter. Note that LGLM is not exposed the first 105 meters along the measured profile.

The frequency variations within the MGLM are shown in Table 4.1. This limestone member reaches a maximum frequency of 12 deformation bands per meter, whereas the average frequency throughout MGLM is 5.3 bands per meter. Figure 4.10B, shows average frequency changes for all the scanlines conducted in MGLM. There is a steady increase in average frequency from 5 to 9 deformation bands per meter in the interval from 0 to 105 meters along the profile (SL1 to SL3; Fig. 4.10B). A subsequent decrease is observed from 105 to 131 meters (SL3 to SL5; Fig. 4.10B), where the average frequency in the latter is 1.5 deformation bands per meter. In the following interval between 131 and 271 meters (SL5 to SL8; Fig. 4.10B), the average deformation band frequency gradually increases to 4 bands per meter. Further, an abrupt increase in deformation band frequency is apparent from 271 meters to the westernmost extreme of the exposed unit, reaching a frequency of 7.5 bands per meter (SL9; Fig. 4.10B).

Middle Globigerina Limestone Member shows a persistently higher average frequency throughout the formation, compared to the Lower Globigerina Limestone Member (Table 4.1). In general, the average number of deformation bands per meter is 3.5 times higher in MGLM, reaching maximum frequency of 12 bands per meter. Comparatively, the highest

recorded frequency in LGLM is 4 bands per meter. However, the lowest recorded deformation band frequency for both limestone members are 0 bands per meter. In terms of frequency variations along the measured profile, there are larger variations along the scanlines in MGLM, whereas the frequency is more or less constant throughout LGLM (Fig. 4.10A and B).

Table 4.1: Average deformation band frequency per meter for all scanlines in the Lower and Middle Globigerina Limestone Members. Abbreviation: DB= deformation band.

	Average frequency (DB per meter)	Max	Min	Number of scanlines
Lower Globigerina Limestone Member	1.5	4	0	6
Middle Globigerina Limestone Member	5.3	12	0	9
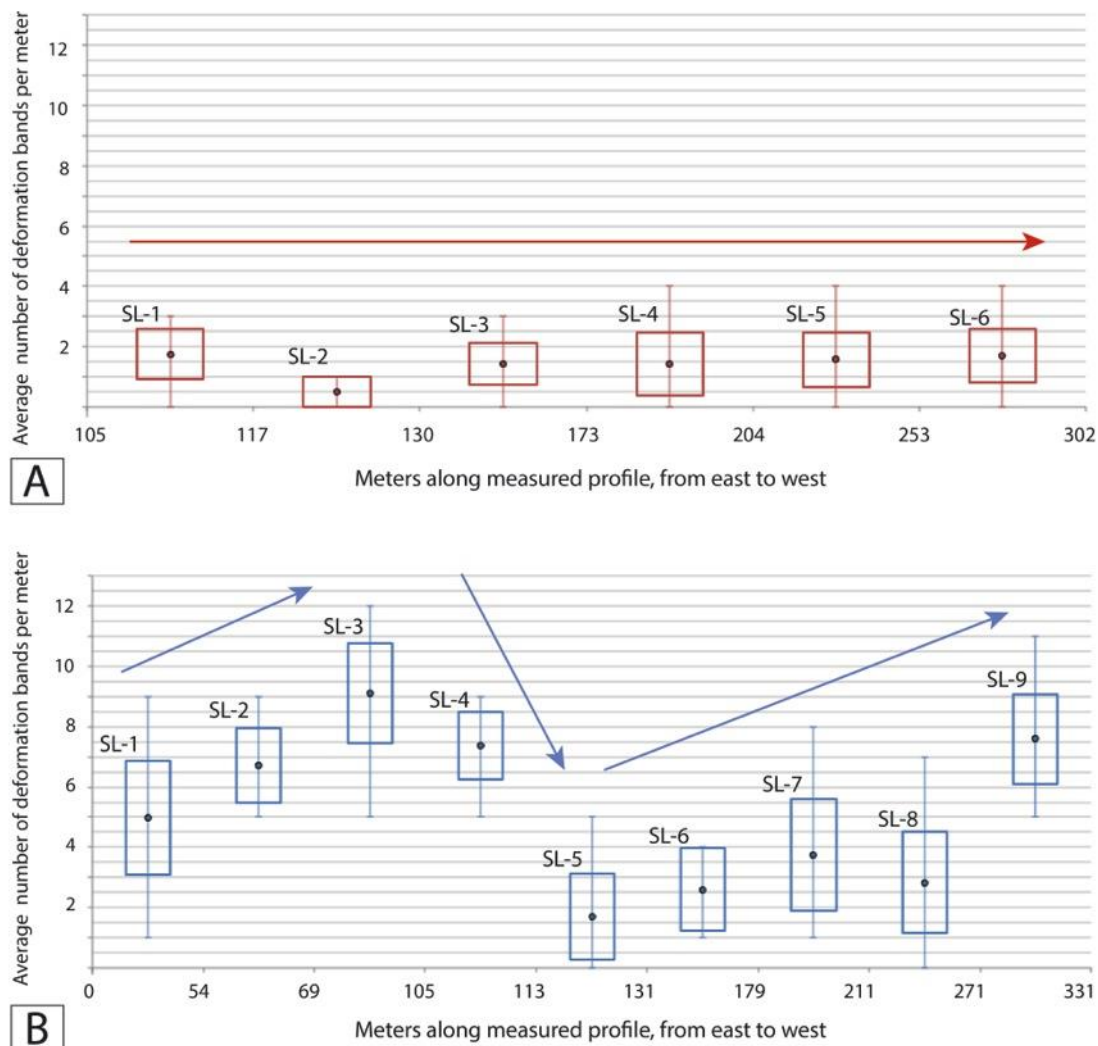
Figure 4.10: Measured deformation band frequency along scanlines in Lower Globigerina Limestone Member (Sc1-6) and Middle Globigerina Limestone Member (Sc1-9). For each scanlines average deformation bands per meter are shown with a point, standard deviation with a box and maximum and minimum values as a line. Note that the Maghlaq Fault slip surface corresponds to 0 meters along measured profile. A) Deformation band frequency for all scanlines within Lower Globigerina Limestone Member. Note that this limestone member is not exposed the first 105 meters along the measured profile. As illustrated by the frequency trend-arrow, there are no significant variations along the profile, and for all the scanlines there is averagely 2 deformation bands per meter. B) Frequency variations along the scanlines conducted in Middle Globigerina Limestone Member, where an arrow illustrates the frequency trend. In the interval from 0 to 105 meters, the average frequency increases from steadily from 5 to 9 deformation bands per meter. A subsequent decrease is observed from 105 to 131 meters, from 9 to 1.5 deformation bands per meter. In the following interval between 131 to 271 meters, the average deformation band gradually increases from 1.5 to 4 deformation bands per meter. An abrupt increase is apparent from 271 meters to the western most extreme of the exposed unit, reaching a frequency of 7.5 bands per meter.

Figure 4.11, shows a graph of how the deformation band frequency changes along the measured profile from east to west, with a distance up to 115 meters away from the Maghlaq Fault. As indicated by the graph, Lower Globigerina Limestone Member does not reveal any noteworthy frequency peaks with varying distance from the Maghlaq Fault. Even though there are some small variations, ranging from 0 to 4 deformation bands per meter, the overall

change is not significant. Nevertheless, within Middle Globigerina Limestone Member, there are larger variations in frequency. In the most proximal 2 meters from the slip surface, MGLM is intensely deformed, and due to the chaotic texture of the rock deformation band frequencies are difficult to record. However, at distances exceeding about 50 meters from the fault, the total number of deformation bands ranges from 1 to 9 deformation bands per meter. The proceeding interval between 50 to 85 meters, the average is somewhat higher, ranging from 5 to 12 deformation bands per meter. Further, between 85 and 100 meters away from the fault, larger parts of MGLM are not exposed. In the most distal part, however, between 100-115 meters from the fault, the deformation band frequency shows a general decrease. Nevertheless, an abrupt increase is apparent around 115 meters, where the frequency ranges from 5 to 11 deformation bands per meter. This latter interval is in the proximal part of the intersecting fault (IF) situated in the western part of the study area.

The overall frequency trend in MGLM reveals two distinct frequency peaks between 50-85 meters and around 115 meters away from the Maghlaq Fault. On the contrary, Lower Globigerina Limestone Members does not show any significant frequency changes with varying distances from the fault. For normal faults in sandstones, the spatial distribution of deformation bands is generally higher in the proximal part of the fault (e.g. Antonellini & Aydin 1995, Fossen et al. 2005). As seen from the graph there is no clear correlation between deformation band frequency and distance from the large Maghlaq fault, concerning both Lower and Middle Globigerina Limestone Members. Nevertheless, comparing the frequency with the other faults present in the area (IBF1-4 and IF; Fig. 4.11), the frequency is generally higher proximal to the faults, with a steady decrease away from the faults.
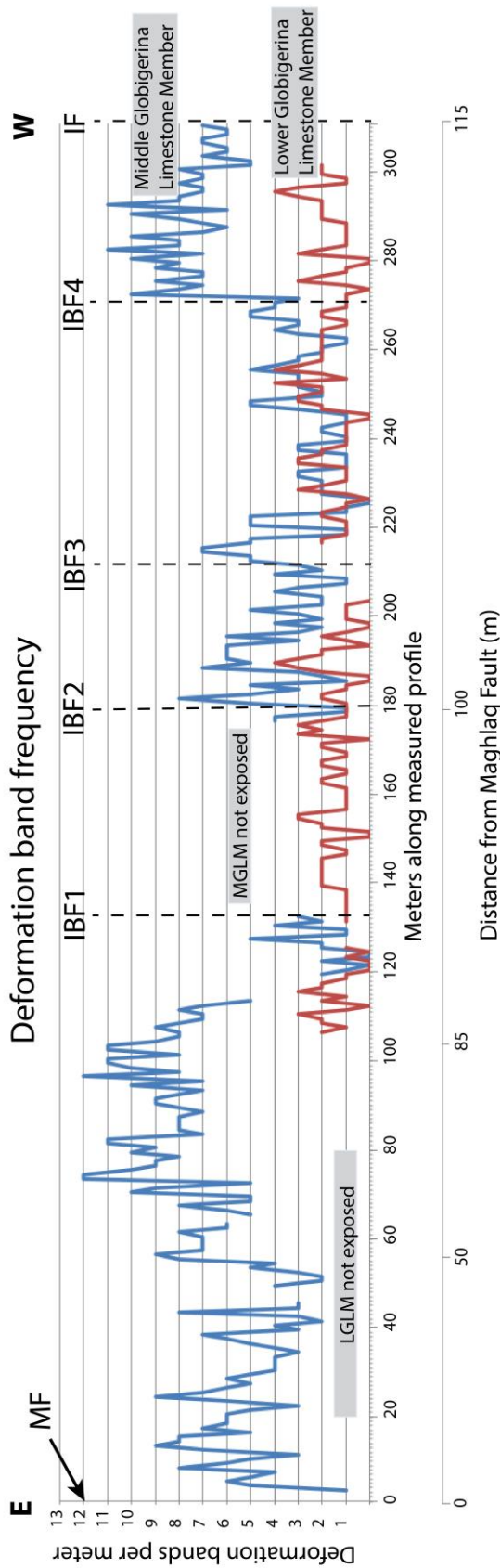
Figure 4.11: Graph illustrating the deformation band frequency with distance from Maghlaq Fault (lower most x-axis). The Lower Globigerina Limestone Member (LGLM) does not show any significant frequency changes with varying distance from the fault. On the contrary, the overall frequency trend in Middle Globigerina Limestone Member (MGLM) reveals two distinct frequency peaks between 50-85 meters and around 115 meters away from the Maghlaq Fault. Nevertheless, there is no clear correlation between deformation band frequency and distance from the Maghlaq Fault. Note that LGLM is not exposed the proximal 105 meters from the fault, and large parts of MGLM are not exposed between 85 and 100 meters from the fault. The location of the smaller faults within the area, i.e. intrablock faults (IBF1-4) and the intersecting fault (IF) are shown with dashed lines. Generally, the frequencies of deformation bands are higher in the most proximal part of the faults, and decrease with distance away from the faults.

50

5. Petrophysical properties

The purpose of this chapter is to present the petrophysical properties of the deformation bands and accompanying host rock determined from the samples collected in the field. As described in section 1.5.2, the collected samples from Middle Globigerina Limestone Member, were used to drill core plugs and to make polished thin sections (see Appendix II for sample locations). Further, permeability and porosity measurements of deformation bands and host rock were conducted by: i) laboratory measurements of core plugs by gas-transfer techniques and ii) image analysis of thin sections using ImageJ and MATLAB. The results will be presented below.

5.1 Porosity estimations

5.1.1   Core plug porosity

The bulk porosity was measured for six core plugs: three host rock samples and three samples containing deformation bands. Porosity measurements from helium porosimetry are shown in Table 5.1. The host rock provides an effective porosity ranging between 17-26%, whereas core plugs containing deformation bands show an effective porosity ranging between 18-23%. Thus, there is no significant change in porosity when deformation bands are present in the core. This is to be expected, since the technique records effective porosity of the entire sample, and since the deformation bands represent a very small volume compared to that of the entire sample. In order to analyze deformation band porosity, image analysis techniques are better suited, since these are capable of estimating the bulk porosity inside the deformation bands; image analyses of porosity are therefore presented in the next subsection.

Table 5.1: Bulk porosity obtained from core plugs.

Sample number	Sample length	Sample porosity (%)	Description
2	5.80	17.20	Host rock
11	5.80	25.78	Host rock
12	6.80	24.84	Host rock
16	6.30	22.71	Host rock containing deformation band
37A	7.00	19.76	Host rock containing deformation band
37B	7.00	18.32	Host rock containing deformation bands

5.1.2   Image analysis porosity

Image analyses using both ImageJ and MATLAB were performed on backscattered electron images (BSE) obtained from scanning electron microscope (SEM). The image processing methods provides an estimate of the porosity of deformation bands and host rock on a microscale, thus mapping out the variations in properties along and across deformation bands. Table 5.2, show the 2D porosity values from the BSE-SEM images at different locations within thin section 1B (Fig. 5.1). As illustrated in the table, the two image analysis methods provide similar porosity estimations. Host rock porosity varies from 19% to 32%, with average porosity of 24%. Contrastingly, the deformation bands reveal a lower porosity compared to that of the host rock, ranging between 9-12%, with average porosity of 10%.

Table 5.2: Porosity estimations from BSE-SEM images using ImageJ and MATLAB

| | BSE-SEM- derived porosity | | | |
| | Image J | | MATLAB | |
Location (1B)	DB Porosity (%)	HR Porosity (%)	DB Porosity (%)	HR Porosity (%)
D1	10.40	-	10.07	-
D2	11.90	-	11.30	-
D3	9.50	-	8.80	-
D4	9.00	-	8.6	-
H1	-	20.00	-	20.20
H2	-	20.00	-	20.20
H3	-	27.40	-	27.30
H4	-	32.00	-	30.70
H5	-	24.00	-	22.80
H6	-	19.90	-	18.90

Abbreviations: DB, deformation bands; HR, host rock.
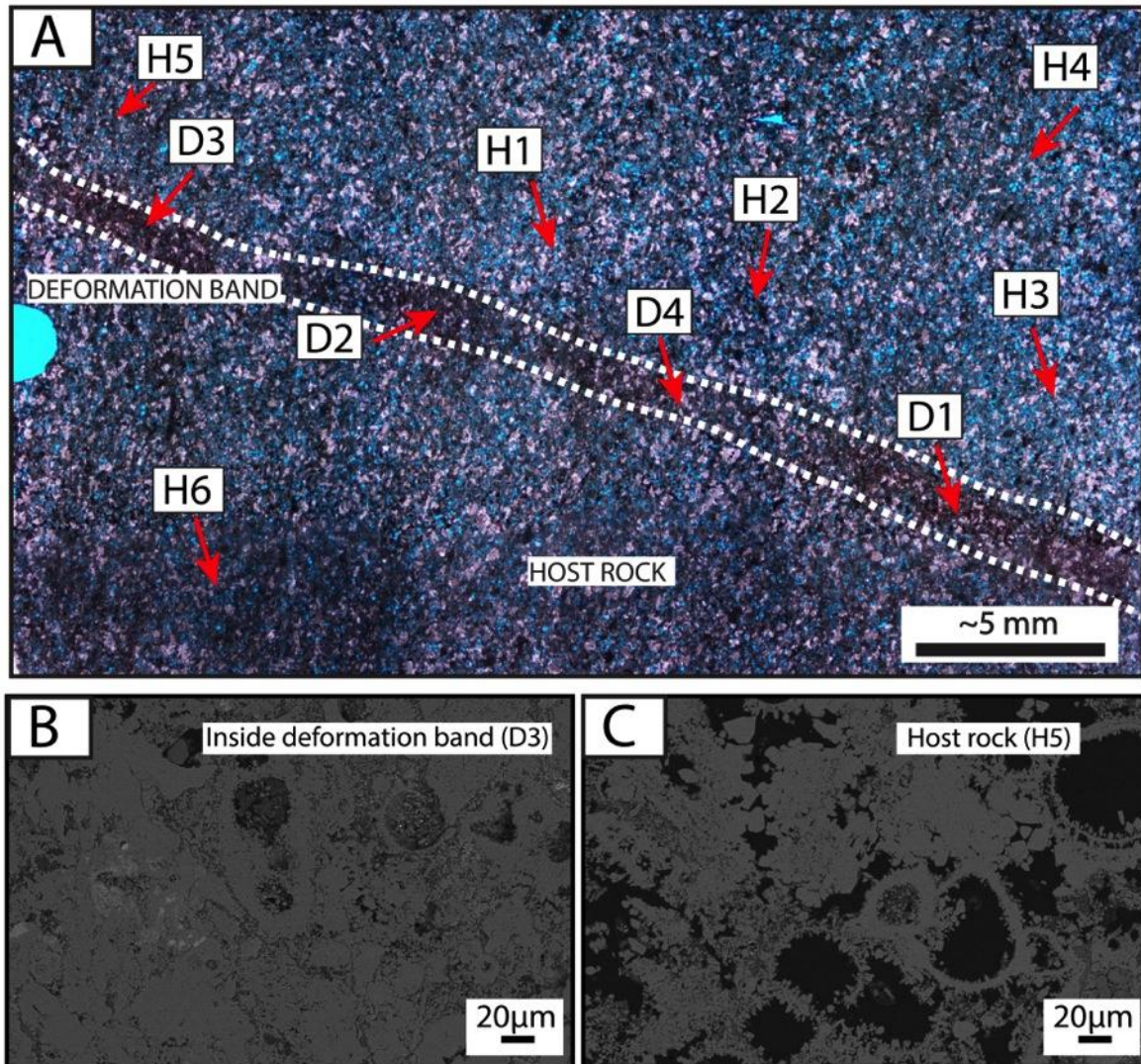
Figure 5.1: Photomicrographs from optical microscope and scanning electron microscope. A) Photomicrograph of thin section 1B, showing all the locations where BSE-SEM image analysis have been carried out for estimating porosity. White stippled line represents the boundary between host rock and deformation band. All locations termed "D" is within deformation band, while "H" are within the host rock. B) Backscattered electron images (BSE) from scanning electron microscope (SEM) with 1000x magnification, within the deformation bands and location "D3". Black color represents pore space, while grey color represents grains/cement. The porosity is here estimated to be 9.5%. C) BSE-SEM image from the host rock at location "H5" with 1000x magnification. The black color is pore space, while grey color is grains/cement. The porosity is here estimated to be 24%.

5.2 Permeability estimations

5.2.1 Core plug permeability

The Klinkenberg-corrected gas permeability of the core plugs is displayed in Table 5.3. In order to characterize the permeability reduction between deformation bands and adjacent host rock, three samples made up of both deformation bands and host rock were tested (Fig. 5.2). This gives the permeability for the whole samples as k_{total}. For a separate test, samples containing only host rock were measured as k_{hr}. This implicitly assumes that the host rock permeability does not vary significant within short distances from the bands. Further, assuming one-dimensional flow, the permeability of the deformation bands (k_{db}) can be calculated by:

$$k_{db} = \frac{l_{db}}{\frac{l_{total}}{k_{total}} - \frac{l_{hr}}{k_{hr}}}$$

Equation 5.1

Where l_{total}, l_{hr}, and l_{db} represents the total length of sample, length of the part containing host rock, and the thickness of the deformation band, respectively, as illustrated in Figure 5.2A (Deng et al. 2015).

The values of k_{hr} measured from the three host rock samples are different from each other (Table 5.3), thus l_{db}, l_{hr} and k_{hr} may have different values, and the variation of these parameters gives a range of the calculated permeability of the deformation band part in the plug sample. Thus, in the calculations of deformation band permeability, k_{total} and l_{total} remain constant, whereas the other parameters vary. The calculations are presented in Table 5.3

The average permeability in the undeformed host rock is 4.3 mD with a range from 2.42 to 7.40 mD. Thus, there is no significant variation in the permeability measurements obtained from the core plugs comprising only host rock. Nevertheless, for the samples containing deformation bands, there is a clear decrease in the sample permeability, ranging between 0.5-1.75 mD (Table 5.3). The calculated average deformation band permeability (eq. 5.1) ranges

from 0.038 to 0.093, revealing approximately 2 orders of magnitude permeability reduction relative to the host rock.
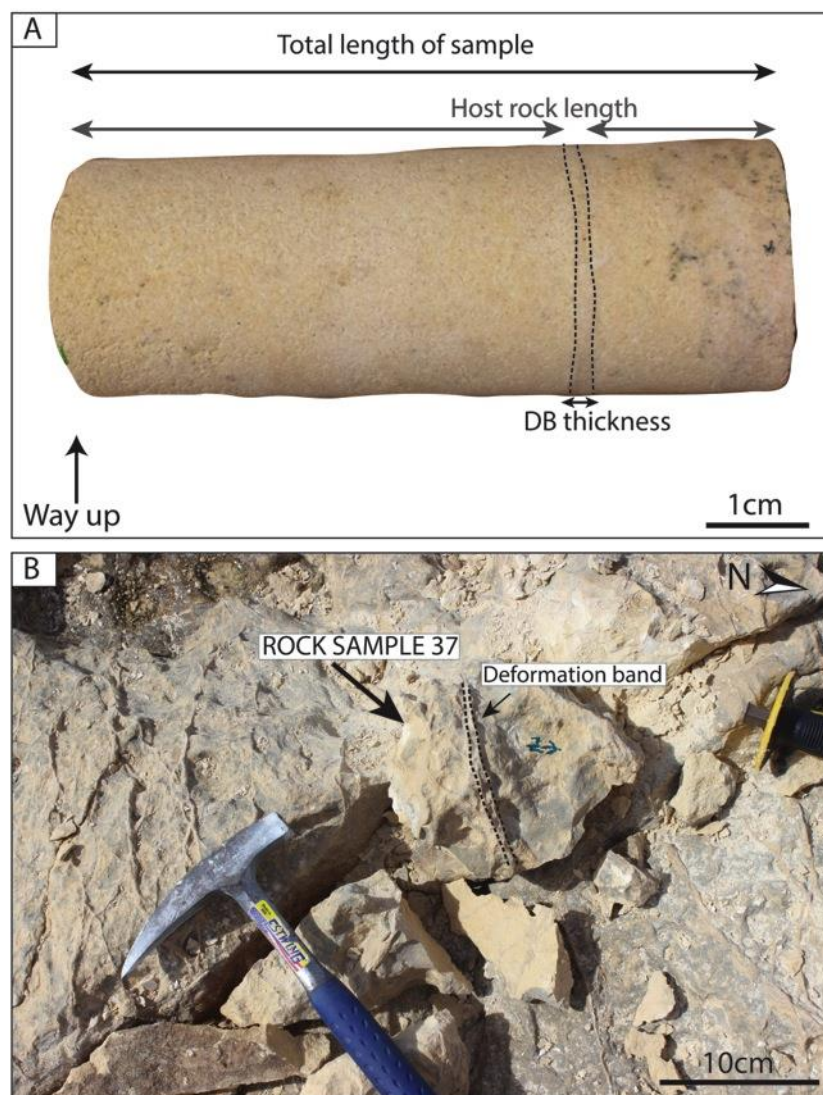
Figure 5.2: A) Representative core sample from bed-perpendicular deformation band. The core plug contains both deformation band and host rock. B) Field picture of rock sample 37. Deformation band is marked with black stippled line. The core plug was drilled out parallel with the bed, i.e. perpendicular to the deformation band.

Table 5.3: Measured permeability of each sample and calculate deformation band (DB) permeability.

Sample number	Sample length (cm)	Number of DB	Sample permeability (mD)	Thickness-range DB (cm)	Min. & Max. Permeability of DB (mD)	Average permeability of DB (mD)	Host rock permeability (mD)
2	5.80	0	3.12	-	-	-	3.12
11	5.80	0	2.42	-	-	-	2.42
12	6.80	0	7.40	-	-	-	7.40
16	6.30	1	1.02	0.1-0.2	0.020-0.062	0.038	-
37A	7.00	1	1.75	0.05-0.2	0.017-0.205	0.082	-
37B	7.00	4	0.53	0.5-1*	0.048-0.145	0.093	-

*Cumulative thickness, since there are 4 deformation bands present

5.2.2   Image analysis of permeability

A representative thin section containing both deformation band and host rock was selected for permeability estimations using image analysis of BSE-SEM images in MATLAB, calculating the permeability using a modified version of the Kozeny-Carman relation (e.g. Torabi & Fossen 2009). The locations for permeability estimations in the thin section are shown in Figure 5.1. Further, the permeability obtained from core plugs were compared to permeabilities from the image analysis. The estimated permeability values for host rock and deformation bands are illustrated in Table 5.4. The host rock yield permeabilities ranging from 2.86 to 146.66 mD, with average permeability of 35.31 mD. Compared to the permeability estimations from the core plugs, image analysis reveals more scatter, and is averagely one order of magnitude higher. Further, permeability estimation of the deformation band shows a range from 0.467 to 3.32 mD, with average permeability of 1.40 mD. Hence, compared to calculated deformation band permeability form core plugs, the image analysis yields somewhat higher permeabilities by 1-2 orders of magnitude. Nevertheless, the permeability calculations obtained from image analysis, reveal 1-2 magnitude orders of permeability reduction within the deformation bands relative to the host rock, similar to the permeability contrast attained from the core plugs.

Table 5.4: Image analysis permeabilites obtained from thin section 1B.

Thin section locality	Deformation band permeability (mD)	Host rock permeability
D1	1.10	-
D2	0.467	-
D3	0.832	-
D4	3.230	-
H1	-	2.86
H2	-	3.71
H3	-	33.78
H4	-	143.66
H5	-	21.33
H6	-	7.11

5.3 Porosity and permeability

Generally, for sandstones there is a simple relationship between porosity and permeability. In carbonate reservoirs, however, the porosity-permeability relationship is more complex (Lønøy 2006). As illustrated in porosity-permeability plot in Figure 5.3, the host rock reveals very high porosity, and low permeability, i.e. porosity above 15% and somewhat scattered permeabilities, which occasionally exceeds 20 mD. The deformation bands, however, has a porosity of 10%, and very low permeability which seldom exceed 1mD. Thus, compared to

the host rock, deformation bands reveal a decrease in porosity of approximately 50%, and permeability reductions of 1-2 orders of magnitude.
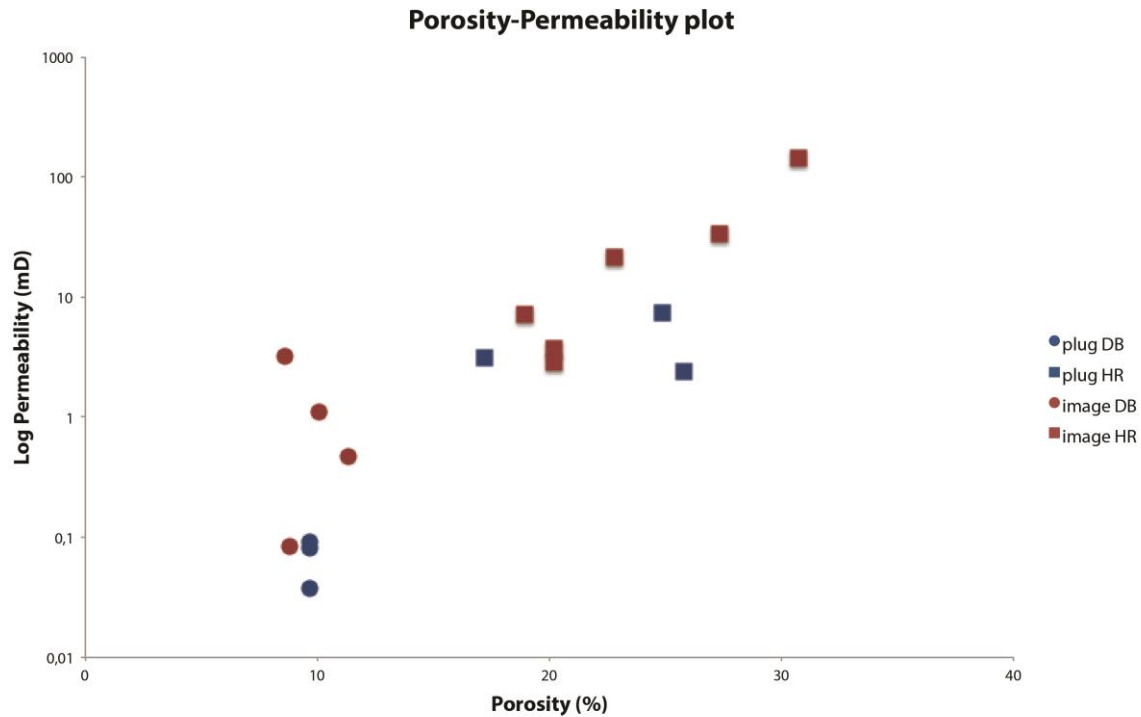
Figure 5.3: Porosity-permeability plot, showing the relationship between porosity and the logarithm of permeability for both host rock and deformation bands. Porosity and permeability estimations form core plugs are shown with blue squares and circles (plug HR- and DB), while petrophysical properties from image analysis (MATLAB) are shown with red squares and circles (Image HR- and DB). Note that since the plug estimations only reveal the bulk porosity of the core plugs containing deformation bands, average porosity from image analysis is used as porosity values of deformation bands. As shown from the porosity-permeability plot, the host rock (HR) has high porosity compared to permeability, while the deformation bands (DB) have lower porosity and even lower permeability compared to the host rock.

6. Reservoir modeling

This section describes the workflow from collecting field-data, through building an analogue geocellular reservoir model based on part of the studied outcrops, to undertaking flow simulation of that model. The purpose is to build a deterministic reservoir model based on a real outcrop case, in order to i) establish a method for (semi-)discrete representation of small scale heterogeneities in reservoir models, ii) to simulate and test the effect of small-scale structural heterogeneities (deformation bands) on fluid flow within a small area, and iii) test the effect of deformation bands in a low-permeable host rock scenario and a high-permeable host rock scenario.

6.1 Introduction

As previously described in section 2.2, computational limitations restrict the number of cells that can be represented in a full-field reservoir simulation model, and, consequently, the resolution of small-scale heterogeneities (e.g. Nordahl et al. 2005). However, if structural details were to be included explicitly, it would require a finer grid, resulting in substantial number of cells. In turn, this would be computationally expensive, and in extreme cases make the models unmanageable (Fachri et al. 2011, Fachri et al. 2013b). Thus, sub-centimeter scale deformation bands are too small to be discretely represented in conventional reservoir models, and they are often represented implicitly with upscaled permeabilities from numerical or analytical (approximate) procedures (e.g. Jourde et al. 2002, Rotevatn et al. 2009b). However, such approach does not fully resolve the orientation and distribution of the deformation bands. By building small-scale models, the deformation bands can be represented discretely in a finer grid, capturing the distribution and orientation of the observed structural sets. This can give insight to detailed flow behavior at a local scale. Further, results obtained from mini-flow models can be applied for upscaling permeability in full-field reservoir models with inexpensive computational costs (e.g. Fachri et al. 2013a, Fachri et al. 2013b).

In order to construct a small-scale reservoir model using semi-discrete representation of deformation bands, the spatial structural data collected in the field from the 1m x 1m square presented in section 4.2.1 (see Fig. 4.5D) was used. The stratigraphic unit of interest in the present study is the 4.6 m thick Unit 1M within the Middle Globigerina Limestone Member (see section 4.1.3). The resolution of the structures recorded in the square is approximately 3 millimeters, equivalent to the average thickness of the deformation bands mapped in the field.

6.2 Grid modeling and fluid flow simulation design

A reservoir model based on structural data collected in the field was built by the use of the reservoir-modeling suite Roxar RMS 2012 (see section 1.5.3 for general work flow). The procedure for constructing reservoir models from outcrop data is illustrated in Figure 6.1. All steps regarding the model building, i.e. surface modeling, creating a grid, property modeling and flow simulation will be described in detail in this section.
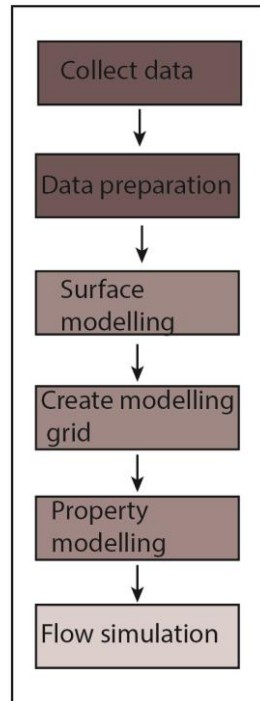
Figure 6.1: Illustration of the main steps involved building the deterministic model based on real outcrop data. Collection of data was done during fieldwork and the methodology is described in section 1.5.1, and the data is further presented in chapter 4. The main steps in building the geocellular model will be examined in this section and includes i) surface modeling (Section 6.2.1), ii) creation of the modeling grid (Section 6.2.1), iii) property modeling (Section 6.2.3), and iv) flow simulation (Section 6.2.5).

6.2.1   Model framework and grid

Due to technical limitations of RMS, it is not possible to flow simulate a modeling grid with a total size of 1 m x 1 m. Therefore, an inflated model was generated with a 1:1000 enlargement, thus keeping the ratios and relationships constant between the observed structural sets in outcrop and the model. Additionally, the frequency and pattern of the deformation bands are preserved.

The surface model represents the framework for the geocellular model, providing the boundaries used to constrain the grid. The project boundary was set to 1000 m x 1000 m x 10

m. Initially two horizontal surfaces were generated, defining the top and the base of the reservoir model, with the base situated 10 meters below the top. Once the surface framework was established, a zone bounded by these two surfaces was created, and a geocellular grid was generated. Grids are built between the surfaces in order to present properties, i.e. petrophysical properties and facies. The resulting modeling grid has a total grid size of 1000 m x 1000 m x 10 m, corresponding to a grid cell configuration of 100 x 100 x 1, bringing the total number of cells to 10 000. Thus, the average cell size of the grid is 10 x 10 x 10 meters. The grids are designed to specifically follow the key geological heterogeneities (i.e. deformation bands) due to their potential control on fluid flow.

6.2.2   Representation of deformation bands in the reservoir model

As previously mentioned in section 6.1, small-scale heterogeneities are challenging to represent in full-field reservoir models. Thus, the main technical challenge for the reservoir modeling in the present study is to represent the millimeter scale deformation bands in the model, as the bands are too small and numerous to be resolvable in the modeling grid. Therefore, the deformation bands were represented in the model with a 1:1000 enlargement, resulting in a single deformation band being c. 3 meters thick. Using this inflated approach allowed us to undertake a semi-discrete representation of the deformation bands in the model.

In order to discretize the deformation bands in the geocellular model, the following approach was used. Firstly, the detailed 1x1 deformation band map illustrated in Figure 6.2A was imported into RMS as a JPG file, and inflated to fit the model boundaries of 1000 m x 1000 m in the x- and y-direction. Secondly, 3D trend parameters were generated for the geocellular grid, allowing for discretization of the deformation bands. By using the deformation band map, the deformation bands were digitized into the grid by populating each cell with a trend parameter assigned values from 0 to 4, based on the frequency of deformation bands within that particular cell (Fig. 6.2B): i) undeformed host rock (trend parameter= 0) ii) one deformation band present (trend parameter= 1), iii) two deformation bands present (trend parameter= 2), vi) three deformation bands (trend parameter= 3) and iv) four deformation bands present (maximum value; trend parameter=4). The model comprises only one cell in the vertical direction (z-axis), and thus all the deformation bands were assumed to be vertical and continuous through the reservoir model.

With the 3D trend parameter being established, the model can be further assigned with petrophysical properties.
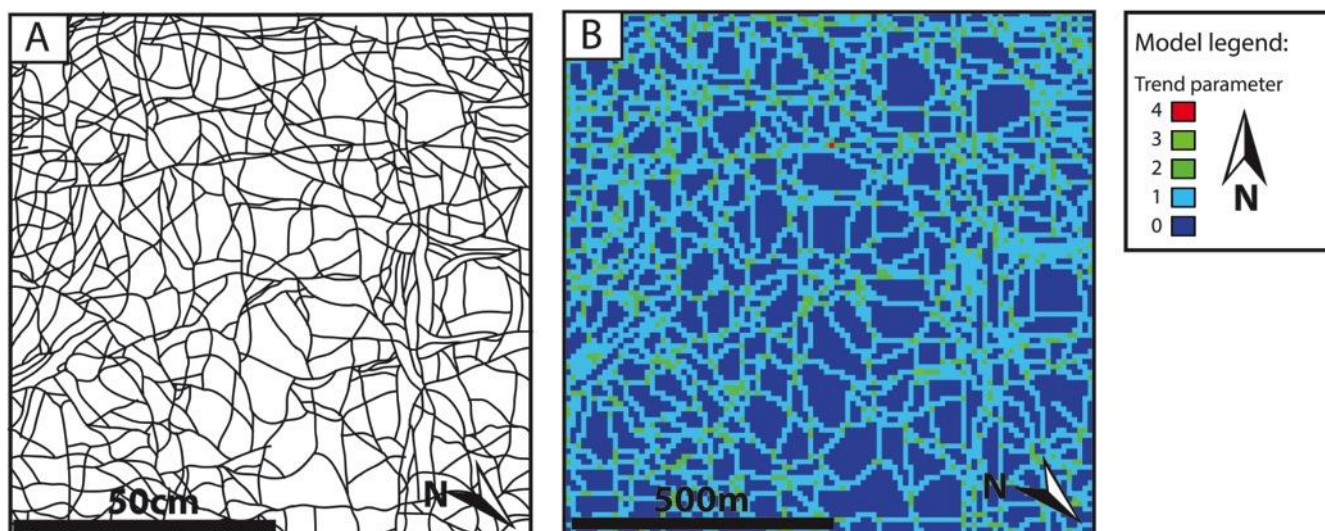
Figure 6.2: A) Deformation band map representing the band pattern within 1 m x 1 m square in the Middle Globigerina Limestone Member. This map was imported into RMS, in order to digitalize the deformation bands in the model. Field picture of the 1 m x 1 m square is shown in **Figure 4.5**. B) Based on the deformation band map, the bands were digitized into the geocellular model as 3D trend parameters. The cells comprising the model was populated with trend parameters assigned values from 0 to 4, based on the frequency of deformation bands within that particular cell: i) undeformed host rock (trend parameter=0), ii) one deformation band present (trend parameter=1), iii) two deformation band present (trend parameter= 2), vi) three deformation bands present (trend parameter= 3) and iv) four deformation bands present (trend parameter= 4). Note that the geocellular model is inflated, to a total grid size of 1000 m x 1000 m. Additionally, the geographically north is not the same as north in the model.

6.2.3   Modeling petrophysical properties

The final step in the generation of the geological- reservoir model involves the assignment of petrophysical properties of the grid cells. The petrophysical properties and the calculation of grid cell permeabilities are presented below. Using the parameter calculator, the deformation bands and adjacent host rock have been deterministically assigned permeability and porosity values.

Petrophysical properties

The reservoir modeling in this study uses porosity and permeability values presented in Rath et al. (2011) and Antonellini et al. (2014), as these authors addresses the porosity and permeability contrast between deformation bands and host rock in porous carbonate grainstones. Note that the permeabilities determined in this thesis (Chapter 5) falls within the values taken from these two papers, but that the published values were used to broaden the

range of band permeabilities tested.

By the use of pressure decay probe permeametry, Rath et al. (2011) found a permeability difference of at least 2.5 orders of magnitude between deformation bands (0.2-10mD) and the nondeformed host rock (60-7976mD). Using the same method, Antonellini et al. (2014) reported a permeability reduction of 1 order of magnitude, from the host rock (26.5-265.3mD) to the deformation bands (1.3-21.7mD). Nevertheless, the reported porosity of the deformation bands and the adjacent host rock in the two studies is similar. From helium porosimetry, Rath et al. (2011) found a deformation band porosity of 2-5%, and 22-35% porosity of the accompanying host rock. Antonellini et al. (2014) reported 2-5% deformation band porosity and 17-27% host rock porosity from image analysis of thin sections (2D porosity).

Permeability and porosity values used in this study are within the range of the reported petrophysical properties of the aforementioned studies. The porosity is kept constant throughout the model volume: 22% porosity for host rock and 5% porosity for the deformation bands. Host rock permeability is set to 150 mD and 1000 mD, with different values of deformation band permeability: 100 mD, 10 mD and 1mD.

The current study focuses on how permeability changes related to deformation bands affect fluid flow. Hence, effects of porosity reduction and capillary effects are beyond the scope of the study and are thus not considered here. Since the deformation bands are vertical, variations in vertical permeabilities can be ignored as there is no way for fluids to flow around the permeability barriers that are vertically continuous through the reservoir model.

Computing grid cell permeabilities in the model
The deformation bands in the inflated model have a thickness of approximately 3 meters, and even with high grid resolution such as in this case (10 m x 10 m x 10 m), the deformation bands are too small to occupy the entire cell width. The cumulative thickness of deformation bands in each cell is given by the 3D trend parameter that shows the number of deformation bands in each cell. Thus, in order to account for a single deformation band only occupying 30% of the cell width, the established 3D trend parameter was used to calculate the effective permeability of each cell, by modifying the initial deformation band permeabilities of 100 mD, 10 mD and 1 mD. Further, the porosity and modified effective cell permeabilities (x- and

y-directions) were assigned to the individual cell trend parameter using a simple IF-THEN algorithm in the parameter calculator.

In general, if the flow is parallel to the main structures, an arithmetic mean is used to estimate the effective permeability, while if the flow is perpendicular to structures, the harmonic mean is the best estimate of effective permeability (Manzocchi et al. 1998). However, given the varying orientation of deformation bands in the present model (Fig. 6.3A), a simplification was done by assuming that the permeability in the x- and y-direction (perm_x and perm_y) is equal and can best be estimated using the harmonic mean. As the deformation bands with different orientations frequently crosscuts and intersects to create blind alleys or minitraps, the arithmetic average would underestimate the permeability. Encountering such minitraps, the fluids are forced to cross one or more deformation bands (Fig. 6.3B). Thus, as a minimum approach the minitraps are assumed to represent a barrier equivalent to a single deformation band, and both perm_x and perm_y will be closer to the harmonic average than the arithmetic average permeability (Fig. 6.3C).

The effective permeability (K_{eff}) was calculated using the harmonic average for one-dimensional flow through an anisotropic medium given by Cardwell and Parsons (1945):

$$k_{eff} = \frac{L}{\frac{l_{hr}}{k_{hr}} + \frac{l_{db}}{k_{db}}}$$
                                                                                        Equation 6.1

Here, L is the total length of flow path (10 meters for each cell), k_{hr} and k_{db} are the bulk permeability of the host rock and deformation bands respectively and l_{hr} and l_{db} are the total accumulated width of the host rock and deformations bands respectively. The effective permeability calculations are shown in Table 6.1.
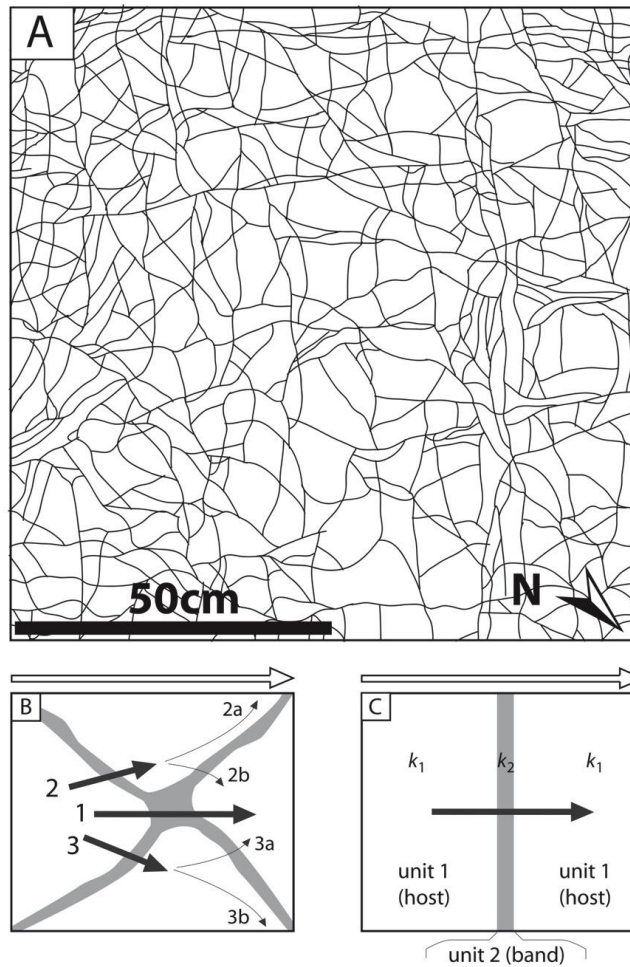
Figure 6.3: A) Deformation band map representing a 1 x 1 meter area in the field (Fig. 4.5). The deformation bands are closely spaced and reveal variable orientations, resulting in a highly connective and anastomosing pattern. Note that the deformation bands with different orientations crosscuts and intersects. B) Illustration of an approximation of possible flow path from the left to the right in a grid cell where two deformation bands crosscut and forms a minitrap. Flow paths 2a and 3b represents the least hindrance to flow. C) The encounter of a minitrap represents a barrier at least equivalent of one individual deformation band. The harmonic average is used to calculate the effective permeability for the situation. Note that B) and C) are from Rotevatn et al. (2007).

Table 6.1: Calculated effective permeability, using harmonic mean eq., for each trend parameter in the different models.

Model	Para-meter	Host rock		Single deformation bands				Total	
		Lhr (m)	Khr (mD)	Average DB thickness (m)	Number of DB to cross	Ldb (m)	Kdb (mD)	L tot (m)	K(eff) (mD)
LL_REF	0	10	150	3.3	0	3.3	150	10	150
LL_1ORD	1	6.7	150	3.3	1	3.3	10	10	27
LL_1ORD	2	3.4	150	3.3	2	6.6	10	10	15
LL_1ORD	3 & 4	0.1	150	3.3	3	9.9	10	10	10
HH_REF	0	10	1000	3.3	0	3.3	1000	10	1000
HH_1ORD	1	6.7	1000	3.3	1	3.3	100	10	252
HH_1ORD	2	3.4	1000	3.3	2	6.6	100	10	144
HH_1ORD	3 & 4	0.1	1000	3.3	3	9.9	100	10	101
HH_2ORD	1	6.7	1000	3.3	1	3.3	10	10	30
HH_2ORD	2	3.4	1000	3.3	2	6.6	10	10	15
HH_2ORD	3 & 4	0.1	1000	3.3	3	9.9	10	10	10
HH_3ORD	1	6.7	1000	3.3	1	3.3	1	10	3
HH_3ORD	2	3.4	1000	3.3	2	6.6	1	10	2
HH_3ORD	3 & 4	0.1	1000	3.3	3	9.9	1	10	1

Abbreviations: REF= Reference model (deformation bands absent), 1ORD=1 order of magnitude permeability difference between host rock and deformation bands, 2ORD= 2 orders of magnitude difference, etc.

6.2.4   Experimental design

A total of six deterministic models were generated with deformation band frequency, distribution and orientation based on field observations, and petrophysical properties of deformation bands and host rock based on measurements presented in Rath et al. (2011) and Antonellini et al. (2014). The six deterministic models are based on principally two cases, with different initial host rock permeability, and different realizations within each case where the main variable modulated was the deformation band permeability. Thus, a high permeable host rock case and a low permeable host rock case were tested, and will be further addressed as HH-case and LL-case respectively (Fig. 6.4). As the main aim was to investigate the effect of deformation bands on fluid flow, measures were taken to isolate these effects. Hence, the model comprises only one zone (Unit 1M) where lithological contrasts were omitted and the reservoir sedimentology was modeled as homogenous. The porosity of the host rock and deformation bands in both cases is kept constant throughout the model volume: 22% host rock porosity and 5% deformation band porosity.

The HH-case is based on permeability measurements presented in Rath et al. (2011), described in section 6.2.3. The initial host rock permeability in this case is kept constant at 1000mD, and the permeability contrast between the host rock and deformation bands in the different realizations ranges from 1-3 orders of magnitude, i.e. 100mD, 10mD and 1mD deformation band permeability (HH_1ORD, HH_2ORD and HH_3ORD; Fig. 6.4). The LL-case however is based on permeability measurements presented in Antonellini et al. (2014), described in section 6.2.3. The initial host rock in this case is 150mD, and kept constant throughout the model volume. Here, the permeability contrast between host rock and deformation band is 1 order of magnitude, equivalent to a deformation band permeability of 10mD (LL_1ORD; Fig. 6.4). Additionally, undeformed grids with identical dimensions and gridcell configuration were made for both cases. This permits all the model cases to be flow simulated both with and without deformation bands, in order to isolate the effects of deformation bands on synthetic reservoir behavior (HH_REF and LL_REF; Fig. 6.4).

As mentioned in section 6.2.3, the deformation bands in the model do not occupy the entire cell width. Thus, the cell permeability was modified by calculating the effective permeability of each cell using the harmonic mean equation. These modified cell permeabilities, K(eff) in Table 6.1, were used as input values of the cells comprising the model.
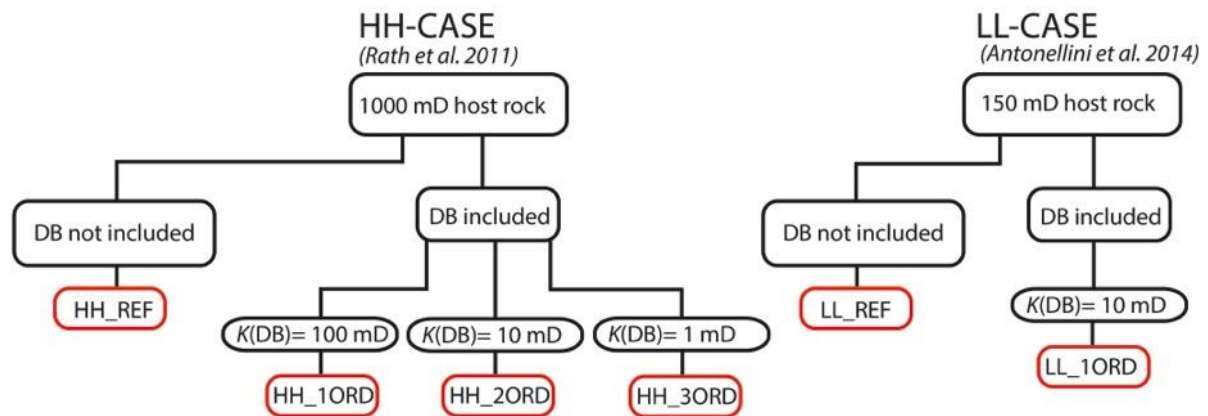
Figure 6.4: Hierarchical overview of the models built and simulated in this study. One high-permeable host rock model was generated (HH-case) based on permeability measurements of deformation bands and host rock presented in Rath et al. (2011). Three realizations were simulated for this model with varying permeability contrast between deformation bands and host rock (HH_1ORD, HH_2ORD and HH_3ORD). Furthermore, one low-permeable host rock model was created (LL-case) based on deformation band and host rock permeability values presented in Antonellini et al. (2014). For this model, one realization was flow simulated, testing the effect of the presence of low permeable deformation bands. Additionally, undeformed grids with identical dimensions and gridcell configuration were made for both cases (HH_REF and LL_REF). Abbreviations: DB= deformation bands, K(DB)= permeability deformation bands, REF= reference case with no deformation bands, 1ORD= 1 order of magnitude permeability reduction within deformation bands, relative to host rock, 2= 2 orders of magnitude permeability reduction and 3ORD= 3 orders of magnitude permeability reduction.

6.2.5   Flow simulation

All six models were flow simulated using RMS finite difference, black oil simulator. The flow simulations were based on two vertical water-injection wells and two vertical production wells placed on opposite sides of the model, 800 meters apart. The injection wells were positioned in the western part of the model, and the production wells in the eastern part. As the aim was to investigate the effect of deformation bands on fluid flow, the main variable tested were host rock and deformation band permeability. Thus, other dynamic variables are kept constant between the model runs.

The aim was to simulate injection in the lower part of the model and evaluate the flow across grid for a minimum of 35 years, or until water break-through occurred in the producing wells. Some simplifications were necessary: first, extreme injection rates of 100000 Sm^3 of water per day and production rates of 90000 Sm^3 oil per day were used; and secondly: the reservoir was assumed to be oil filled (i.e. oil-water contact below the geocellular model). The dynamic properties used to condition the models are presented in Table 6.2. The key parameters used

to analyze the model sensitivity were water-cut, oil saturation and time to water break-through.

Table 6.2: Flow simulation dynamic properties.

Length of run	Until water break-through in production well	
Other run constraints	Minimum 35 years	
Report step		Every month
Rock compressibility		0.0000435 1/bar
Rock reference pressure		275.79 bar
Spec. gravity oil		0.8
Gas/oil ratio		142.486 Sm^3 Sm^{-3}
Corey exponents	Water	4
	Oil	3
Saturation end points	S_{ORW}	0.2
	S_{WRC}	0.2
Rel. perm. End points	k_{romax}	1
	k_{rw}	0.4
Top of model		0 m
Oil-water contact (OWC)		11 m
OWC capillary pressure		0 bar
Reference depth		10 m
Reference pressure		50 bar
Wells	Injectors	2
	Producers	2
Flow rate	Injectors	100000 Sm^3 per day
	Producers	90000 Sm^3 per day
Bottom-hole pressure	Injectors	70 bar
	Producers	50 bar

6.3 Results flow simulation

One of the purposes of this study was to investigate the effect of deformation bands with variable orders of permeability reduction relative to host rock on fluid flow in a i) low-permeable host rock scenario (LL-case) and ii) a high-permeable host rock scenario (HH-case). Analyzed fluid flow aspects include flow characteristics in terms of variation in shape and speed of waterfronts. In addition, reservoir performance is analyzed using time to water break-through and oil saturation. The results are shown graphically in Figure 6.5 through Figure 6.10, and in Table 6.3, and will be described in the following subsections.

6.3.1   Low-permeable host-rock cases (LL-cases)

For the low-permeable host rock cases, one reference scenario without bands (LL_REF), and one scenario with low band-to-host permeability contrast (LL_1ORD), were run (see Fig. 6.4 for an overview of the different cases descriptions). Fluid flow characteristics in the LL-case with low permeability contrast between host rock and deformation bands (LL_1ORD; *c*. 1

order of magnitude) were compared with the reference case with no deformation bands present (LL_REF), at different time steps as illustrated in Figure 6.5.

In the LL_REF case, the water from the injection wells displaces the oil with smooth and radial fluid fronts. After 5 years of simulation, the water has almost moved half way across the grid, however, still as separate fluid fronts. The two fluid fronts are separate throughout the first 10 years of the simulation, and link up after approximately 15 years, with a small portion of residual oil between the contacts. After 5721 days (16 years; Table 6.3 and Fig. 6.6), the injected water reaches the two production wells in the eastern part of the model simultaneously. Further, after 20 years of simulation, there is still some oil left in the model, as the water has not yet travelled across the whole grid (Fig. 6.5).

Comparatively, in the LL_1ORD case where deformation bands are present, the waterfronts get more irregular (Fig. 6.7) and the water migrates slower across the grid (Fig. 6.5). After 5 years of simulation, the water has migrated approximately 200 meters away from the injection wells, and displaces the water with uneven fluid fronts. The water reaches half way across the grid after 15 years, and the fluid fronts starts to link up after 20 years, however, still with a noteworthy quantity of residual oil between the water front contacts. The injected water has not yet reached the production wells 20 years into the simulation; hence there is a larger portion of oil left in the LL_1ORD case, compared to the LL_REF case after 20 years (t(20); Fig 6.5). Water break-through occurs after 9435 days (26 years) in the southeastern production well, whereas the water reaches the production well in the northeastern part after 11 200 days (31 years; Table 6.3 and Fig. 6.6). Thus, with the presence of deformation bands in the model the water break-through is delayed by 10 and 15 years in the SE and NE production wells, respectively (compare LL_REF with LL_1ORD; Table 6.3 and Fig. 6.6).
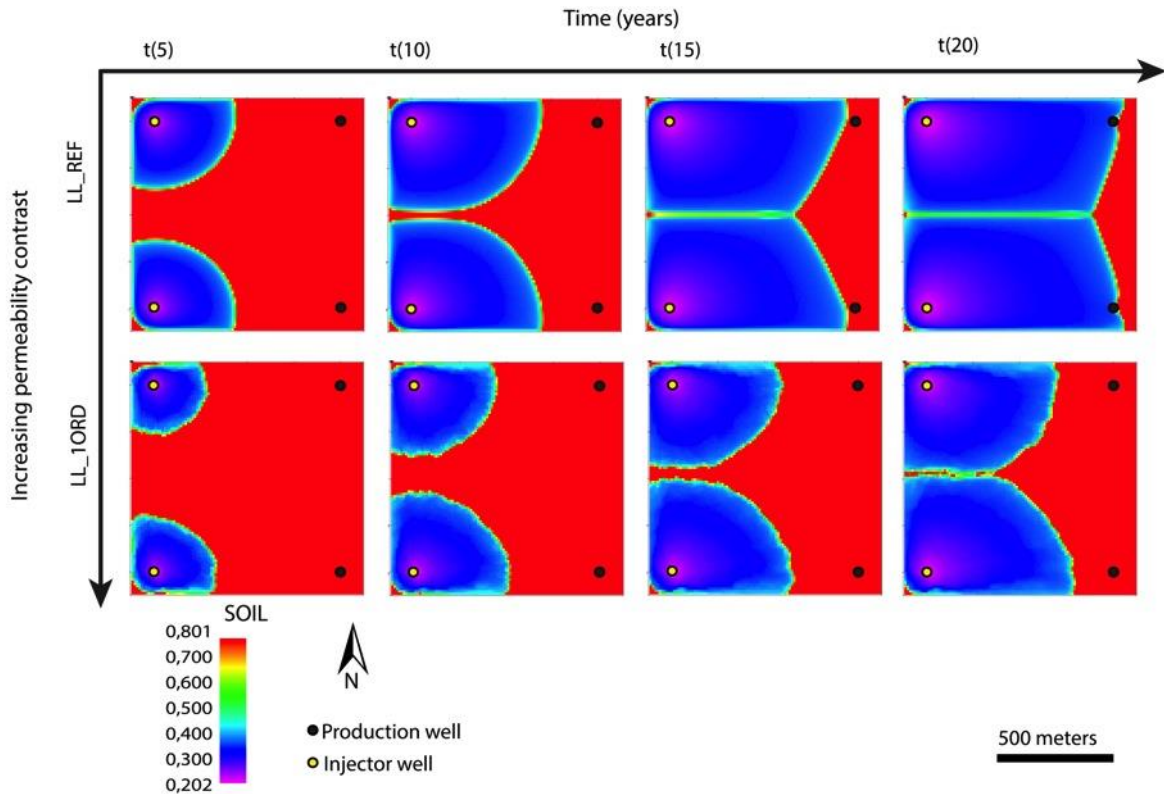
Figure 6.5: Oil saturation at different time steps of the flow simulation in the low- permeable host rock cases: one reference scenario without bands (LL_REF) and one scenario with low band-to-host permeability contrast (LL_1ORD). The host rock permeability is kept constant at 150 mD throughout the models, whereas the deformation band in LL_1ORD case is *c.* one order of magnitude lower than host rock. As illustrated by the figure, in the LL_REF case, the waterfront displaces the oil with smooth and radial fluid fronts, where the fluid fronts link up after 15 years of simulation. The water migrates relatively fast, and water break-through occurs after 5721 days (16 years) in both production wells. Note that there is still some residual oil left in the model after 20 years of simulation, as the water has not yet travelled across the whole grid. In the LL_1ORD case, however, the waterfronts get more irregular and migrate slower across the grid. Due to the slower water propagation, there is more oil in the model at all time steps compared to LL_REF. The waterfronts start to link up after 20 years, and have still not reached the production wells in the eastern part at this time step. Thus there is a larger amount of oil trapped between the waterfront and more oil left in the eastern part of the model in LL_1ORD compared to LL_REF at t(20).
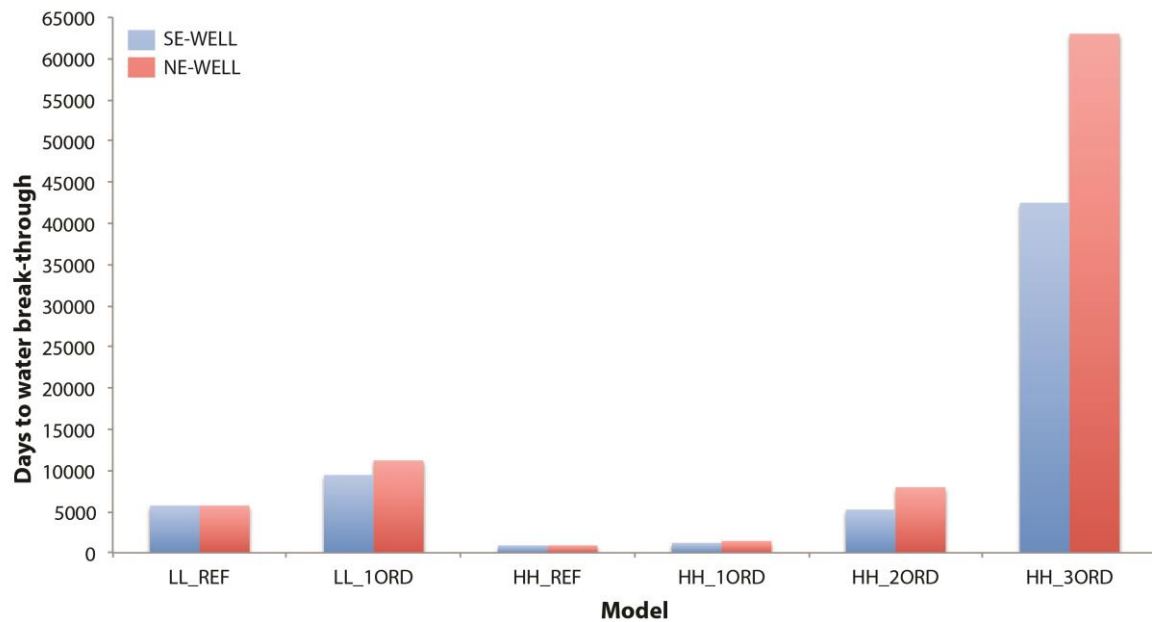
Figure 6.6: Histogram showing days to water break-through (y-axis) in the different models (x-axis). The production wells in the reference cases (LL_REF and HH_REF) generally reaches water break-through faster compared to when deformation bands are present in the models. Additionally, the water reaches the production well situated in the southeastern corner of the model faster than the northeastern situated production well (except in LL_REF and HH_REF cases, where water break-through occurs simultaneously). When comparing the LL-cases and the HH_cases the water generally migrates faster in the latter, and thus reaches water break-through faster in the production wells.

Table 6.3: Time to water break through (WBT) for the production wells in all the model cases.

Model	Days to WBT		Years to WBT	
	SE-well	NE-well	SE-well	NE-well
LL_REF	5721	5721	16	16
LL_1ORD	9435	11200	26	31
HH_REF	883	883	2.5	2.5
HH_1ORD	1187	1430	3	4
HH_2ORD	5236	7944	14	22
HH_3ORD	42490	63005	116	173

Note that years are rounded up/down to closest half year.
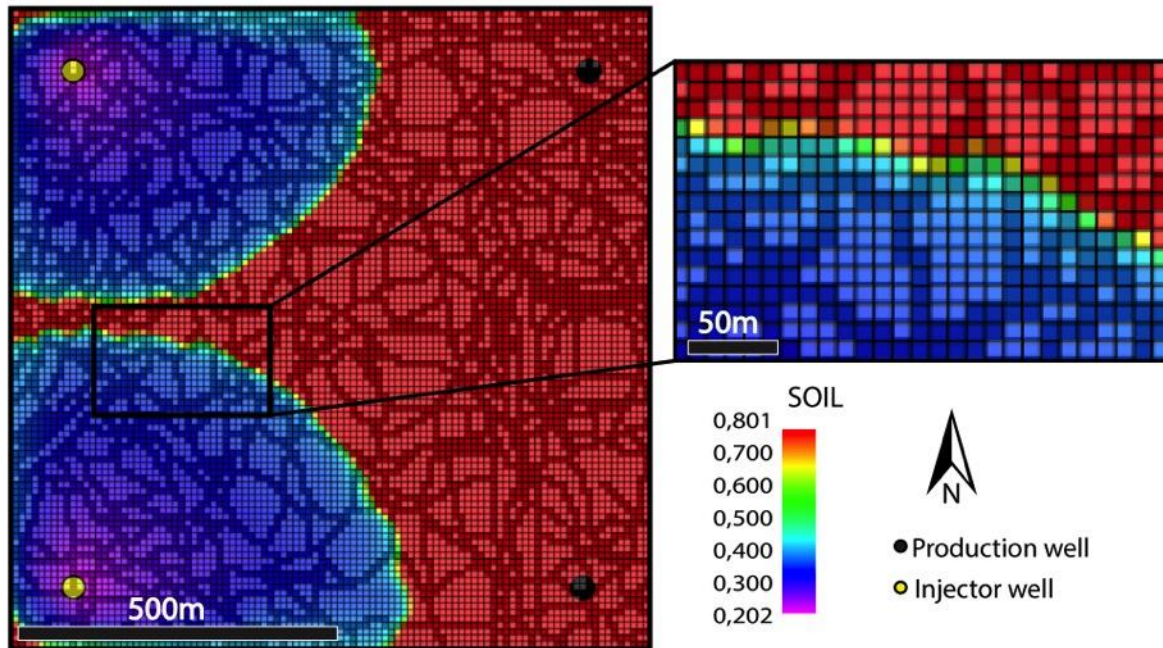
Figure 6.7: Illustration of how the fluid front is disrupted by the presence of deformation bands in LL_1ORD case after 15 years of simulation (t(15); Fig. 6.5). The deformation bands forms a complex orientation pattern, and are marked with black lines in the model.

6.3.2   High-permeable host-rock cases (HH-cases)

For the high-permeable host rock cases, one reference scenario without bands (HH_REF), and three scenarios with variable band-to-host permeability contrast (HH_1ORD, HH_2ORD and HH_3ORD), were flow simulated (see Fig. 6.4 for an overview of the different cases descriptions). Fluid flow characteristics in the HH-cases with varying orders of magnitude permeability contrast between host rock and deformation bands (10^1, HH_1ORD; 10^2, HH_2ORD; 10^3, HH_3ORD) were compared with each other, and the reference case, at different time steps as illustrated in Figure 6.8.

In the reference case (HH_REF), the waterfront is tabular due to early link-up of the two waterfronts from the injection wells (Fig. 6.8). The water migrates rather fast, and within 5 years of simulation time, the water has almost travelled across the entire grid. At this time step, however, there is still some residual oil in the eastern most part of the model and some smaller amounts between the waterfronts. Within 10 years of simulation time, the water has displaced most of the oil, and the model contains mostly water. Coinciding water break-through is apparent in the two production wells after only 883 days (2.5 years), as shown in Table 6.3 and Figure 6.6.

A similar flow pattern is observed in the HH_1ORD case, with just a slightly more irregular front and slightly slower water migration across the grid (Fig. 6.8). After 5 years of simulation, the waterfronts are linked-up, still with some amount of residual oil between the fluid front contacts. When comparing HH_REF and HH_1ORD at this time step, there is more oil in the eastern part of the model, due to the migration across the grid is somewhat slower in the HH_1ORD case. Additionally, in the HH_REF case the water front contact is observable as a straight line throughout the model, whereas in the HH_1ORD case the fluid front contact is curved towards SE. After 20 years of simulation in the HH_1ORD case, the model is mostly water saturated. The production wells in the southeast and northeast reach water break-through after 1187 (3 years) and 1430 (4 years), respectively (Table 6.3 and Fig. 6.6). Thus, compared to the HH_REF case the water break-through is delayed by 0.5 and 1.5 years (in the SE and NE wells, respectively), when deformation bands are present with one order of magnitude permeability reduction relative to host rock (compare HH_1ORD and HH_REF in Table 6.3 and Fig. 6.6).

In the HH_2ORD case, waterfronts are increasingly uneven with higher degree of tortuosity (Fig. 6.8). Five years into the simulation time, the waterfronts from the injection wells are still separate, and the oil saturation area is significantly larger compared to HH_REF and HH_1ORD cases. After 10 years, the water has migrated half way across the grid, however, with somewhat faster migration of the water from the southwestern injection well. The fluid fronts link up after 15 years of simulation, but with a zone of residual oil between the waterfront contacts. After 20 years of simulation, there is still a relatively large amount of oil left in the model in the eastern part of the model, compared to HH_REF and HH_1ORD cases (Fig. 6.8). In the HH_2ORD case, water break-through appears after 5236 days (14 years) in the production well situated in the southeast, and 7944 days (22 years) in the northeastern production well (Table 6.3 and Fig. 6.6). Thus, when the deformation bands have 2 orders of magnitude lower permeability compared to the host rock, water break-through is delayed by 11.5 and 19.5 years, compared to when deformation bands are absent (HH_REF).

However, the largest difference is observed in the HH_3ORD case, where the waterfronts are almost circular and much less widespread than the other models (Fig. 6.8). After 5 years of simulation, the water has migrated only *c*. 100 meters away from the injection wells, displacing the oil with uneven sub-circular waterfronts. Further into the simulation, the waterfronts are getting even more disrupted and irregular, with increasing degree of tortuosity

(Fig. 6.9). At all time steps, there are larger volumes of residual oil left in the HH_3ORD case, compared to the other models (HH_REF, HH_1ORD and HH_2ORD). This is due to the extremely slow migration of the water across the grid. Additionally, the westernmost corners in the HH_3ORD case comprise unswept oil pockets. After 20 years, the water has not even extended to the central part of the grid, and there are large amounts of oil present in the model. It takes 42 490 days (116 years) for the water to reach the southeastern production well, and 63 005 days (173 years) to the northwestern well (Table 6.3 and Fig. 6.6). Accordingly, when deformation bands have 3 orders of magnitude permeability difference compared to host rock, the water break-through in the production wells is delayed by 113.5 and 170.5 years, compared to when no deformation bands are present in the model (HH_REF).
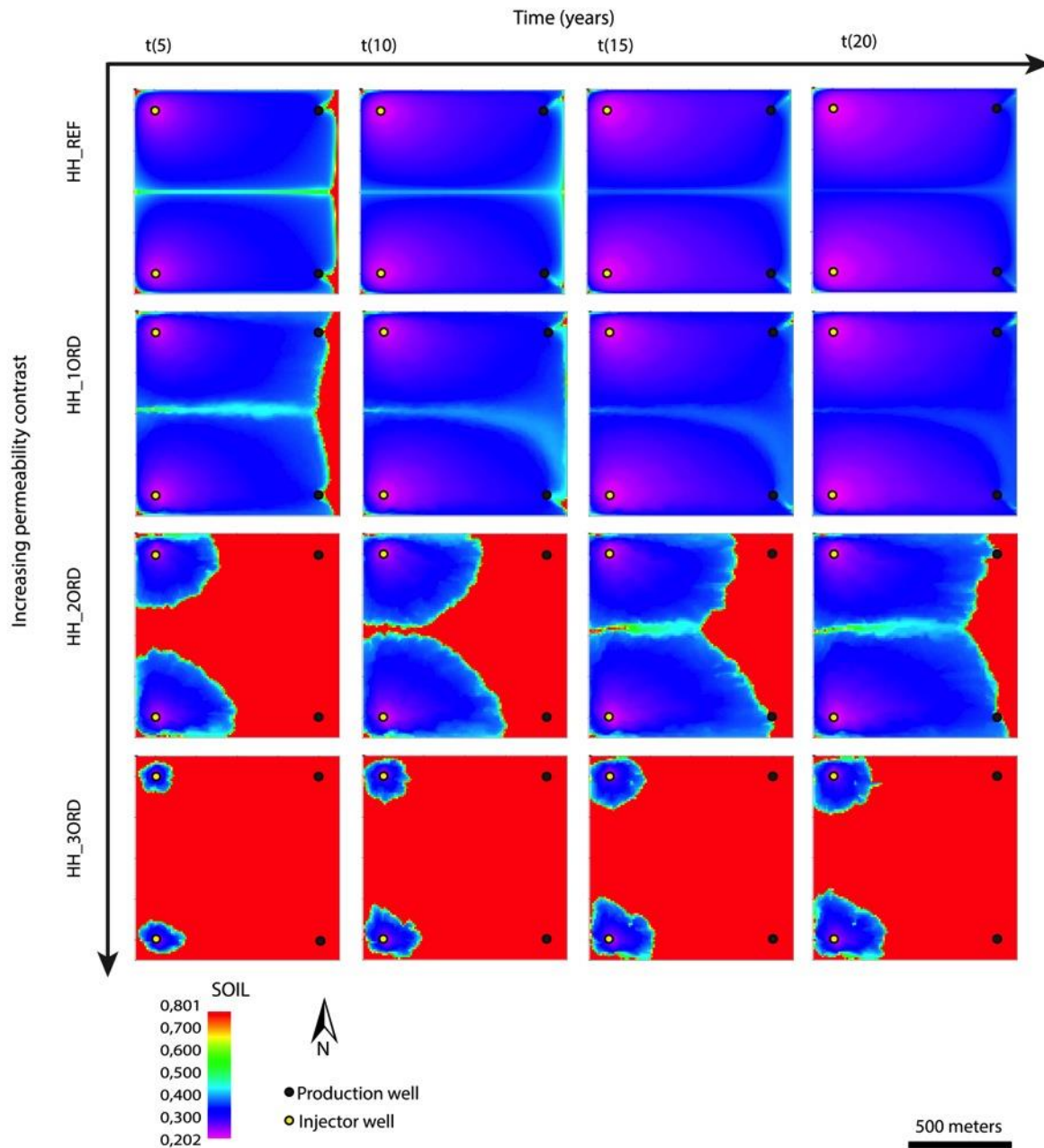
Figure 6.8: Oil saturation at different time steps of the flow simulation in the high-permeable host rock cases: one reference scenario without deformation bands (HH_REF) and three cases with varying orders of magnitude permeability contrast between host rock and deformation bands (10^1, HH_1ORD; 10^2, HH_2ORD; 10^3, HH_3ORD). As illustrated by the figure, in the HH_REF and HH_1ORD cases, the water displaces the oil in the model by a tabular waterfront due to early link-up of the two waterfronts from the injection wells. The water migrates rather fast, and within 5 years of simulation (t(5)), the water has almost travelled across the entire grid for both cases. As the water migrates slightly slower in the HH_1ORD case, there is more oil present in the eastern part of the model at t(5). Additionally, at this time step, there is a larger zone of residual trapped between the two waterfronts after link-up in the HH_1ORD case. After 20 years of simulation (t(20)) both models are completely water saturated. Increasing the permeability contrast further, in the HH_2ORD case, the waterfronts gets increasingly uneven with higher degree of tortuosity. After 5 years of simulation (t(5)) the waterfronts are still separate, and does not link up before approximately 15 years into the simulation (t(15)), resulting in a zone of residual oil between the waterfronts. Thus, at all time steps for this model, there is more oil present in the models compared to HH_REF and HH_1ORD. The largest difference is observed in the HH_3ORD case, where the waterfronts are almost circular, and much less widespread compared to the other models. The waterfronts are separate throughout 20 years of simulation (t(20)), and large amounts of oil are still present in the model. The fluid fronts are irregular and highly disrupted by the presence of low-permeable deformation bands.
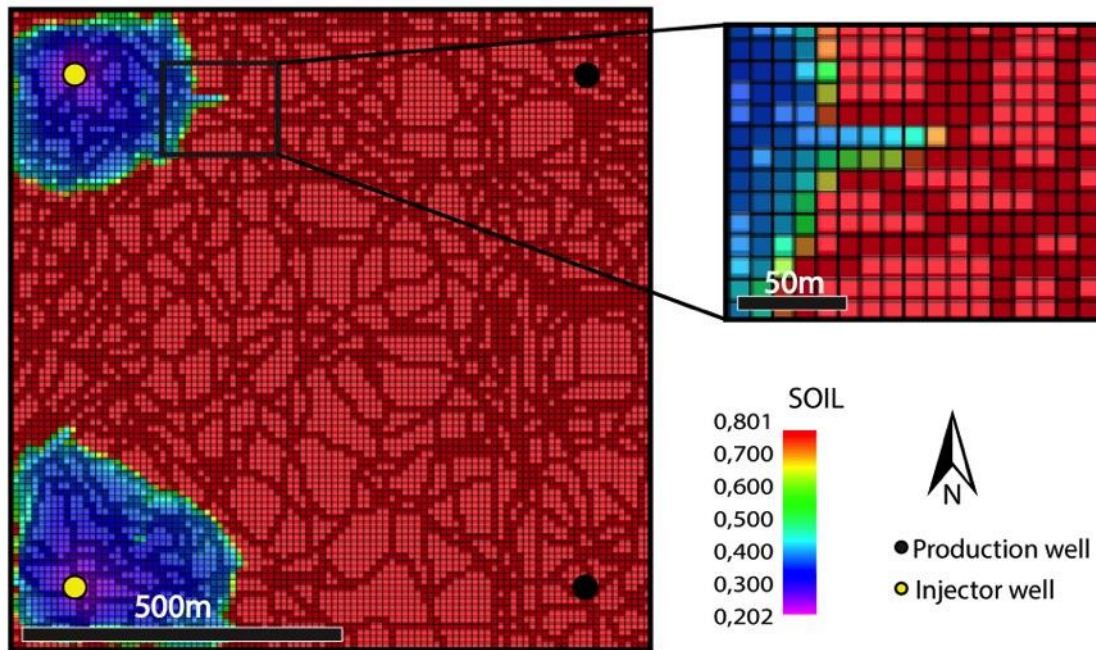
Figure 6.9: Illustration of how the fluid front is disrupted by the presence of very low permeable deformation bands in HH_3ROD case after 20 years of simulation (t(20); **Fig.6.8**). The deformation bands forms a complex orientation pattern, and are marked with black lines in the model. Note that the deformation band distribution in the northern part of the model is more complex and denser compared to the southern part.

6.3.3   Comparison of the HH-cases and LL-cases

A comparison of flow characteristics in the LL-cases and HH-cases is illustrated in Figure 6.10, where the host rock permeability is dissimilar: 150 mD and 1000 mD, respectively. In the reference cases (LL_REF and HH_REF), where deformation bands are absent, the water in the models migrates relatively fast. Nevertheless, the water migrates slower in the LL_REF case, as expected given the dissimilar permeabilities of the two models. After five years of simulation, the waterfronts within HH_REF have already linked-up, while the waterfronts in the LL_REF case link up after c. 15 years. Thus, there is more residual oil between the waterfront contacts in the LL_REF case. However, for both cases, the waterfront is smooth an even throughout the grid. The water uses 2.5 years to reach the production well is the HH_REF case and 16 years in the LL_REF case, consequently the water uses 13.5 more years to reach the production wells in the latter case (Compare HH_REF and LL_REF in Table 6.3 and Fig. 6.6).

In the models containing deformation bands (LL_1ORD and HH_1ORD), the permeability difference between host rock and deformation bands is c. 1 order of magnitude (Fig. 6.10). Nevertheless, the LL_1ORD case represents a low-permeable host rock scenario (i.e. 150

mD), while HH_1ORD represent a high-permeable host rock scenario (i.e. 1000 mD). As illustrated by Figure 6.10, the water migrates slower in the LL_1ORD case, and after 20 years, there is still no water break-through in the production wells. Oppositely, the water reaches the production wells within five years in the HH_1ORD case. Compared to the accompanying reference case (HH_REF), water break-through is delayed by 0.5 and 1.5 years in the SE and NE production wells, respectively (compare HH_REF and HH_1ORD in Table 6.3 and Fig. 6.6). Alternatively, water break-through in the LL_1ORD case is delayed by 10 and 15 years in the SE and NE wells, respectively (compare LL_REF and LL_1ORD in Table 6.3 and Fig. 6.6). Thus, the low-permeable host rock scenario (LL-cases) seems more sensitive to the occurrence of deformation bands with one order of magnitude reduced permeability, compared to the high-permeable host rock scenario (HH-cases). Nevertheless, similar for both cases is that the presence of deformation bands does not appear to have large effect on the water front, even though some minor irregularities are observed in both cases.
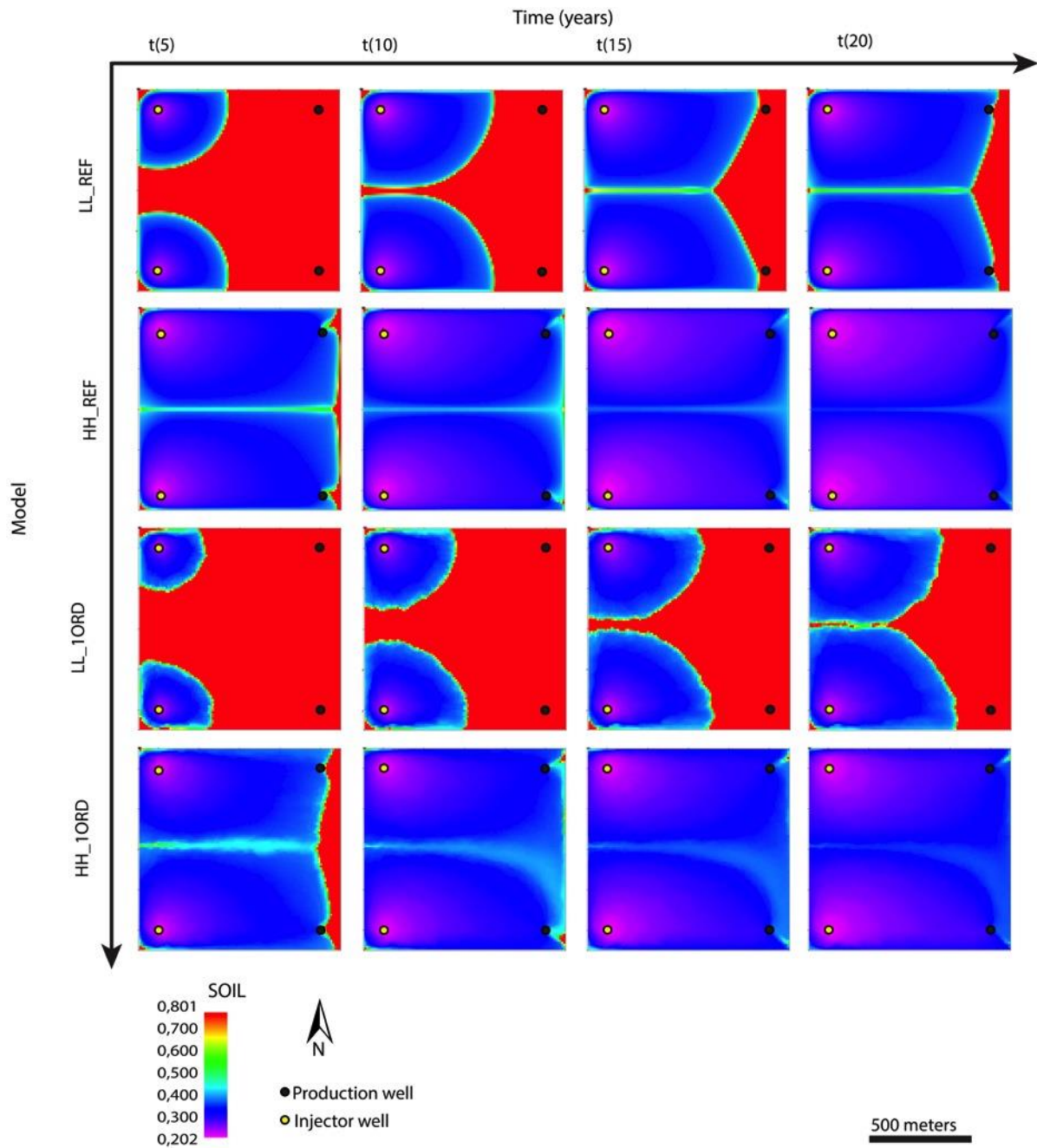
Figure 6.10: Comparison of flow characteristics at different time steps of the simulation in the low-permeable host rock cases (150mD; LL-cases) and high-permeable host rock cases (1000mD; HH-cases). In the reference cases (LL_REF and HH_REF), the water migrates slower across the grid in LL_REF model, not surprisingly given their dissimilar permeabilities. Thus, at all time steps the LL_REF case; there are large volumes of oil still present in the model. Regarding both cases, the waterfronts are smooth and even throughout the grid. Water break-through occurs simultaneously in the production wells after 2.5 years in the HH_REF case, and 16 years in the LL_REF case. In the models containing deformation bands (LL_1ORD and HH_1ORD), the permeability difference between host rock and deformation bands is *c*. 1 order of magnitude. The presence of deformation bands does not seem to have a significant effect on the waterfront, even though some minor irregularities is observed. As expected, the water migrates slower across the grid in the LL_1ORD case, and there are hence larger volumes of oil left in the model at the different time-steps. In the HH_1ORD case, water break-through occurs after 3 and 4 years in the southeastern and northwestern production wells respectively. While in the LL_1ORD case, the water reaches the production well in the southeast after 26 years, and the northeastern production well after 31 years. Thus, the presence of deformation bands causes more significant delay in water break-through time in the LL_1ORD case compared to HH_1ORD case.

6.3.4   Fluid flow summary

The main variable tested was the effect of varying orders of permeability reduction of deformation bands on fluid flow, in a low-permeable host rock scenario (LL-case) and a high-permeable host rock scenario (HH-case). Analyzed fluid flow aspects included variation in shape and speed of fluid fronts. Additionally, reservoir performance was analyzed using time to water break-through and oil saturation at the different time steps. With increasing contrast between deformation bands and host rock the following key observations were made:

- Increasing delay of water break-through in the production wells.
- Desynchronized water break-through in the two production wells.
- Perturbed waterfront.
- Delayed link-up of the waterfronts.
- Increasing degree of tortuosity and irregularities in the waterfronts.
- Low-permeable host rock cases (LL-case) are more sensitive to the presence of deformation bands (compared to HH-case), in terms of delayed water break-through in the production wells. The introduction of deformation bands with one order of magnitude permeability reduction relative to host rock, causes the water break-through to be delayed up to 15 years in the LL-case, whereas only 1.5 years in the HH-case (compared to the accompanying reference cases).

Thus, within the range of tested deformation band permeability values, fluid flow complexity increases when deformation band permeability is reduced.

7. Discussion

7.1 Introduction

The main aims of this study have been to better understand the impact of deformation bands on fluid flow in carbonate rocks and to improve the representation of deformation bands in geocellular reservoir models. In order to assess these aims, following aspects will be discussed: i) the effect of deformation bands on reservoir porosity and permeability distribution, ii) representation of deformation bands in reservoir models, and iii) the effect of deformation bands on fluid flow in reservoir models.

7.2 Effects of deformation bands on reservoir porosity and permeability

Generally for sedimentary rocks, the logarithm of permeability is often linearly proportional to porosity (Nelson 1994). However, for carbonate rocks, the porosity-permeability relationship tend to be more complex (e.g. Lønøy 2006). The undeformed grainstone of Middle Globigerina Limestone Member reveal very high porosity compared to permeability, i.e. 17-31% and 2.5-144 mD, respectively (Fig. 7.1 and Fig. 5.3). Similar values have been reported from carbonate grainstones in Antonellini et al. (2014) where the porosity is in the range of 17-27% and permeability between 26.5- and 265.3 mD (Fig. 7.1). Alternatively, with a host rock porosity of 22-35%, Rath et al. (2011) reported somewhat higher permeability values of host rock, ranging between 60-7976 mD (Fig. 7.1). The porosity-permeability relationship in carbonates is very complex due to the great variability in pore types, and because different pore types may have varying size and distribution (Choquette & Pray 1970, Lucia 1983, 1995, Lønøy 2006). Pore type is related to rock fabric, which is the result of spatially distributed depositional and diagenetic processes (Lucia 1983). Thus, large differences might be expected in the permeability with varying depositional environment and dominating diagenetic processes. Additionally, different methods used for porosity and permeability measurements are likely to differ to some extent. In particular minipermeameter values, as used for determining the permeability in Rath et al. (2011) and Antonellini et al. (2014). Compared to permeability estimates obtained from core plugs and image analysis, the minipermeameter usually overestimates the permeability (Fossen et al. 2011).

A major challenge in the evaluation of carbonate reservoirs is to understand the relationship between pore type and porosity and permeability (e.g. Lønøy 2006). The high porosity and

low permeability estimates obtained from core plugs within Middle Globigerina Limestone Member, can be explained by the porosity distribution as suggested by Lønøy (2006). The interparticle porosity (i.e. pore space occuring between grains; Choquette & Pray 1970) can be classified as either uniform or patchy. At similar porosities, a patchy porosity distribution yields a higher permeability than uniform porosity distribution. This is because the porosity is concentrated over a smaller volume and the pore system is better connected than for an correspondent, uniformly distributed pore volume (Lønøy 2006). Thus, even with high porosities, the permeability will be relatively small if the pore space is uniformly distributed. Additionally, intraparticle porosity (i.e. porosity occurring within grains) is characteristic for carbonates as this pore type typically is fauna dependent where the porosity is enclosed within skeleton walls (Choquette & Pray 1970). When determining porosity and permeability from image analysis, the intraparticle porosity within fossils might give a high porosity estimate, with low associated permeability if the pore space is not connected.

High porosity regions within the grainstones are preferred location for the deformation bands, as the presence of pore space allows for grain reorganization, repacking and compaction (e.g. Aydin 1978, Aydin & Johnson 1978, Fossen et al. 2007). The deformation bands reveal a porosity of 9-12%, corresponding to a porosity reduction of approximately 50% relative to the host rock (Fig. 7.1A). The decrease in porosity within the deformation bands results in a reduction in permeability of 0.038-3.2 mD, which are approximately two orders of magnitude less than the host rock (Fig. 7.1B). From helium porosimetry and image analysis, respectively, Rath et al. (2011) and Antonellini et al. (2014) measured a lower deformation band porosity than measured in this study, i.e. 2-5% (Fig. 7.1A). Moreover, Antonellini et al. (2014), reported a deformation band permeability one order of magnitude less than in the undeformed host rock (1.3-21.7 mD). This difference is significantly smaller than the differences measured by Rath et al. (2011), who documented a permeability reduction by as much as three orders of magnitude from the host rock to the deformation bands (0.2-10 mD; Fig.7.1B).

The magnitude of the permeability reduction within the bands is highly dependent on the deformation mechanism involved in the formation, as different mechanisms may produce deformation bands with different petrophysical properties (Fossen et al. 2007). In sandstones, the petrophysical properties of deformation bands and amount of cataclasis are interrelated (Ballas et al. 2012). Consequently, cataclastic bands reveal a larger decrease in porosity and permeability, compared to disaggregation bands, due to the changed grain-size distribution

caused by grain crushing (Fisher & Knipe 2001, Fossen et al. 2007). Additionally, dissolution and cementation might significantly increase the reduction of permeability and porosity caused by reorganization of grains and mechanical crushing (Ogilvie & Glover 2001). Because of the chemical reactivity of carbonate minerals, carbonate rocks are less resistant to chemical compaction and associated cementation, even at shallow depths (Ehrenberg & Nadeau 2005, Rath et al. 2011). Thus, the development of deformation bands in carbonate rocks are typically associated with dissolution- and cementation processes, where increasing degree of cementation during the generation deformation bands might, in turn, result in change of deformation mechanism, i.e. from grain rotation and compaction to cataclastic deformation (Rath et al. 2011, Cilona et al. 2012). However, as deformation mechanism typically change with burial depth, it is essential to examine petrophysical- and microstructural properties of cores for an accurate prediction of deformation structures and permeability characteristics in subsurface reservoirs (e.g. Fossen et al. 2007, Rotevatn et al. 2009b).

The fluid flow properties within a reservoir are controlled by the primary porosity and permeability characteristics, as well as several types of heterogeneities at different scales, including sedimentological, diagenetic and structural (e.g. Parnell et al. 2004). Deformation bands are potential flow barriers, and can have strong effects on the communication in porous reservoirs (e.g. Lothe et al. 2002). The overall low permeability of the Middle Globigerina Limestone Member becomes even lower with the presence of low-permeable deformation bands. Thus, production within such low-permeable reservoirs commonly depends on fractures, as reported in chalk reservoirs in the Oseberg field in the North Sea (Wennberg et al. 2013). Nevertheless, even though the deformation bands locally reduce the permeability within the Middle Globigerina Limestone Member, the effectiveness of deformation bands as flow baffles depends on other factors than the permeability contrast. In particular, number of bands (collective thickness), continuity, and the variation in permeability and porosity in three dimensions. Additionally, spatial distribution (e.g. connectivity) and orientation may influence the flow pattern during production and injection of fluids (e.g. Fossen et al. 2007). Factors affecting fluid flow will be further discussed in section 7.4.
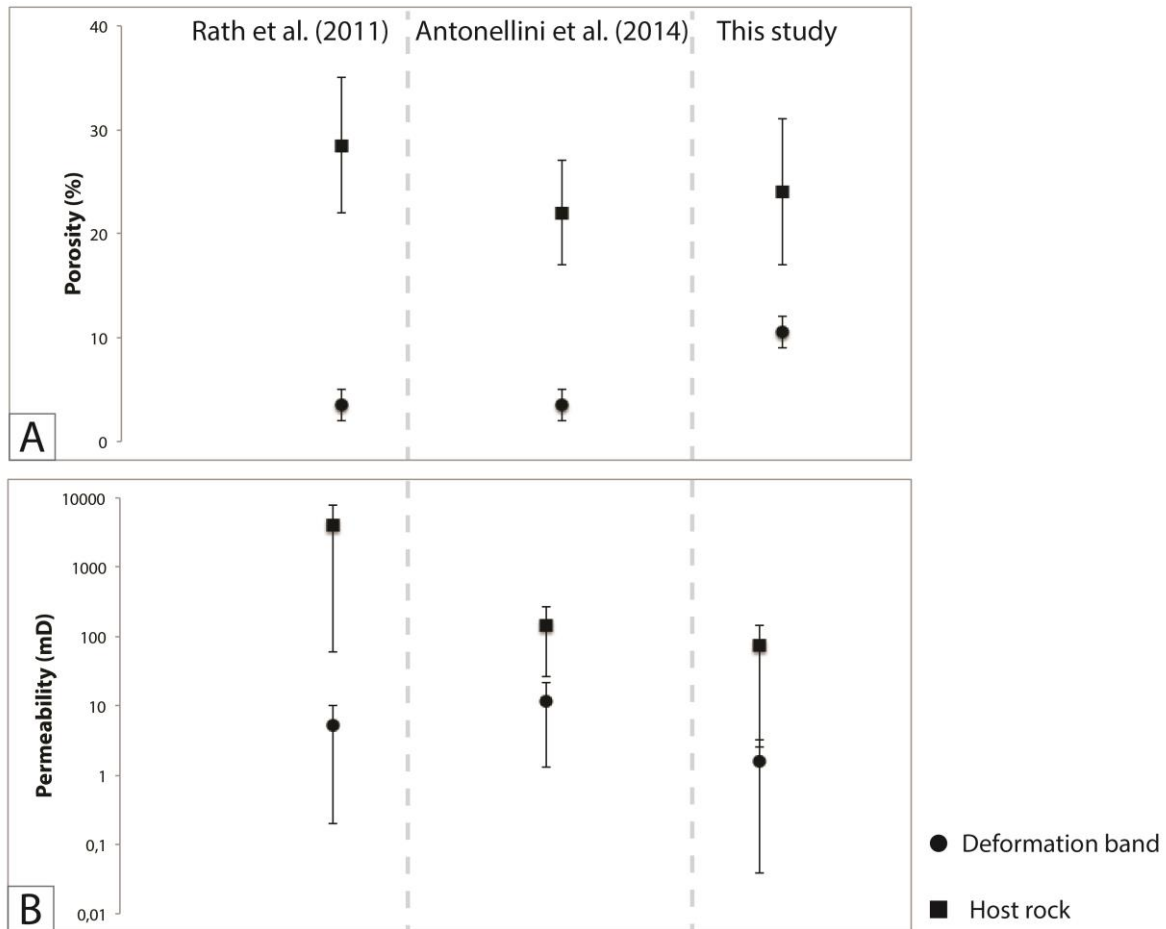
Figure 7.1: Comparison of the porosity and permeability values reported from Rath et al. (2011), Antonellini et al. (2014) and this study, for both deformation bands (circles) and the host rocks (squares). The circles/squares represent the mid-range values (i.e. max value+min value/2), while the line represent maximum and minimum values, giving the total range of measured porosities/permeabilites. A) Note the similarities in the host rock porosity (squares) between this study and Antonellini et al. (2014), whereas Rath et al. (2011) reported somewhat higher porosity values. In contrast, deformation band porosities (circles) reported from Rath et al. (2011) and Antonellini et al. (2014) show similar numbers, whereas deformation band porosity is higher in this study. B) Notice similarities in host rock permeability (squares) between this study and Antonellini et al. (2014); however, the lowest values from this study is one order of magnitude less than the lowest value in Antonellini et al. (2014). By comparison, Rath et al. (2011) reported fairly high host rock permeabilitites. Deformation band permeability (circles) in this study is approximately two orders of magnitude less than the host rock, whereas permeability values from Antonellini et al. (2014) is one order of magnitude less than the host rock. Alternatively, Rath et al. (2011) found a permeability reduction of three orders of magnitudes relative to host rock.

7.3 Representation of deformation bands in reservoir models

In general, deformation bands in extensional settings are found in the damage zone of larger offset faults, formed within porous granular rocks (Shipton & Cowie 2001, 2003, Fossen & Bale 2007). Thus, faults usually exhibit highly anisotropic flow properties, and capturing these effects is crucial for correct prediction of reservoir behavior during injection and production of fluids (Fachri et al. 2013a). In geocellular reservoir models, faults are generally

incorporated by transmissibility multipliers (e.g. Manzocchi et al. 2010). However, such an approach does not capture the fault zone permeability anisotropy very well (Manzocchi et al. 1999). Addressing this problem, a three dimensional approach have been conceptually proposed to the representation of faults in reservoir models (Tveranger et al. 2005, Braathen et al. 2009). Following this approach, fault zone architectural details can be implemented as tabular grids (i.e. fault facies). So far, fault facies modeling has primarily been focusing on siliciclastic reservoirs, even though roughly 50% of the world´s petroleum reservoirs are found in carbonates (Fredman et al. 2008). However, despite the differences in depositional mechanisms (i.e. allochthonous for sandstones versus autochthonous for carbonates; Ehrenberg & Nadeau 2005), fault deformation shows in many cases similarities between carbonates and siliciclastic rocks. Common elements observed in both cases include lenses, breccias, slip surfaces, cataclasis and deformation band development (e.g. Nøttveit 2005, Bonson et al. 2007). Nevertheless, adding such geological detail within conventional reservoir models is computationally expensive (Fachri et al. 2013a). Thus, in previous studies, small-scale heterogeneities such as deformation bands have been implicitly represented in geocellular models with upscaled permeabilities from analytical or numerical procedures (e.g. Jourde et al. 2002, Rotevatn et al. 2009b). This approach, however, has limitations with respect to fully resolve the orientation and distribution of deformation bands (Fachri et al. 2013a).

Addressing this problem, deformation bands in this study deformation bands have been implemented by employing an inflated deterministic approach. This method allows for deformation bands to be represented by semi-discrete means, keeping the ratios and relationships between observed structural sets and the structures in the model constant. The staged approach used in this study has several advantages. Firstly, such semi-discrete representation reproduces distribution and orientation trends of observed structural sets. In cases where deformation bands have a preferred orientation, fluid flow parallel to these structures would be easier than flowing across the structures (Fossen & Bale 2007, Fossen et al. 2007). Thus, an accurate representation of the geometry and orientation of such structures is of importance due to the possible effect they might have on flow pattern and reservoir sweep (Fossen & Bale 2007). Secondly, the approach allows for detailed investigation of local effect of deformation bands on fluid flow.

Fachri et al. (2013a) demonstrated the application of a deterministically constrained stochastic approach to representing small-scale structural heterogeneity in flow models. By employing fault facies as basic modeling element with high grid resolution (i.e. populating fault envelope grids with 3D geological objects; Tveranger et al. 2005, Braathen et al. 2009), a high-resolution relay zone model were built, explicitly including observed structural sets in terms of deformation band frequency. Further, they (Fachri et al. 2013a) compared the flow simulations of the stochastically generated models with the deterministic approach of the same relay zone presented in Rotevatn et al. (2009b), where the structural elements are represented implicitly, by means of upscaled permeabilities. The comparison of the two different modeling approaches revealed little or no effect on production for flow baffles with high permeability, whereas for medium- to low-permeable flow baffles (i.e. 10^3 to 10^5 magnitude orders permeability reduction relative to host rock), the choice of modeling approach has significant effects on simulated flow dynamics and production performance. Based these results (Fachri et al. 2013a), a fine-scaled modeling approach might better resolve detailed flow effects, giving a more realistic and accurate picture of the flow.

The modeling technique presented in the study herein, where deformation bands are represented semi-discretely, is likely to yield a more realistic understanding of the details of fluid flow and sweep-efficiency in reservoirs where small-scale flow baffles must be resolved. Even though the high grid resolution is beyond what is computationally feasible in conventional reservoir models, such approaches can be used for localized, detailed studies to complicated model zones where the effect of small-scale heterogeneities on fluid flow needs to be understood. Further, the results can be used for upscaling permeabilities to typical flow simulation scales with inexpensive computational costs, and further contribute to improved history matching, reservoir prediction and reservoir management (Garden et al. 2005, Soleng et al. 2007, Fachri et al. 2013a).

Detailed studies of deformation bands are constrained to outcrop studies. Given the small-scale nature of deformation bands, the detection of such structures are restricted by seismic resolution, which in turn makes their incorporation in reservoir models challenging (Zuluaga et al., *in review*). However, the prediction of deformation bands in subsurface reservoirs is feasible, by relating them to seismically mappable structures, by means of analogue field studies combined with a thorough understanding of the sedimentary geology of the reservoir. Additionally, where available, cores can provide spatially restricted information, which might

yield clues about the style of structural heterogeneities to be expected (Hesthammer & Fossen 2001, Zuluaga et al., *in review*). Thus, the use of analogues is essential for better understanding of specific reservoir types (Rotevatn et al. 2009a), and can provide more detailed information on continuity of flow zones and their connectivity, which is otherwise constrained in statistical (stochastic) models based on data attained from well logs (Matthäi et al. 1998).

7.4 Effect of deformation bands on fluid flow in carbonate reservoirs

In order to assess the dynamic effect of deformation bands on fluid flow, deformation bands have been implemented in a deterministic model by semi-discrete means, where the permeability contrast between deformation bands and host rock is the main variable tested (i.e. 10^1 to 10^3 orders of permeability contrast) within two scenarios: a low-permeable host rock case and a high-permeable host rock case.

7.4.1 Implications for fluid flow and sweep efficiency in hydrocarbon reservoirs

As implied by the current study, decreasing deformation band permeability increases the permeability heterogeneity in the models. This, in turn, makes the flow in the models more complex. The presence of low-permeability deformation bands in the models results in slower and more irregular waterfront propagation, compared to models where deformation bands are absent. The decreased speed of the waterfront from the injection wells thus delays the water break-through in the production wells. This agrees well with findings presented in Fachri et al. (2013a), where increasing permeability contrast between host rock and deformation bands caused fluid flow complexity reflected by variations in shape and speed of fluid fronts (which thereby delays water break-through).

The lateral sweep efficiency, i.e. the ability of injected water to saturate the model, is variable and largely affected by deformation band permeability. In the reference models with high permeability (i.e. 150 mD and 1000 mD) the water flows easily with smooth fluid fronts, due to the homogenous permeability field. This in turn results in good sweep efficiency throughout the model, as reflected by high water saturation at the end of the simulations (e.g. HH_REF and LL_REF; Fig. 6.10). There is good pressure communication between the wells, and the water takes a direct route to the production wells. However, when introducing deformation bands in the models, the waterfront gets perturbed due to the heterogeneous

permeability field. Since the deformation bands compose a complex and anastomosing pattern of low permeable barriers, cross-deformation band flow causes the fluid front to be uneven and irregular. With decreasing deformation band permeability, the fluid front gets progressively more irregular, with increasing tortuosity, resulting in a wide zone of residual oil confined between the waterfronts when they link up (Fig. 7.2). This zone of lower water saturation gets wider with decreasing deformation band permeability, and thus reflects local areas of poorer sweep efficiency (Compare HH_REF and HH_3ORD in Fig. 7.2), similar to the "shadow zones" of bypassed oil reported in Manzocchi et al. (2002). Contrastingly, as reported from both extensional settings (relay ramp; Rotevatn et al. 2009b) and contractional tectonic settings (fault propagation fold; Zuluaga et al., *in review*), increased flow tortuosity caused by low-permeable deformation bands resulted in better sweep efficiency, forcing the injection fluid places that would not be swept in a higher permeable case.

As illustrated by Rotevatn and Fossen (2011), low-permeable deformation bands can cause significant pressure compartmentalization, which in turn results in poor pressure communication between injection and production wells. On a large scale, such compartmentalization could impact the volume of moveable (produceable) oil or gas (Jolley et al. 2010). The results from the flow simulation herein show that even though complete blocking of fluid is not occurring, the models with progressively decreasing deformation band permeability experience slower lateral fluid flow migration which results in increasingly delayed water break-through. The most substantial delay is, as expected, when the deformation bands have three orders of magnitude permeability reduction relative to host rock (HH_3ORD; Fig. 6.6), causing the water break-through to be delayed up to 170.5 years compared to when deformation bands are absent. This indicates that the low-permeable deformation bands exercise a strict control on fluid flow across the grid, and the anastomosing pattern of deformation bands is very tight. However, significant water break-through delay is already observed when the deformation bands have 2 orders of permeability reduction relative to host rock (HH_2ORD), where water break-through is delayed up to 19.5 years compared to the undeformed simulated model. The slow migration of the water across the grid is reflected by the oil saturation results, which demonstrates how the water displaced the oil from the injector to the producer. At all time steps in the models containing deformation bands (LL_1ORD, HH_1ORD, HH_2ORD and HH_3ORD), there are larger amounts of oil in the deformation band models compared to the reference cases (LL_REF and HH_REF), as illustrated in Figure 6.5 and Figure 6.8.

Fossen and Bale (2007) suggested that the arrangement and orientation might have an effect on flow pattern and reservoir sweep. In every scenario in this study, where deformation bands are present, the southernmost production well is always the first to produce water. This can thus be explained by the complex spatial distribution and dense pattern of deformation bands in the northernmost part of the model (e.g. Fig. 6.9), causing water break-through delay of up to 60 years, compared to the southern situated production well (HH_3ORD). Nevertheless, the delayed water break-through results in prolonged production life. When looking at the end results when both production wells have achieved water break-through in all the simulated cases (Fig. 7.2), the delayed water break-through actually results in better sweep efficiency, as a slightly larger area in the eastern part of the models have been swept. In turn, this will have positive effect on the recovery rates. This is because the water has more time to sweep during the timespan between water break-through in the southern well and the later water break-through in the northern well.

In the published literature, there are some contradictory results regarding the practical effect of deformation bands on fluid flow. From the simulated geocellular relay model presented in Rotevatn et al. (2009b), they concluded that deformation bands must be of extremely low-permeability (more than three orders of magnitude permeability contrast) to significantly affect fluid flow. Alternatively, based on mathematical considerations, Fossen and Bale (2007) argued that uncommonly high permeability contrast (>4 orders of magnitude) and/or unusually high band concentrations are required for deformation bands to significantly affect the fluid flow in sandstone reservoirs. However, concerning permeability reduction within deformation bands, the term "orders of magnitude" is to some degree misleading when it is taken out of the context of the initial host rock permeability. As previously mentioned, the overall flow properties within a reservoir are controlled by the primary porosity and permeability characteristics, in addition to different types of heterogeneities, i.e. structural, diagenetic and sedimentological (Parnell et al. 2004). Thus, the development of deformation bands have been a matter of interest due to the possible effect they might have on fluid flow in otherwise excellent reservoirs. Nevertheless, if the permeability within a reservoir is initially poor, the presence of deformation bands might result in even poorer bulk permeability than primarily assumed. In terms of darcy units, one order of magnitude permeability reduction is not equivalent when comparing a high-permeable host rock case (i.e. 1000 mD, HH case) with a comparatively low-permeable host rock case (i.e. 150 mD,

LL-case). As shown in the current study, fluid flow within the low-permeable host rock containing deformation bands with one order of permeability reduction (LL_1ORD) is to a larger degree affected by the presence of deformation bands compared to the high permeable host rock case (HH_1ORD). This is reflected in the slower water migration across the grid, and thus water break-through time. In the LL_1ORD case, the occurrence of deformation bands results in water break-through delay of up to 15 years, compared to when deformation bands are absent. Contrastingly, water break-through is only delayed by maximum 1.5 years in the HH_1ORD case, relative to the accompanying undeformed model. Thus, since the initial host rock permeability is higher in the latter case, one order of permeability reduction within the deformation bands still results in fairly high bulk permeabilities throughout the model. These results indicate that deformation bands exercise a relatively stricter control on fluid flow, when the host rock is relatively low-permeable to start with. In other words, whereas previous authors (e.g. Fossen & Bale 2007, Rotevatn et al. 2009b) may be right that in initially high-permeable rocks, 3-4 magnitude-order reduction of permeability is necessary for deformation bands to significantly reduce flow, bands exhibiting only 1-2 magnitude-order permeability reductions may have a very significant effect in (initially) lower-permeable reservoir rocks. Accordingly, when evaluating the bulk permeability of reservoirs containing low-permeable deformation bands, one should carefully take into consideration the initial host rock permeability. Zuluaga at al. (in review) concluded that higher-permeable bands have smaller effect on flow and could probably be safely disregarded if the contrast to host rock is only 1-2 orders of magnitude. However, as shown in the current study, this is may not be the case if the host rock permeability is initially low.
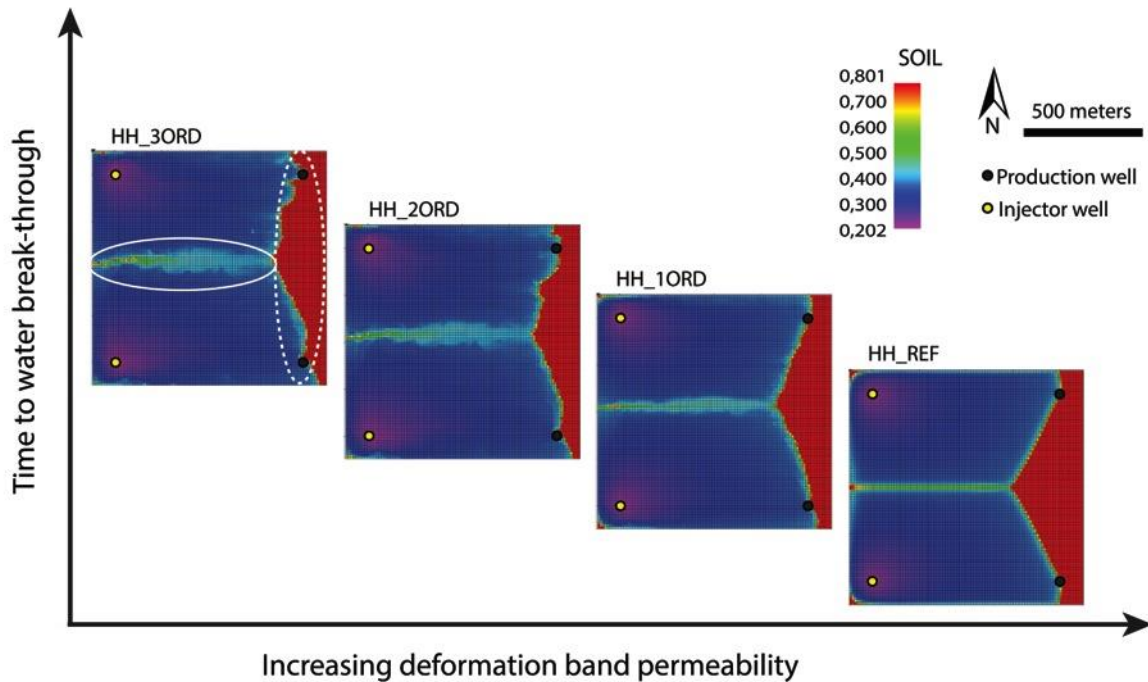
Figure 7.2: Conceptual diagram showing the high-permeable host rock case (i.e. 1000 mD, HH-case) with increasing deformation band permeability along the x-axis (i.e. 1 mD, HH_3ORD; 10 mD, HH_2ORD; 100 mD, HH_1ORD; 1000 mD, HH_REF) and time to water break-through along the y-axis. Decreasing deformation band permeability results in progressively increasing permeability heterogeneity in the models, as the permeability contrast between the host rock and deformation bands increases. This causes slower lateral water propagation, which in turn results in delayed water-break through. Additionally, decreasing deformation band permeability results in progressively more irregular waterfront and increased tortuosity. As illustrated by the white, continuous ellipse, the increased tortuosity causes residual oil to be trapped between the waterfronts when they link up. This zone of lower water saturation gets wider with increasing permeability contrast between the deformation bands and host rock (e.g. compare HH_1ORD and HH_3ORD). However, as the water break-through is desynchronized between the southern and northern production well, the water has more time to sweep in this interval from the initial water break-through in the southern well and final water break-through in the northern well. Thus, a larger area in the eastern model is swept in the cases where deformation bands are present (HH_1ORD, HH_2ORD and HH_3ORD), as illustrated by the withe, dashed ellipse. Note that even though the LL_1ORD case is not included in the figure, HH_REF & LL_REF, and HH_1ORD & LL_1ORD shows similar fluid flow characteristics (in terms of shape and swept area), respectively.

7.4.2 Deformation bands and well planning

The size of hydrocarbon accumulations is typically limited, and decision on well placement influence the risk of water coning and mixing of oil and water during production. Therefore, it is important to predict flow paths within the reservoirs, since they might control which parts of the reservoirs are bypassed by the flow and which regions are drained by the well over time (Matthäi et al. 1998). As previously mentioned in section 7.2, the spatial distribution and orientation of low-permeable deformation bands may influence the flow pattern during production and injection of fluids (Fossen et al. 2007). If the deformation bands have a preferred orientation they may change the flow pattern (Fossen et al. 2007). Sigda et al. (1999) reported that the presence of low-permeable deformation bands could act as

preferential groundwater flow path through the vadose zone. Hence, similar channelization can be envisaged during production of a petroleum reservoir (Fossen et al. 2007). In the current study, the deformation bands within Middle Globigerina Limestone Member are predominantly oriented ENE-WSW to NE-SW (Chapter 4; Fig. 4.9). If the study area was set in a subsurface petroleum reservoir, and the fluid prefer to flow parallel to these low-permeable structures rather than across (e.g. Antonellini et al. 1999, Fossen & Bale 2007, Fossen et al. 2007), the most optimal well placement would be with the injector situated in the WSW and producer in the ENE or contrariwise. In such scenario, the fluid could flow parallel to the deformation band orientation trend. However, flow pattern does not only depend on the orientation. The physical connectivity of deformation bands (i.e. the degree of intersecting bands) is an important factor, as it could undermine the effect of deformation bands as flow-reducing structures (Fossen et al. 2007). That is, if the deformation bands have are poorly connected, the fluid are free to flow around and between bands, thus, reducing their effect as flow barriers (Fossen & Bale 2007). Local areas within the Middle Globigerina Limestone Member reveal a larger spread in orientation trends, forming a highly connective and anastomosing pattern, as investigated in the study herein (Chapter 4; Fig. 4.5D). Thus, for the anastomosing pattern, deformation band connectivity acts to reduce the band-parallel flow, forcing the fluid to flow cross-band. This in turn resulted in significantly slower waterfront propagation and delayed water break-through, as discussed in section 7.4.1. Additionally, the frequencies of the deformation bands exercise an important control on the effective permeability, as illustrated by the harmonic average equation for the one-dimensional flow presented in Cardwell and Parsons (1945), eq. 6.1 described in Chapter 6. Here, the frequency, in terms of collective thickness is included in the calculations. Thus, high frequency of low-permeable deformation bands will reduce the effective permeability significantly, acting as efficient barriers to fluid flow. Deformation bands are commonly found in proximity to larger offset faults, and when planning a well in such locations, one should be aware of the possibility of high deformation band frequency (Fossen et al. 2005). The deformation band frequency within the Middle Globigerina Limestone Member (Fig. 4.11 and Fig. 4.10) varies along the measured profile, where the frequency is lowest in the middle part (i.e. from 110 to 260 meters along the profile). Since the deformation band frequency within this interval is generally low (i.e. averagely 2-4 deformation bands per meter), the fluid flow within this area would be less affected by the presence of deformation bands and unlikely to be of any concern.

Other simulation studies testing the effect of deformation bands on fluid flow (e.g. Rotevatn et al. 2009b, Fachri et al. 2013a, Zuluaga et al., *in review*), demonstrated that deformation bands with intermediately low permeabilities (i.e. $\geq 10^3$ orders permeability reduction relative to host rock) may have a positive effect on recovery by increasing the tortuosity of injection fluid and delaying water break-through in the production wells. Consequently, they further suggested that deformation bands might affect sweep efficiency positively, as the injected water flows more tortuously and sweep areas that would not otherwise be swept. Thus, on a large scale deformation bands might yield better production results in terms of total produced volumes and total recovery. Fossen and Bale (2007) stated that structural complications caused by sub-seismic faults are more likely to reduce hydrocarbon production. Hence, deformation bands might not contribute to the compartmentalization in the same manner as the large scale structures (e.g. Berg & Øian 2007). However, that being said, indications exist for the impact of low-permeability deformation bands on fluid flow in sandstone (Sternlof et al. 2004). For example, in the Ras Budran oil field in the Gulf of Suez (Egypt), cataclastic deformation bands in the Nubian Sandstone is thought to reduce well performance (Harper & Moftah 1985). Hesthammer et al. (2002) also suggested that post tectonic cementation of deformation bands might explain the low performance in the Gullfaks Sør reservoir situated in the North Sea. In addition, patterns of diagenetic alternation, indicative of paleofluid flow, in the Aztec Sandstone in southeastern Nevada (USA), demonstrate that deformation bands and deformation band arrays acted as baffles to flow at a variety of scales (Taylor & Pollard 2000, Eichhubl et al. 2004). Nevertheless, deformation bands are commonly ignored in the practice of reservoir management, even though their potential as low-permeable flow baffles rival those represented by depositional heterogeneities (Sternlof et al. 2004, and references therein), which, to date, have been incorporated into simulation more successfully and in higher detail than structural heterogeneities (Zuluaga et al., *in review*). Tyler and Finley (1988, 1992) reported that during hydrocarbon production, the ability to recover oil stored in a specific reservoirs decrease with increasing geological complexity. Thus, structural heterogeneities must be incorporated in reservoir simulation models in order to more accurately plan and predict fluid flow and production within a reservoir.

8. Conclusions

This study has attempted to improve the understanding of the effect of deformation bands on fluid flow in carbonate rocks and to improve the representation of deformation bands in geocellular reservoir models. This was done by means of reservoir modeling and fluid flow simulations of the outcrop example, in which deformation band permeability were the main variable tested for a high-permeable host rock case and a low-permeable host rock case. The constructed outcrop model included the collected outcrop and petrophysical data, supplemented by petrophysical data from the literature. From the work presented herein, the following conclusions are drawn:

- Image analysis and gas-transfer measurements of thin section and core plugs, respectively, document a decrease of porosity by 50% and a decrease of permeability up to two orders of magnitude within the deformation bands relative to the host rock.

- An inflated modeling approach, allows for a semi-discrete representation of deformation bands, successfully reproducing the observed structural sets and spatial distribution pattern. Such representation of structural heterogeneities permits for detailed investigation of fluid flow in reservoir zones where small-scale flow baffles must be resolved, and their effect on fluid flow needs to be understood.

- Increasing permeability contrast between host rock and deformation bands cause fluid flow complexity, reflected by variations in shape and propagation speed of fluid fronts. In turn, slower waterfront propagation delays water break-through in the production wells.

- The spatial distribution of the deformation bands exercise a strict control on the fluid flow, as reflected by desynchronized water break-through in the production wells.

- Within a high-permeable host rock (i.e. 1000 mD), deformation bands must feature two or more orders of magnitude permeability contrast relative to host rock to significantly affect fluid flow (in terms of water break-through delay). Limited effect is seen in the case with one order of permeability contrast.

- In a low-permeable host rock (i.e. 150 mD), deformation bands have significant effect on fluid flow even with one order of permeability reduction relative to host rock.

- When estimating the bulk permeability within a reservoir, initial host rock permeability deserves additional attention, as flow-reducing structures exercise a larger control on the effective permeability in initially lower-permeable host rocks.

- Deformation bands are commonly found in proximity to larger offset faults, and when planning a well in such locations, one should take into consideration that flow-reducing structural heterogeneity might exist. These structures must be incorporated in reservoir simulation models in order to more accurately plan and predict fluid flow and production.

9. Applicability, implications, limitations and future work

9.1 Applicability, implications and limitations

Understanding how geological heterogeneity and fluid flow interacts is important for the prediction of flow and optimization for production strategies. The semi-discrete modeling technique presented herein is applicable in scenarios where understanding the details of fluid flow and sweep efficiency in reservoir zones containing small-scale flow baffles needs to be resolved. The grid resolution and level of geological detail is beyond what is computationally reasonable in conventional field-scale reservoir models. However, the results may be used for localized, detailed studies of complex model zones, in cases where understanding the effect of small-scale reservoir heterogeneities is important. Furthermore, the results may be used for upscaling petrophysical properties in field-scale reservoir models, or to understand measured needed to stimulate production and sweep efficiency in complex reservoir zones. Although one should not directly apply the spatial distribution and orientation of deformation bands in this study, which are specific to the case studied herein, a similar approach may be applied to subsurface reservoirs based on input from core data and/or specifically suited analogue studies. Additionally, the local geological setting, such as mineralogy, composition, grain size, porosity and burial depth at time of deformation must be taken into account, as the presence of low-permeable sub-seismic structures is to a large extent controlled by these factors (Fossen et al. 2007). Local conditions may not favor the formation of deformation bands, and in low/non porous rocks, fractures generally form the prevailing deformation elements, which would result in an increase the overall porosity and permeability (Fossen et al. 2007). However, it is worth noting that porous carbonate reservoirs commonly encompass several heterogeneities at different scales (structural, sedimentological and diagenetic), thus all of these needs to be considered and their effect captured in reservoir models for successful prediction and management of fluid flow in subsurface reservoirs (Zuluaga et al., *in review*). Given the chemical reactivity of carbonate minerals, carbonate rocks are less resistant to chemical compaction and associated cementation (Ehrenberg & Nadeau 2005). Thus, one should use caution and be aware of the local factors, as dissolution and cementation might significantly increase the reduction of permeability and porosity caused by reorganization of grains and mechanical crushing (Ogilvie & Glover 2001).

In the literature, the majority of reported of deformation bands are limited to extensional settings (including the current study) where deformation bands tend to be localized in the vicinity of faults (e.g. Antonellini & Aydin 1995, Hesthammer & Fossen 2001, Rotevatn et al. 2009b, Rath et al. 2011). However, deformation bands can also occur in contractional tectonic settings, where they appear to be more widely distributed than in the extensional regime (Saillet & Wibberley, Solum et al. 2010, Klimczak et al. 2011, Brandenburg et al. 2012, Fossen & Rotevatn 2012, Soliva et al. 2013, Zuluaga et al., *in review*). Thus, one should be aware of the regional tectonic setting, as the distribution of deformation bands within a reservoir might be different in extensional settings and contractional tectonic settings.

It should also be mentioned that in this study the thickness of the deformation bands is, for simplicity, kept constant. In general, deformation bands are characterized by substantial thickness variations in three dimensions. Hence, the thickness variations might be of importance, as thickness minima may to some extent undermine the effect of deformation bands as flow-reducing structures, as asserted by some authors (Fossen & Bale 2007, Fossen et al. 2007, Torabi & Fossen 2009). Nevertheless, from fine-scale simulation, Rotevatn et al. (2013) tested this assertion and demonstrated that thickness variations have negligible effect, compared to the overall effect of the deformation band array on fluid flow and, thus, not necessary to account for in subsurface reservoir modeling.

Despite the note of cautions, the mapped and flow simulated example presented herein demonstrated an approach to understanding the effect of structural heterogeneity on local dynamic flow and may be applied to other settings if local factors and regional tectonic setting are taken into consideration.

9.2 Future work

In this study the reservoir sedimentology was modeled as homogenous for all cases instead of real or synthetic realistic stratigraphy. In a realistic setting, stratigraphic layers less prone to developing low-permeable deformation bands could represent conduits for flow, where fluids could bypass the deformation bands in other layers (e.g. Rotevatn et al. 2009a) . Such example would be the Lower Globigerina Limestone Member, comprising lower frequencies of deformation bands (Chapter 4; section 4.2.3), which could potentially provide conduit for flow. This was, however, omitted from the modeling herein, in order to isolate the effect of

deformation bands on fluid flow within the Middle Globigerina Limestone Member. Thus, the interplay between deformation band occurrence, stratigraphy and fluid flow is a desired subject for further modeling studies.

Additionally, as intrinsic host rock properties (i.e. grain size, grain shape, sorting, mineralogy and porosity) may vary laterally within a layer or from one layer to another, change in deformation band style might occur (Fossen et al. 2007). The amount of cataclasis seems to be an important control on porosity and related permeability reduction within deformation bands (Fossen et al. 2007, Ballas et al. 2012). Thus, it would be interesting to further investigate the interplay and effect of different types of deformation bands on fluid flow, e.g. disaggregation bands and cataclastic bands.

10. References

Alexander, D. 1988. A review of the physical geography of Malta and its significance for tectonic geomorphology. *Quaternary Science Reviews* **7**(1), 41-53.

Antonellini, M. & Aydin, A. 1994. Effect of faulting on fluid flow in porous sandstones: petrophysical properties. *AAPG bulletin* **78**(3), 355-377.

Antonellini, M. & Aydin, A. 1995. Effect of faulting on fluid flow in porous sandstones: geometry and spatial distribution. *AAPG bulletin* **79**(5), 642-670.

Antonellini, M., Aydin, A. & Orr, L. 1999. Outcrop aided characterization of a faulted hydrocarbon reservoir: Arroyo Grande Oil Field, California, USA. In: *Faults and subsurface fluid flow in the shallow crust* (edited by W. C. Haneberg, P. S. M., J. C. Moore, & L. B. Goodwin). American Geophysical Union, 7-26.

Antonellini, M., Petracchini, L., Billi, A. & Scrocca, D. 2014. First reported occurrence of deformation bands in a platform limestone, the Jurassic Calcare Massiccio Fm., northern Apennines, Italy. *Tectonophysics* **628**, 84-102.

Antonellini, M. A., Aydin, A. & Pollard, D. D. 1994. Microstructure of deformation bands in porous sandstones at Arches National Park, Utah. *Journal of structural geology* **16**(7), 941-959.

Argnani, A. 1990. The Strait of Sicily rift zone: foreland deformation related to the evolution of a back-arc basin. *Journal of Geodynamics* **12**(2), 311-331.

Argnani, A. & Bonazzi, C. 2005. Malta Escarpment fault zone offshore eastern Sicily: Pliocene‐Quaternary tectonic evolution based on new multichannel seismic data. *Tectonics* **24**(4).

Aydin, A. 1978. Small faults formed as deformation bands in sandstone. *Pure and Applied Geophysics* **116**(4-5), 913-930.

Aydin, A., Borja, R. I. & Eichhubl, P. 2006. Geological and mathematical framework for failure modes in granular rock. *Journal of Structural Geology* **28**(1), 83-98.

Aydin, A. & Johnson, A. M. 1978. Development of faults as zones of deformation bands and as slip surfaces in sandstone. In: *Rock Friction and Earthquake Prediction*. Springer, 931-942.

Aydin, A. & Johnson, A. M. 1983. Analysis of faulting in porous sandstones. *Journal of Structural Geology* **5**(1), 19-31.

Ballas, G., Soliva, R., Sizun, J.-P., Benedicto, A., Cavailhes, T. & Raynaud, S. 2012. The importance of the degree of cataclasis in shear bands for fluid flow in porous sandstone, Provence, France. *AAPG bulletin* **96**(11), 2167-2186.

Ballas, G., Soliva, R., Sizun, J.-P., Fossen, H., Benedicto, A. & Skurtveit, E. 2013. Shear-enhanced compaction bands formed at shallow burial conditions; implications for fluid flow (Provence, France). *Journal of Structural Geology* **47**, 3-15.

Baud, P., Schubnel, A. & Wong, T. f. 2000. Dilatancy, compaction, and failure mode in Solnhofen limestone. *Journal of Geophysical Research: Solid Earth (1978–2012)* **105**(B8), 19289-19303.

Baud, P., Vinciguerra, S., David, C., Cavallo, A., Walker, E. & Reuschlé, T. 2009. Compaction and failure in high porosity carbonates: Mechanical data and microstructural observations. In: *Rock Physics and Natural Hazards*. Springer, 869-898.

Berg, S. S. & Skar, T. 2005. Controls on damage zone asymmetry of a normal fault zone: outcrop analyses of a segment of the Moab fault, SE Utah. *Journal of Structural Geology* **27**(10), 1803-1822.

Berg, S. S. & Øian, E. 2007. Hierarchical approach for simulating fluid flow in normal fault zones. *Petroleum Geoscience* **13**(1), 25-35.

Bésuelle, P. 2001. Compacting and dilating shear bands in porous rock: Theoretical and experimental conditions. *Journal of Geophysical Research: Solid Earth (1978–2012)* **106**(B7), 13435-13442.

Bonson, C. G., Childs, C., Walsh, J. J., Schöpfer, M. P. & Carboni, V. 2007. Geometric and kinematic controls on the internal structure of a large normal fault in massive limestones: the Maghlaq Fault, Malta. *Journal of Structural Geology* **29**(2), 336-354.

Brandenburg, J., Alpak, F. O., Solum, J. G. & Naruk, S. J. 2012. A kinematic trishear model to predict deformation bands in a fault-propagation fold, East Kaibab monocline, Utah. *AAPG bulletin* **96**(1), 109-132.

Bryant, I., Carr, D., Cirilli, P., Drinkwater, N., McCormick, D., Tilke, P. & Thurmond, J. 2000. Use of 3D digital analogues as templates in reservoir modelling. *Petroleum Geoscience* **6**(3), 195-201.

Braathen, A., Tveranger, J., Fossen, H., Skar, T., Cardozo, N., Semshaug, S., Bastesen, E. & Sverdrup, E. 2009. Fault facies and its application to sandstone reservoirs. *AAPG bulletin* **93**(7), 891-917.

Cardwell, W. & Parsons, R. 1945. Average permeabilities of heterogeneous oil sands. *Transactions of the AIME* **160**(01), 34-42.

Carminati, E., Lustrino, M. & Doglioni, C. 2012. Geodynamic evolution of the central and western Mediterranean: Tectonics vs. igneous petrology constraints. *Tectonophysics* **579**, 173-192.

Casero, P. & Roure, F. 1994. Neogene deformations at the Sicilian–North African plate boundary. In: *Peri-Tethyan Platforms* (edited by Roure, F.). Editions Technip, Paris, 27-50.

Cashman, S. & Cashman, K. 2000. Cataclasis and deformation-band formation in unconsolidated marine terrace sand, Humboldt County, California. *Geology* **28**(2), 111-114.

Cavazza, W. & Wezel, F. C. 2003. The Mediterranean region-a geological primer. *Episodes* **26**(3), 160-168.

Cello, G., Crisci, G., Marabini, S. & Tortorici, L. 1985. Transtensive tectonics in the Strait of Sicily: structural and volcanological evidence from the island of Pantelleria. *Tectonics* **4**(3), 311-322.

Choquette, P. W. & Pray, L. C. 1970. Geologic nomenclature and classification of porosity in sedimentary carbonates. *AAPG bulletin* **54**(2), 207-250.

Cilona, A., Baud, P., Tondi, E., Agosta, F., Vinciguerra, S., Rustichelli, A. & Spiers, C. J. 2012. Deformation bands in porous carbonate grainstones: field and laboratory observations. *Journal of Structural Geology* **45**, 137-157.

Civile, D., Lodolo, E., Accettella, D., Geletti, R., Ben-Avraham, Z., Deponte, M., Facchin, L., Ramella, R. & Romeo, R. 2010. The Pantelleria graben (Sicily Channel, Central Mediterranean): an example of intraplate 'passive'rift. *Tectonophysics* **490**(3), 173-183.

Dart, C., Bosence, D. & McClay, K. 1993. Stratigraphy and structure of the Maltese graben system. *Journal of the Geological Society* **150**(6), 1153-1166.

Deng, S., Zuo, L., Aydin, A., Dvorkin, J. & Mukerji, T. 2015. Permeability characterization of natural compaction bands using core flooding experiments and three-dimensional image-based analysis: Comparing and contrasting the results from two different methods. *AAPG Bulletin* **99**(1), 27-49.

Dreyer, T., Fält, L. M., Høy, T., Knarud, R. & Cuevas, J. L. 1993. Sedimentary architecture of field analogues for reservoir information (SAFARI): a case study of the fluvial

Escanilla Formation, Spanish Pyrenees. In: *The geological modelling of hydrocarbon reservoirs and outcrop analogues* (edited by Flint, S. S., & Bryant, I.D.). Blackwell Publishing Ltd, Oxford, UK. , 57-80.

Du Bernard, X., Eichhubl, P. & Aydin, A. 2002. Dilation bands: A new form of localized failure in granular media. *Geophysical Research Letters* **29**(24), 29-1-29-4.

Dunham, R. J. 1962. Classification of carbonate rocks according to depositional textures. In: *Classification of Carbonate rocks* (edited by Ham, W.) **1**. American Association of Petroleum Geologist Memoir, 108-121.

Durlofsky, L. J. 2003. Upscaling of geocellular models for reservoir flow simulation: a review of recent progress. In: *7th International Forum on Reservoir Simulation* Citeseer, Bühl/Baden Germany, 23-27.

Ehrenberg, S. & Nadeau, P. 2005. Sandstone vs. carbonate petroleum reservoirs: A global perspective on porosity-depth and porosity-permeability relationships. *AAPG bulletin* **89**(4), 435-445.

Eichhubl, P., Hooker, J. N. & Laubach, S. E. 2010. Pure and shear-enhanced compaction bands in Aztec Sandstone. *Journal of Structural Geology* **32**(12), 1873-1886.

Eichhubl, P., Taylor, W. L., Pollard, D. D. & Aydin, A. 2004. Paleo-fluid flow and deformation in the Aztec Sandstone at the Valley of Fire, Nevada—Evidence for the coupling of hydrogeologic, diagenetic, and tectonic processes. *Geological Society of America Bulletin* **116**(9-10), 1120-1136.

Elter, P., Grasso, M., Parotto, M. & Vezzani, L. 2003. Structural setting of the Apennine-Maghrebian thrust belt. *Episodes* **26**(3), 205-211.

Embry, A. F. & Klovan, J. E. 1971. A Late Devonian reef tract on northeastern Banks Island, NWT. *Bulletin of Canadian Petroleum Geology* **19**(4), 730-781.

Enge, H. D., Buckley, S. J., Rotevatn, A. & Howell, J. A. 2007. From outcrop to reservoir simulation model: Workflow and procedures. *Geosphere* **3**(6), 469-490.

Enge, H. D. & Howell, J. A. 2010. Impact of deltaic clinothems on reservoir performance: Dynamic studies of reservoir analogs from the Ferron Sandstone Member and Panther Tongue, Utah. *AAPG bulletin* **94**(2), 139-161.

Exner, U. & Grasemann, B. 2010. Deformation bands in gravels: displacement gradients and heterogeneous strain. *Journal of the Geological Society* **167**(5), 905-913.

Fachri, M., Rotevatn, A. & Tveranger, J. 2013a. Fluid flow in relay zones revisited: Towards an improved representation of small-scale structural heterogeneities in flow models. *Marine and Petroleum Geology* **46**, 144-164.

Fachri, M., Tveranger, J., Braathen, A. & Schueller, S. 2013b. Sensitivity of fluid flow to deformation-band damage zone heterogeneities: A study using fault facies and truncated Gaussian simulation. *Journal of Structural Geology* **52**, 60-79.

Fachri, M., Tveranger, J., Cardozo, N. & Pettersen, O. 2011. The impact of fault envelope structure on fluid flow: A screening study using fault facies. *AAPG bulletin* **95**(4), 619-648.

Fisher, Q. & Knipe, R. 2001. The permeability of faults within siliciclastic petroleum reservoirs of the North Sea and Norwegian Continental Shelf. *Marine and Petroleum Geology* **18**(10), 1063-1081.

Florence, F., Rushing, J., Newsham, K. & Blasingame, T. 2007. Improved permeability prediction relations for low permeability sands. In: *SPE Rocky Mountain Oil and Gas Technology Symposium*. SPE 107954, Denver (USA), 16-18 April.

Fossen, H. 2010. *Structural geology*. Cambridge University Press, Cambridge, 463 pp.

Fossen, H. & Bale, A. 2007. Deformation bands and their influence on fluid flow. *AAPG bulletin* **91**(12), 1685-1700.

Fossen, H., Johansen, T. E. S., Hesthammer, J. & Rotevatn, A. 2005. Fault interaction in porous sandstone and implications for reservoir management; examples from southern Utah. *AAPG bulletin* **89**(12), 1593-1606.

Fossen, H. & Rotevatn, A. 2012. Characterization of deformation bands associated with normal and reverse stress states in the Navajo Sandstone, Utah: Discussion. *AAPG bulletin* **96**(5), 869-876.

Fossen, H., Schultz, R. A., Shipton, Z. K. & Mair, K. 2007. Deformation bands in sandstone: a review. *Journal of the Geological Society* **164**(4), 755-769.

Fossen, H., Schultz, R. A. & Torabi, A. 2011. Conditions and implications for compaction band formation in the Navajo Sandstone, Utah. *Journal of Structural Geology* **33**(10), 1477-1490.

Fredman, N., Tveranger, J., Cardozo, N., Braathen, A., Soleng, H., Roe, P., Skorstad, A. & Syversveen, A. R. 2008. Fault facies modeling: Technique and approach for 3-D conditioning and modeling of faulted grids. *AAPG bulletin* **92**(11), 1457-1478.

Föllmi, K., Gertsch, B., Renevey, J. P., De Kaenel, E. & Stille, P. 2008. Stratigraphy and sedimentology of phosphate‐rich sediments in Malta and south‐eastern Sicily (latest Oligocene to early Late Miocene). *Sedimentology* **55**(4), 1029-1051.

Garden, R., Mentiply, M., Cook, R. & Sylvester, I. 2005. Modelling fine-scale heterogeneity for optimal history matching from aeolian gas reservoirs, Neptune Field, UKCS. In: *Geological Society, London, Petroleum Geology Conference series* **6**. Geological Society of London, 695-706.

Gardiner, W., Grasso, M. & Sedgeley, D. 1995. Plio-pleistocene fault movement as evidence for mega-block kinematics within the Hyblean—Malta Plateau, Central Mediterranean. *Journal of geodynamics* **19**(1), 35-51.

Granath, J. W. & Casero, P. 2004. Tectonic setting of the petroleum systems of Sicily. In: Swennen, R., Roure, F., Granath, J.W. (Eds.), Deformation, fluid flow and reservoir appraisal in foreland fold-and-thrust belts: AAPG Hedberg Series, no. 1, pp. 391-411.

Grasso, M., Reuther, C.-D., Baumann, H. & Becker, A. 1986. Shallow crustal stress and neotectonic framework of the Malta Platform and the Southeastern Pantelleria Rift (Central Mediterranean). *Geol. Romana* **25**, 191-212.

Grove, C. & Jerram, D. A. 2011. jPOR: An ImageJ macro to quantify total optical porosity from blue-stained thin sections. *Computers & Geosciences* **37**(11), 1850-1859.

Gueguen, E., Doglioni, C. & Fernandez, M. 1998. On the post-25 Ma geodynamic evolution of the western Mediterranean. *Tectonophysics* **298**(1), 259-269.

Haldorsen, H. H. & Damsleth, E. 1990. Stochastic Modeling (includes associated papers 21255 and 21299). *Journal of Petroleum Technology* **42**(04), 404-412.

Harper, T. & Moftah, S. O. 1985. Skin Effect and Completion Options in the Ras Budran. *SPE* **13708**, 211-226.

Hesthammer, J., Bjorkum, P. A. & Watts, L. 2002. The effect of temperature on sealing capacity of faults in sandstone reservoirs: Examples from the Gullfaks and Gullfaks Sor fields, North Sea. *AAPG bulletin* **86**(10), 1733-1751.

Hesthammer, J. & Fossen, H. 2001. Structural core analysis from the Gullfaks area, northern North Sea. *Marine and Petroleum Geology* **18**(3), 411-439.

Illies, J. 1980. Form and formation of graben structures: the Maltese Islands. In: *Mobile Earth* (edited by Cloos, H., Von Gehen, K., Illies, J. H., Kuntz, E., Neuman, J. & Seibold, E.). Boppard, 161-84.

Illies, J. 1981. Graben formation—the Maltese Islands—a case history. *Tectonophysics* **73**(1), 151-168.

Jacobs, E., Weissert, H., Shields, G. & Stille, P. 1996. The Monterey event in the Mediterranean: A record from shelf sediments of Malta. *Paleoceanography* **11**(6), 717-728.

Jolley, S., Fisher, Q. & Ainsworth, R. 2010. Reservoir compartmentalization: an introduction. In: *Reservoir compartmentalization* (edited by Jolley, S. J., Fisher, Q. J., Ainsworth, R. B., Vrolijk, P. J., Delisle, S.) **347**. Geological Society, London, Special Publications, London, 1-8.

Jongsma, D., Van Hinte, J. E. & Woodside, J. M. 1985. Geologic structure and neotectonics of the North African continental margin south of Sicily. *Marine and petroleum Geology* **2**(2), 156-179.

Jongsma, D., Woodside, J., King, G. & Van Hinte, J. 1987. The Medina Wrench: a key to the kinematics of the central and eastern Mediterranean over the past 5 Ma. *Earth and planetary science letters* **82**(1), 87-106.

Jourde, H., Flodin, E. A., Aydin, A., Durlofsky, L. J. & Wen, X.-H. 2002. Computing permeability of fault zones in eolian sandstone from outcrop measurements. *AAPG bulletin* **86**(7), 1187-1200.

Kastens, K., Mascle, J., Auroux, C., Bonatti, E., Broglia, C., Channell, J., Curzi, P., Emeis, K.-C., Glaçon, G. & Hasegawa, S. 1988. ODP Leg 107 in the Tyrrhenian Sea: Insights into passive margin and back-arc basin evolution. *Geological Society of America Bulletin* **100**(7), 1140-1156.

Klimczak, C., Soliva, R., Schultz, R. A. & Chéry, J. 2011. Sequential growth of deformation bands in a multilayer sequence. *Journal of Geophysical Research: Solid Earth (1978–2012)* **116**(B9).

Klinkenberg, L. 1941. The permeability of porous media to liquids and gases. In: *Drilling and production practice*. American Petroleum Institute, 200-213.

Kolyukhin, D., Schueller, S., Espedal, M. S. & Fossen, H. 2010. Deformation band populations in fault damage zone—impact on fluid flow. *Computational Geosciences* **14**(2), 231-248.

Lehner, B. L. 1991. Neptunian dykes along a drowned carbonate platform margin: an indication for recurrent extensional tectonic activity? *Terra Nova* **3**(6), 593-602.

Lothe, A., Gabrielsen, R., Hagen, N. B. & Larsen, B. 2002. An experimental study of the texture of deformation bands: effects on the porosity and permeability of sandstones. *Petroleum Geoscience* **8**(3), 195-207.

Lucia, F. 1983. Petrophysical parameters estimated from visual descriptions of carbonate rocks: a field classification of carbonate pore space. *J. Pet. Technol.;(United States)* **35**(3).

Lucia, F. 1995. Rock-fabric/petrophysical classification of carbonate pore space for reservoir characterization. *AAPG bulletin* **79**(9), 1275-1300.

Lønøy, A. 2006. Making sense of carbonate pore systems. *AAPG bulletin* **90**(9), 1381-1405.

Mandl, G., De Jong, L. & Maltha, A. 1977. Shear zones in granular material. *Rock Mechanics* **9**(2-3), 95-144.

Manzocchi, T., Childs, C. & Walsh, J. 2010. Faults and fault properties in hydrocarbon flow models. *Geofluids* **10**(1‐2), 94-113.

Manzocchi, T., Heath, A., Walsh, J. & Childs, C. 2002. The representation of two phase fault-rock properties in flow simulation models. *Petroleum Geoscience* **8**(2), 119-132.

Manzocchi, T., Ringrose, P. & Underhill, J. 1998. Flow through fault systems in high-porosity sandstones. *Geological Society, London, Special Publications* **127**(1), 65-82.

Manzocchi, T., Walsh, J., Nell, P. & Yielding, G. 1999. Fault transmissibility multipliers for flow simulation models. *Petroleum Geoscience* **5**(1), 53-63.

Matthäi, S., Aydin, A., Pollard, D. & Roberts, S. 1998. Numerical simulation of departures from radial drawdown in a faulted sandstone reservoir with joints and deformation bands. *Geological Society, London, Special Publications* **147**(1), 157-191.

Mazzullo, S. 2004. Overview of porosity evolution in carbonate reservoirs. *Kansas Geological Society Bulletin* **79**(1-2), 20-28.

Micallef, A., Foglini, F., Le Bas, T., Angeletti, L., Maselli, V., Pasuto, A. & Taviani, M. 2013. The submerged paleolandscape of the Maltese Islands: Morphology, evolution and relation to Quaternary environmental change. *Marine Geology* **335**, 129-147.

Micarelli, L., Benedicto, A. & Wibberley, C. 2006. Structural evolution and permeability of normal fault zones in highly porous carbonate rocks. *Journal of Structural Geology* **28**(7), 1214-1227.

Missenard, Y., Bertrand, A., Vergély, P., Benedicto, A., Cushing, M.-E. & Rocher, M. 2014. Fracture-fluid relationships: implications for the sealing capacity of clay layers–Insights from field study of the Blue Clay formation, Maltese islands. *Bulletin de la Societe Geologique de France* **185**(1), 51-63.

Mollema, P. & Antonellini, M. 1996. Compaction bands: a structural analog for anti-mode I cracks in aeolian sandstone. *Tectonophysics* **267**(1), 209-228.

Morelli, C. 1985. Geophysical contribution to knowledge of the Mediterranean crust. In: *Geological evolution of the Mediterranean Basin* (edited by Stanley, D. J., Wezel, F. C.). Springer, New York, 65-82.

Murray, J. 1890. The Maltese Islands, with special reference to their geological structure: With geological map, two lithographic plates, and woodcuts. *The Scottish Geographical Magazine* **6**(9), 449-488.

Nelson, P. H. 1994. Permeability-porosity relationships in sedimentary rocks. *The log analyst* **35**(03), 38-62.

Nordahl, K., Ringrose, P. S. & Wen, R. 2005. Petrophysical characterization of a heterolithic tidal reservoir interval using a process-based modelling tool. *Petroleum Geoscience* **11**(1), 17-28.

Nøttveit, H. 2005. Fault zone modelling: A hierarchical approach for numerical modelling of fault structures, upscaling and flow simulation, M. Sc. thesis, University of Bergen, Bergen.

Ogilvie, S. R. & Glover, P. W. 2001. The petrophysical properties of deformation bands in relation to their microstructure. *Earth and Planetary Science Letters* **193**(1), 129-142.

Parnell, J., Watt, G. R., Middleton, D., Kelly, J. & Baron, M. 2004. Deformation band control on hydrocarbon migration. *Journal of Sedimentary Research* **74**(4), 552-560.

Pedley, H. 1978. *A new lithostratigraphical and palaeoenvironmental interpretation for the coralline limestone formations (Miocene) of the Maltese Islands*. HM Stationery Office.

Pedley, H. & Bennett, S. 1985. Phosphorites, hardgrounds and syndepositional solution subsidence: a palaeoenvironmental model from the Miocene of the Maltese Islands. *Sedimentary Geology* **45**(1), 1-34.

Pedley, H. M., House, M. R. & Waugh, B. 1976. The geology of Malta and Gozo. *Proceedings of the Geologists' Association* **87**(3), 325-341.

Pedley, H. M., House, M. R. & Waugh, B. 1978. The geology of the Pelagian block: the Maltese Islands. In: *The ocean basins and margins.* Springer, 417-433.

Pickup, G. E. & Hern, C. Y. 2002. The development of appropriate upscaling procedures. *Transport in porous media* **46**(2-3), 119-138.

Pringle, J., Howell, J., Hodgetts, D., Westerman, A. & Hodgson, D. 2006. Virtual outcrop models of petroleum reservoir analogues: a review of the current state-of-the-art. *First break* **24**(3).

Rath, A., Exner, U., Tschegg, C., Grasemann, B., Laner, R. & Draganits, E. 2011. Diagenetic control of deformation mechanisms in deformation bands in a carbonate grainstone. *AAPG bulletin* **95**(8), 1369-1381.

Rawling, G. C. & Goodwin, L. B. 2003. Cataclasis and particulate flow in faulted, poorly lithified sediments. *Journal of Structural Geology* **25**(3), 317-331.

Reuther, C.-D. & Eisbacher, G. 1985. Pantelleria Rift—crustal extension in a convergent intraplate setting. *Geologische Rundschau* **74**(3), 585-597.

Rosenbaum, G., Lister, G. S. & Duboz, C. 2002. Reconstruction of the tectonic evolution of the western Mediterranean since the Oligocene. *Journal of the Virtual Explorer* **8**, 107-130.

Rotevatn, A., Buckley, S. J., Howell, J. A. & Fossen, H. 2009a. Overlapping faults and their effect on fluid flow in different reservoir types: A LIDAR-based outcrop modeling and flow simulation study. *AAPG bulletin* **93**(3), 407-427.

Rotevatn, A. & Fossen, H. 2011. Simulating the effect of subseismic fault tails and process zones in a siliciclastic reservoir analogue: implications for aquifer support and trap definition. *Marine and Petroleum Geology* **28**(9), 1648-1662.

Rotevatn, A. & Fossen, H. 2012. Soft faults with hard tips: magnitude-order displacement gradient variations controlled by strain softening versus hardening; implications for fault scaling. *Journal of the Geological Society* **169**(2), 123-126.

Rotevatn, A., Fossen, H., Hesthammer, J., Aas, T. E. & Howell, J. A. 2007. Are relay ramps conduits for fluid flow? Structural analysis of a relay ramp in Arches National Park, Utah. *Special publication, geological society of London* **270**, 55.

Rotevatn, A., Sandve, T., Keilegavlen, E., Kolyukhin, D. & Fossen, H. 2013. Deformation bands and their impact on fluid flow in sandstone reservoirs: the role of natural thickness variations. *Geofluids* **13**(3), 359-371.

Rotevatn, A., Torabi, A., Fossen, H. & Braathen, A. 2008. Slipped deformation bands: a new type of cataclastic deformation bands in Western Sinai, Suez rift, Egypt. *Journal of Structural Geology* **30**(11), 1317-1331.

Rotevatn, A., Tveranger, J., Howell, J. & Fossen, H. 2009b. Dynamic investigation of the effect of a relay ramp on simulated fluid flow: geocellular modelling of the Delicate Arch Ramp, Utah. *Petroleum Geoscience* **15**(1), 45-58.

Rushing, J., Newsham, K., Lasswell, P., Cox, J. & Blasingame, T. 2004. Klinkenerg-corrected permeability measurements in tight gas sands: steady-state versus unsteady-state techniques. In: *SPE Annual Technical Conference and Exhibition*. Society of Petroleum Engineers.

Rustichelli, A., Tondi, E., Agosta, F., Cilona, A. & Giorgioni, M. 2012. Development and distribution of bed-parallel compaction bands and pressure solution seams in carbonates (Bolognano Formation, Majella Mountain, Italy). *Journal of Structural Geology* **37**, 181-199.

Saillet, E. & Wibberley, C. A. 2010. Evolution of cataclastic faulting in high-porosity sandstone, Bassin du Sud-Est, Provence, France. *Journal of Structural Geology* **32**(11), 1590-1608.

SEPM, S. 2013. Carbonate classification: http://www.sepmstrata.org/page.aspx?pageid=89, [Accessed 22.05.2014].

Shipton, Z. & Cowie, P. 2001. Damage zone and slip-surface evolution over μm to km scales in high-porosity Navajo sandstone, Utah. *Journal of Structural Geology* **23**(12), 1825-1844.

Shipton, Z. & Cowie, P. 2003. A conceptual model for the origin of fault damage zone structures in high-porosity sandstone. *Journal of Structural Geology* **25**(3), 333-344.

Sigda, J. M., Goodwin, L. B., Mozley, P. S. & Wilson, J. L. 1999. Permeability Alteration in Small‐Displacement Faults in Poorly Lithified Sediments: Rio Grande Rift, Central New Mexico. *Faults and Subsurface Fluid Flow in the Shallow Crust*, 51-68.

Soleng, H., Syversveen, A. R., Skorstad, A. & Tveranger, J. 2007. Flow through inhomogeneous fault zones. In: *Society of Petroleum Engineers Annual Technical Conference and Exhibition, SPE paper* **110331**.

Soliva, R., Schultz, R. A., Ballas, G., Taboada, A., Wibberley, C., Saillet, E. & Benedicto, A. 2013. A model of strain localization in porous sandstone as a function of tectonic setting, burial and material properties; new insight from Provence (southern France). *Journal of Structural Geology* **49**, 50-63.

Solum, J. G., Brandenburg, J., Naruk, S. J., Kostenko, O. V., Wilkins, S. J. & Schultz, R. A. 2010. Characterization of deformation bands associated with normal and reverse stress states in the Navajo Sandstone, Utah. *AAPG bulletin* **94**(9), 1453-1475.

Sternlof, K., Chapin, J., Pollard, D. & Durlofsky, L. 2004. Permeability effects of deformation band arrays in sandstone. *AAPG bulletin* **88**(9), 1315-1329.

Sternlof, K. R., Karimi‐Fard, M., Pollard, D. & Durlofsky, L. 2006. Flow and transport effects of compaction bands in sandstone at scales relevant to aquifer and reservoir management. *Water Resources Research* **42**(7).

Taylor, W. & Pollard, D. D. 2000. Estimation of in situ permeability of deformation bands in porous sandstone, Valley of Fire, Nevada. *Water Resources Research* **36**(9), 2595-2606.

Thorsheim, E. 2015. The geometry and evolution of deformation bands in carbonate grainstones along the Maghlaq Fault, Malta, M. Sc. thesis, University of Bergen, Bergen.

Tondi, E. 2007. Nucleation, development and petrophysical properties of faults in carbonate grainstones: evidence from the San Vito Lo Capo peninsula (Sicily, Italy). *Journal of Structural Geology* **29**(4), 614-628.

Tondi, E., Antonellini, M., Aydin, A., Marchegiani, L. & Cello, G. 2006. The role of deformation bands, stylolites and sheared stylolites in fault development in carbonate grainstones of Majella Mountain, Italy. *Journal of Structural Geology* **28**(3), 376-391.

Torabi, A. & Fossen, H. 2009. Spatial variation of microstructure and petrophysical properties along deformation bands in reservoir sandstones. *AAPG bulletin* **93**(7), 919-938.

Torabi, A., Fossen, H. & Alaei, B. 2008. Application of spatial correlation functions in permeability estimation of deformation bands in porous rocks. *Journal of Geophysical Research: Solid Earth (1978–2012)* **113**(B8).

Tveranger, J., Braathen, A., Skar, T. & Skauge, A. 2005. Centre for Integrated Petroleum Research–Research activities with emphasis on fluid flow in fault zones. *Norwegian Journal of Geology* **85**(1-2), 63-71.

Tyler, N. & Finley, R. J. 1988. Reservoir architecture-a critical element in extended conventional recovery of mobile oil in heterogeneous reservoirs. *AAPG Bulletin* **72**, 255.

Tyler, N. & Finley, R. J. 1992. Architectural controls on the recovery of hydrocarbons from sandstone reservoirs. In: *The Three-Dimensional Facies Architecture of Terrigenous Clastic Sediments, and its Implications for Hydrocarbon Discovery and Recovery* (edited by Miall, A. D., Tyler, N.) **3**. SEPM Concepts Models Sedimentol. Palaentol. , 1-5.

Vajdova, V., Baud, P. & Wong, T. f. 2004. Compaction, dilatancy, and failure in porous carbonate rocks. *Journal of Geophysical Research: Solid Earth (1978–2012)* **109**(B5).

Vanney, J.-R. & Gennesseaux, M. 1985. Mediterranean seafloor features: overview and assessment. In: *Geological evolution of the Mediterranean Basin* (edited by Stanley, D. J., Wezel, F. C.). Springer, New York, 3-32.

Wennberg, O. P., Casini, G., Jahanpanah, A., Lapponi, F., Ineson, J., Wall, B. G. & Gillespie, P. 2013. Deformation bands in chalk, examples from the Shetland Group of the Oseberg Field, North Sea, Norway. *Journal of Structural Geology* **56**, 103-117.

Zuluaga, L., Rotevatn, A., Keilegavlen, E. & Fossen, H., in review: Structural heterogeneity and fluid flow in porous sandstone reservoirs affected by contractional folding: a flow simulation study of the San Rafael Monocline, Utah (USA). *AAPG Bulletin*.

Appendix

Appendix I: Scanlines

Appendix II: Sample localities

Appendix III: Fault dip

Appendix I- Scanlines

Localities with scanlines are presented in this appendix for Lower and Middle Globigerina Limestone Member (LGLM and MGLM, respectively). Data collected for scanlines include primarily: GPS coordinates, deformation band frequencies (deformation bands per meter), deformation band orientations, deformation band thickness, and lithofacies. Additionally, standard deviation (frequency), average frequency and thickness were calculated for each scanline.
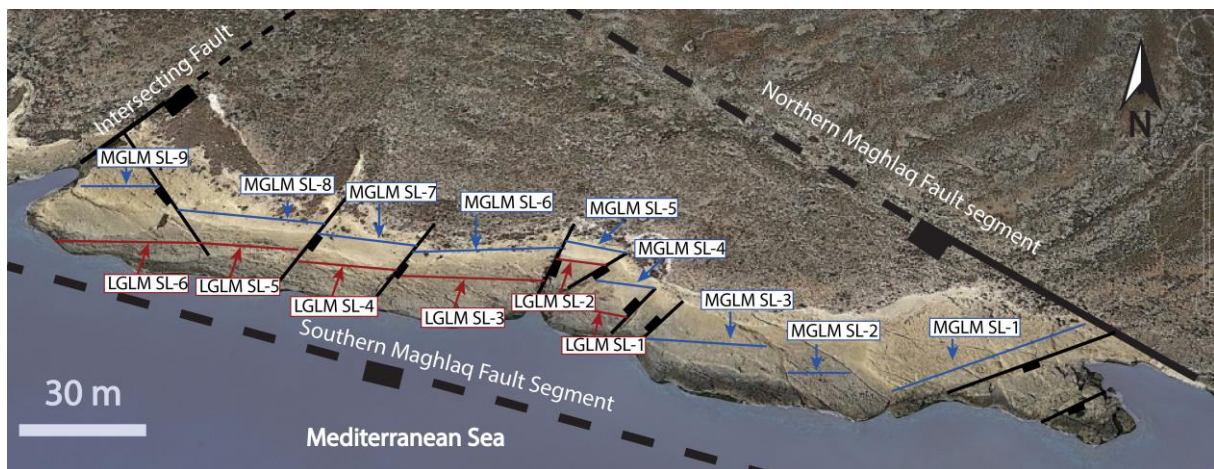
Figure A.1: Orientation of scanlines conducted within the Lower and Middle Globigerina Limestone Members denoted LGLM and MGLM, respectively. A total on nine scanlines were obtained from MGLM (MGLM SL1-9), whereas six scanlines from LGLM (LGLM SL1-6). The large fault trends are illustrated with black lines, stippled where conjectured.

Middle Globigerina Limestone Member scanlines

MGLM SL-1	Meter	Deformation band frequency (per meter)	Thickness (mm)	Orientation
GPS coordinates: From: N35° 49.193 E14° 27.007 To: N35° 49.189 E14° 26.962 Measured distance along profile: 0-54 meters. Facies: Grainstone.	0-1	-	-	-
	1-2	-	-	-
	2-3	1	5	086
	3-4	5	6,4,3	150,086
	4-5	6	5,3,5,5,4,3	078,160
	5-6	5	3,4,2,4	062,086,100
	6-7	4	6,5,2,3	074,078,040,090
	7-8	8	2,3,5,3,4,2	080,038,160,084,090,068
	8-9	6	10,4,1,3,4	080,084,092,066,004
	9-10	5	2,3,8,4,5	078,058,072,162
	10-11	3	5,5,3	054,060
	11-12	7	4,3,4,2,4	060,076,070,060,080,062
	12-13	9	5,4,4,4,3	030,078,064,130,168
	13-14	8	2,4,3,3,2,4	068,062,154,078,056,118
	14-15	8	3,3,1,2,3	075,086,068,056,150,070
	15-16	5	6,3,2	078,044,064
	16-17	7	4,3,7,2,4	060,078,068,088,148
	17-18	6	2,3,4,4,2,1	170,140,082,172,064,162
	18-19	6	2,2,3,5,3	066,140,168,164,080
	19-20	6	4,2,4,3,6	070,072,086,174,172
	20-21	5	2,2,5,4	050,070,178,088
	21-22	3	3,3,6	072,078,002
	22-23	6	3,3,5,3,3	058,080,040,112,168
	23-24	9	4,4,2,8,5,3,5	170,050,060,160,048,068,180
	24-25	7	2,1,2,2,3,4	028,064,070,078,172,152
	25-26	6	2,3,4,5,5,4	072,110,106,128
	26-27	5	1,2,3,7	068,158,012,070
	27-28	6	1,3,6,2,4	070,068,080,078,148
	28-29	5	3,2,6,3	080,094,084,038
	29-30	4	4,3,4	070,092,080
	30-31	4	2,3,2,3	074,088,084,068
	31-32	4	4,3,5	080,068,080
	32-33	4	3,3,5	082,062,070
	33-34	3	2,4,4	090,088,080
	34-35	4	2,2,5	080,068,096
	35-36	5	1,1,2,4,5	080,076,084,056,076
	36-37	6	2,13	082,076,068
	37-38	7	1,2,1,3,1,3	160,108,080,090,050,060
	38-39	3	2,1	070,080,072
	39-40	4	1,1,1,1	070,078,070,096
	40-41	2	4,3	078,090
	41-42	3	5,1,4	082,050,080
	42-43	8	2,2,2,2,1,1	080,060,080,020,046,180
	43-44	3	5,4,3	078,070,074
	44-45	3	2,2	160,080
	45-46	-	-	-
	46-47	-	-	-
	47-48	-	-	-
	48-49	4	2,3,3	068,064,066
	49-50	2	1,2	074,078
	50-51	2	2,2	070,080
	51-52	3	4,3,3	080,082,062
	52-53	5	3,1,3,2	060,070,050,058
	53-54	4	3,6	082,090,166
Average frequency and thickness		4.98	3.20	
STDAV.P (frequency)		1.90		

MGLM SL-2	Meter	Deformation band frequency (per meter)	Thickness (mm)	Orientation
GPS coordinates: From: N35° 49.194 E14° 26.956 To: N35° 49.199 E14° 26.937 Measured distance along profile: 54-69 meters. Facies: Grainstone.	0-1	8	4,2,6,2,2,1,12	048,063,056,052,054,060,070
	1-2	9	3,3,5,3,2,2,8,5	052,050,052,172,108,160,090,064
	2-3	7	3,4,5,5,3,2	032,108,080,072,102
	3-4	7	2,3,2,7,1,3	078,020,072,080,050,080
	4-5	7	4,2,5,3,3,1	078,050,082,080,080,120
	5-6	7	4,3,3,1,2,3,1	060,056,088,030,100,068,010
	6-7	8	2,3,5,2,4	040,094,072,012,088
	7-8	6	3,2,4,3,5,3	060,100,062,074,074,068
	8-9	6	5,2,3,6	080,060,072,124
	9-10	-	-	-
	10-11	5	4,3,5,5	058,080,090,100
	11-12	6	3,5,3	080,088,046
	12-13	8	1,1,3,2,3,5	060,068,180,050,050,080
	13-14	5	3,3,4	086,158,100
	14-15	5	5,5,3	094,064,086
Average frequency and thickness		6.71	3.40	
STDAV.P (frequency)		1.22		

MGLM SL-3	Meter	Deformation band frequency (per meter)	Thickness (mm)	Orientation
GPS coordinates: From: N35° 49.203 E14° 26.939 To: N35° 49.215 E14° 26.914 Measured distance along profile: 69- 105 meters. Facies: Grainstone.	0-1	10	4,13,1,3,4,3,4	040,080,110,040,080,074,060
	1-2	9	5,3,2,3	060,056,072,080
	2-3	5	2,4,4,3,2	070,070,040,080,056
	3-4	12	3,4,7,3,4	074,056,064,058,070
	4-5	12	1,1,3,3,4,1,4	140,108,072,072,084,078,144
	5-6	10	2,2,5,4,3	088,042,076,094,086
	6-7	9	3,5,2,3,15	098,084,080,076,148
	7-8	9	2,1,1,2,2,2	080,080,080,084,106,044,064,100
	8-9	8	4,3,5,40	080,084,078,076
	9-10	10	2,3,1,2,4,3,2,3,2	060,070,078,066,068,158,160,068,060
	10-11	9	4,9,3,4,5,2	078,076,092,060,109,058
	11-12	11	3,2,4,2,3,5,4	086,030,056,160,062,080,068
	12-13	11	3,2,4,5,3,4	078,080,086,074,064
	13-14	7	3,3,5,4,2,3	078,086,072,088,080
	14-15	8	3,2,5,2,1,4	080,146,068,090,180,100
	15-16	8	4,5,3,3,4,5	060,108,074,062,124,042
	16-17	8	3,2,3,2,2	050,062,074,142,082,072
	17-18	8	3,3,2,3,4,3	080,100,060,080,072,082
	18-19	7	2,2,4,1,3	080,042,098,080,088,074
	19-20	8	1,2,2,2,3,2,4	080,068,080,084,060,100,070
	20-21	9	2,2,3,1,8,1	054,066,058,108,150,178
	21-22	9	2,1,1,2,4,1,3	160,062,070,072,066,038,084
	22-23	8	4,4,2,3,3	058,146,052,064,056
	23-24	7	2,1,2,5,3,5	068,090,058,152,068,054
	24-25	10	1,4,3,6,2,4	158,104,070,084,068,080
	25-26	7	6,2,2,4,2,5	080,074,056,110,160,108
	26-27	12	2,3,2,2,6,5,4	008,054,078,090,080,068,076
	27-28	8	4,11,1,1,3,10,5	078,050,040,100,066,078,070
	28-29	10	4,1,2,4,1,2,3,2,3	076,072,132,068,170,084,060,030,078
	29-30	11	3,5,5,10,2,3,3	078,080,064,050,158,042,160
	30-31	11	3,2,3,2,4,3,1	080,064,064,102,072,062
	31-32	8	3,5,3,5,5,2	092,078,080,088,068,076
	32-33	11	4,3,3,2,3,2,1	086,046,080,020,078,050,120
	33-34	11	5,6,2,4,3	060,078,082,076,056
	34-35	9	1,2,3,2,3,1,5	098,096,060,086,066,074,060
	35-36	8	6,7,8,3	056,080,078,070,062
Average frequency and thickness		9.11	3.40	
STDAV.P (frequency)		1.65		

MGLM SL-4	Meter	Deformation band frequency (per meter)	Thickness (mm)	Orientation
GPS coordinates: From: N35° 49.218 E14° 26.918 To: N35° 49.221 E14° 26.912 Measured distance along profile: 105-113 meters. Facies: Grainstone.	0-1	8	2,2,3,2,1,2,3	156,058,070,078,180,050,062
	1-2	9	5,2,4,3,3,5	060,080,084,078,082,060
	2-3	8	3,2,4,2,2,2	074,174,050,086,180,090
	3-4	7	3,4,4,1,2,3	072,076,070,096,092,078
	4-5	7	3,2,2,4,4,2	084,062,082,060,072,082
	5-6	8	5,2,2,3,4,4	070,074,090,066,070,092
	6-7	7	2,2,4,2,5,2	084,072,058,070,078,076
	7-8	5	2,3,2,2	078,072,058,082
Average frequency and thickness		7.38	2.80	
STDAV.P (frequency)		1.11		

MGLM SL-5	Meter	Deformation band frequency (per meter)	Thickness (mm)	Orientation
GPS coordinates: From: N35° 49.227 E14° 26.914 To: N35° 49.232 E14° 26.902 Measured distance along profile: 113-131 meters. Facies: Grainstone.	0-1	-	-	-
	1-2	-	-	-
	2-3	-	-	-
	3-4	-	-	-
	4-5	-	-	-
	5-6	2	5,5	092,082
	6-7	1	4	084
	7-8	0	-	-
	8-9	2	6,5	062,078
	9-10	0	-	-
	10-11	0	-	-
	11-12	2	5,6	060,080
	12-13	2	6,6	084,080
	13-14	5	4,5,5,4,4	010,080,090,110,090
	14-15	1	3	074
	15-16	1	4	060
	16-17	4	3,3,2,5	080,060,100,092
	17-18	2	2,5	094,080
	18-19	3	2,4,5	090,086,074
Average frequency and thickness		1.69	4.40	
STDAV.P (frequency)		1.43		

MGLM SL-6	Meter	Deformation band frequency (per meter)	Thickness (mm)	Orientation
GPS coordinates: From: N35° 49.233 E14° 26.899 To: N35° 49.239 E14° 26.872 Measured distance along profile: 131- 179 meters. Facies: Grainstone.	0-1	3	3,4,5	090,086,074
	1-43	-	-	-
	43-44	4	3,4,2	112,052,072,062
	44-45	4	3,3,4,5	064,060,080,076
	45-46	1	3	154
	46-47	1	5	062
Average frequency and thickness		2.60	3.80	
STDAV.P (frequency)		1.36		

MGLM SL-7	Meter	Deformation band frequency (per meter)	Thickness (mm)	Orientation
MGLM SL-7 GPS coordinates: From: N35° 49.237 E14° 26.870 To: N35° 49.245 E14° 26.851 Measured distance along profile: 179-211 meters. Facies: Grainstone.	0-1	5	5,8,4,8,3	066,074,080,050,108
	1-2	8	5,4,2,4,4	108,088,092,086,056
	2-3	5	2,3,4,5	120,70,80,072/76,074/62
	3-4	3	2,3,3	068,062,066/84
	4-5	5	3,3,6,2	006,090,070,056
	5-6	1	3	070
	6-7	2	3,4	078,060
	7-8	3	5,4,3	062/64,060,065
	8-9	7	2,2,2,2,3,4	080,178,068,060,068,088
	9-10	5	4,2,2,3,3	064,068,068,104,086
	10-11	6	2,2,2,1,3	064,052,072,078,056
	11-12	6	3,4,10,3,3,4	172,166,070,070,100,080
	12-13	6	2,4,2,2,1,2	062,130,072,078,074,012
	13-14	6	2,2,2,2,3,3	082,066,068,060,080,090
	14-15	3	4,3,5	076,100,078
	15-16	6	2,2,2,4,1,3	046,082,044,084,070,074
	16-17	3	3,4,4	030,072,084
	17-18	2	2,3	090,064
	18-19	4	2,2,3,3	064,052,058,056
	19-20	2	4,5	072,078/64
	20-21	3	3,3,3	066,080,090
	21-22	5	2,3,3,5,5	090,080,082,078,052
	22-23	2	4,3	056,078
	23-24	2	3,2	062,062
	24-25	2	3,3	100,074/70
	25-26	4	3,2,5,3	094,104,046,088
	26-27	3	4,4,3	060,066,108
	27-28	1	4	040
	28-29	1	3	064
	29-30	4	3,5,3,3	084,066,078/86,082
	30-31	2	3,3	078,072
	31-32	3	3,5,3	064,070,064
Average frequency and thickness		3.75	3.20	
STDAV.P (frequency)		1.85		

MGLM SL-8	Meter	Deformation band frequency (per meter)	Thickness (mm)	Orientation
GPS coordinates: From: N35° 49.246 E14° 26.852 To: N35° 49.260 E14° 26.815 Measured distance along profile: 211-271 meters. Facies: Grainstone.	0-1	5	4,5,3,3	070,058,086,060
	1-2	5	-	-
	2-3	7	3,4,3,3,3,4	086,062,020,092,060,064
	3-4	7	-	-
	4-5	5	4,4,5,3,4	058,010,064,064,068
	5-6	5	-	-
	6-7	1	2	060
	7-8	1	-	-
	8-9	5	2,3,5	062,058,090
	9-10	5	-	-
	10-11	5	-	-
	11-12	1	4	064
	12-13	1	-	-
	13-14	0	-	-
	14-15	0	-	-
	15-16	2	3,4	068,048
	16-17	2	-	-
	17-18	2	4,3	058,074
	18-19	2	-	-
	19-20	3	2,2,3	064,082,054
	20-21	3	-	-
	21-22	1	2	066
	22-23	1	-	-
	23-24	1	5	078
	24-25	1	-	-
	25-26	3	4,3,3	040,058,060
	26-27	3	-	-
	27-28	1	4	072
	28-29	1	-	-
	29-30	2	4,6	068,056
	30-31	2	-	-
	31-32	1	3	060
	32-33	1	-	-
	33-34	1	3	040
	34-35	3	-	-
	35-36	5	4,3,5,5	062,050,080,052
	36-37	5	-	-
	37-38	2	3,3	052,056
	38-39	2	-	-
	39-40	3	6,5,3	070,076,070
	40-41	3	-	-
	41-42	3	3,3,3	054,078,076
	42-43	3	-	-
	43-44	5	3,5,3,3	082,068,062,060
	44-45	4	-	-
	45-46	3	3,3,3	062,064,070
	46-47	3	-	-
	47-48	2	3,4	054,056
	48-49	2	-	-
	49-50	1	4	064
	50-51	1	-	-
	51-52	3	5,5,5	040,068,058
	52-53	4	-	-
	53-54	3	4,3,3	048,064,064
	54-55	3	-	-
	55-56	5	2,4,3,3	060,080,058,050
	56-57	5	-	-
	57-58	4	3,2,2,2	068,060,062,054
	58-59	4	-	-
	59-60	3	4,5,3	070,066,100
Average frequency and thickness		2.83	3.5	
STDAV.P (frequency)		1.68		

MGLM SL-9	Meter	Deformation band frequency (per meter)	Thickness (mm)	Orientation
GPS coordinates: From: N35° 49.256 E14° 26.812 To: N35° 49.266 E14° 26.788 Measured distance along profile: 271-311 meters. Facies: Grainstone.	0-1	10	5,4,2,3,5,3	070,060,066,058,074,080
	1-2	8	4,5,3,3	070,080,084,046
	2-3	7	3,3,2,4,5	070,080,052,082,068/64
	3-4	9	2,3,1,1,5	060,078,074,068,066
	4-5	7	2,6,3,3	064,072,074,088
	5-6	7	8,7,3,3,2	060,066,048,072,030
	6-7	9	5,1,5,3	088,068,066,064
	7-8	8	3,4,2,3,3	068/72,070/70,100,060,076
	8-9	10	3,2,5,4,4	064,060,064,068,066
	9-10	7	5,4,3,4,4	056,040,080/64,070/60,086/82
	10-11	11	3,1,2,3,4	058,068,076,070,078
	11-12	8	4,4,3,4,12,2,3	050,068,058,070,070,060,060
	12-13	8	3,4,3,4	060,078,054,088
	13-14	10	4,2,2,10,5,2	062,086,060,00,170,050
	14-15	7	4,3,5,3	070,068,056,060
	15-16	6	4,4,4,3,5	080,046,076,030,080
	16-17	7	4,3,3,2	066,058,088,052
	17-18	8	2,2,3,2,3,2	090,052,054,064,050,080
	18-19	10	3,3,3,4,3,3	060,068,078,084,070,080
	19-20	6	1,3,7,3	046,070,072,066
	20-21	11	2,1,1,1,2,2,3	060,080,030,060,170,180,046
	21-22	8	3,3,4,5	054,072,078,080
	22-23	8	3,1,1,1,3,2	060,058,120,060,072,060
	23-24	7	3,3,2,2	080,052,060,058
	24-25	7	5,3,1,4,2	060,072,140,066,070
	25-26	8	3,3,2,10	064,044,060,070
	26-27	7	4,5,3,4,4	058,060,044,066,060
	27-28	7	2,1,3,2	058,060,044,066,060
	28-29	8	4,4,1,2,10	070,074,060,066,080
	29-30	5	2,2,5,5	086,058,072,080
	30-31	5	2,3,2,1,1	072,080,098,060,090
	31-32	7	2,1,3,2	066,110,052,092
	32-33	6	3,2,10,5,2	082,080,050,062,068
	33-34	6	2,8,4,3	090,080,066,072
	34-35	7	4,2,4,2,1	060,064,072,090,070
	35-36	7	2,4,3,2	082,084,068,078
	36-37	6	3,3,1,3,4,3	080,060,040,060,078,068
	37-38	6	2,2,3	058,052,086
	38-39	7	3,2,3,2,3	080,070,072,076,030
Average frequency and thickness		7.59	3.20	
STDAV.P (frequency)		1.48		

Lower Globigerina Limestone Member- scanlines

LGLM SL-1	Meter	Deformation band frequency (per meter)	Thickness (mm)	Orientation
GPS coordinates:	0-1	2	2,1	090, 056
From: N35° 49.214 E14° 26.912 To:	1-2	1	2	070
N35° 49.218 E14° 26.902	2-3	2	4,3	030, 010
Measured distance along profile:	3-4	2	3,3	180, 016
105-117 meters.	4-5	3	2,4,1	060,008,070
Facies: Grainstone.	5-6	1	1	040
	6-7	0	-	-
	7-8	2	2,1	068,100
	8-9	1	1	066
	9-10	3	4,2,2	178,042,018
	10-11	2	2,1	088,086
	11-12	2	3,4	078,078
Average frequency and thickness		1.75	2.28	
STDAV.P (frequency)		0.83		

LGLM SL-2	Meter	Deformation band frequency (per meter)	Thickness (mm)	Orientation
GPS coordinates:	0-1	1	1	080
From: N35° 49.225 E14° 26.909 To:	1-2	1	1	170
N35° 49.229 E14° 26.900	2-3	0	-	-
Measured distance along profile:	3-4	0	-	-
117- 130 meters.	4-5	0	-	-
Facies: Grainstone.	5-6	1	2	004
	6-7	0	-	-
	7-8	1	2	046
	8-9	-	-	-
	9-10	-	-	-
	10-11	-	-	-
	11-12	-	-	-
	12-13	-	-	-
Average frequency and thickness		0.50	1.60	
STDAV.P (frequency)		0.50		

LGLM SL-3	Meter	Deformation band frequency (per meter)	Thickness (mm)	Orientation
GPS coordinates: From: N35° 49.224 E14° 26.895 To: N35° 49.234 E14° 26.868 Measured distance along profile: 130-173 meters. Facies: Grainstone.	0-1	1	2	062
	1-2	1	-	-
	2-3	1	4	114
	3-4	1	-	-
	4-5	1	2	108
	5-6	1	-	-
	6-7	1	3	078
	7-8	1	-	-
	8-9	2	-	-
	9-10	2	2,5	044,110
	10-11	2	-	-
	11-12	2	10,1	086,074
	12-13	2	-	-
	13-14	2	2,5	140,120
	14-15	2	-	-
	15-16	1	7	124
	16-17	1	-	-
	17-18	2	4,5	142,118
	18-19	2	-	-
	19-20	0	-	-
	20-21	0	-	-
	21-22	2	10,5	134/70, 140
	22-23	2	-	-
	23-24	3	1,2,2	060,106,132
	24-25	3	-	-
	25-26	1	4	136
	26-27	1	-	-
	27-28	1	2	170
	28-29	1	-	-
	29-30	1	10	138
	30-31	1	-	-
	31-32	2	4,3	132,130
	32-33	2	-	-
	33-34	1	15	116/76
	34-35	0	-	-
	35-36	2	3,4	150,178
	36-37	1	-	-
	37-38	1	5	106/76
	38-39	1	-	-
	39-40	2	1,2	140
	40-41	2	-	-
	41-42	0	-	-
Average frequency and thickness		1.43	4.30	
STDAV.P (frequency)		0.70		

LGLM SL-4	Meter	Deformation band frequency (per meter)	Thickness (mm)	Orientation
GPS coordinates: From: N35° 49.233 E14° 26.865 To: N35° 49.242 E14° 26.847 Measured distance along profile: 173- 204 meters. Facies: Grainstone.	0-1	3	3,5,4	140,080,142
	1-2	2	-	-
	2-3	3	4,2,5	118,074,112
	3-4	2	-	-
	4-5	1	2	154
	5-6	1	-	-
	6-7	1	4	150
	7-8	1	-	-
	8-9	2	5,2	118/68,024
	9-10	2	-	-
	10-11	1	2	072
	11-12	1	-	-
	12-13	0	-	-
	13-14	0	-	-
	14-15	2	-	-
	15-16	3	-	-
	16-17	4	2,2,1,3	122,080/70,084,132
	17-18	3	-	-
	18-19	2	7,3	090,174
	19-20	2	-	-
	20-21	0	-	-
	21-22	1	-	-
	22-23	2	4,1	094,082
	23-24	1	-	-
	24-25	0	-	-
	25-26	0	-	-
	26-27	1	5	020
	27-28	1	-	-
	28-29	1	3	040
	29-30	1	-	-
	30-31	0	-	-
Average frequency and thickness		1.42	3.30	
STDAV.P (frequency)		0.40		

LGLM SL-5	Meter	Deformation band frequency (per meter)	Thickness (mm)	Orientation
GPS coordinates: From: N35° 49.243 E14° 26.848 To: N35° 49.254 E14° 26.821 Measured distance along profile: 204-253 meters. Facies: Grainstone.	0-1	0	-	-
	1-2	0	-	-
	2-3	0	-	-
	3-4	0	-	-
	4-5	0	-	-
	5-6	0	-	-
	6-7	0	-	-
	7-8	0	-	-
	8-9	0	-	-
	9-10	0	-	-
	10-11	0	-	-
	11-12	0	-	-
	12-13	2	6,1	074,092
	13-14	2	-	-
	14-15	1	2	086
	15-16	1	-	-
	16-17	1	3	104
	17-18	1	-	-
	18-19	2	4,2	104,080
	19-20	2	-	-
	20-21	1	5	090
	21-22	1	-	-
	22-23	0	-	-
	23-24	1	-	-
	24-25	3	1,3,2	084/66,052,048
	25-26	2	-	-
	26-27	1	4	098
	27-28	1	-	-
	28-29	1	2	108
	29-30	1	-	-
	30-31	3	1,1,3	054,058,044
	31-32	3	-	-
	32-33	2	2,1	080,060
	33-34	2	-	-
	34-35	1	2	116
	35-36	1	-	-
	36-37	1	2	064
	37-38	1	-	-
	38-39	1	1	032
	39-40	1	-	-
	40-41	0	-	-
	41-42	0	-	-
	42-43	2	2,1	070,108
	43-44	2	-	-
	44-45	3	1,2,2	058,038,076
	45-46	3	-	-
	46-47	2	4,3	130,118
	47-48	2	-	-
	48-49	4	7,2,2,2	076,140,070,104
Average frequency and thickness		1.57	2.42	
STDAV.P (frequency)		0.92		

LGLM SL-6	Meter	Deformation band frequency (per meter)	Thickness (mm)	Orientation
GPS coordinates: From: N35° 49.247 E14° 26.824 To: N35° 49.259 E14° 26.795 Measured distance along profile: 253-3 meters. Facies: Grainstone.	0-1	1	1	070
	1-2	2	-	-
	2-3	4	3,5,1,3	063,032,070,066
	3-4	3	-	-
	4-5	2	2,1	084,076
	5-6	2	-	-
	6-7	2	1,4	068,102/74
	7-8	2	-	-
	8-9	2	3,1	062,056
	9-10	2	-	-
	10-11	2	4,3	066,058
	11-12	2	-	-
	12-13	1	2	066
	13-14	1	-	-
	14-15	2	2,2	068,064/80
	15-16	2	-	-
	16-17	1	1	076
	17-18	1	-	-
	18-19	1	1	094
	19-20	1	-	-
	20-21	0	-	-
	21-22	1	-	-
	22-23	3	2,3,6	072,048,056
	23-24	2	-	-
	24-25	1	4	132
	25-26	1	-	-
	26-27	0	-	-
	27-28	0	-	-
	28-29	3	10,1,1	030,050,060
	29-30	2	-	-
	30-31	1	2	062
	31-32	1	-	-
	32-33	1	2	078
	33-34	1	-	-
	34-35	1	1	096
	35-36	1	-	-
	36-37	2	1,2	060/70,052/64
	37-38	2	-	-
	38-39	2	2,3	066,040/64
	39-40	2	-	-
	40-41	2	4,1	084,080
	41-42	3	-	-
	42-43	4	1,1,1,3	066,072/72,067,060
	43-44	3	-	-
	44-45	1	5	064
	45-46	1	-	-
	46-47	2	2,5	070,070/70
	47-48	2	-	-
	48-49	2	2,1	042,072
Average frequency and thickness		1.70	2.45	
STDAV.P (frequency)		0.81		

Table AI.1: Average, maximum and minimum thickness of measured deformation bands

	Average Thickness (mm)	Max. thickness (mm)	Min. thickness (mm)	Number of measurements
Lower Globigerina Lst Mbr.	2,9	15	1	146
Middle Globigerina Lst. Mbr.	3,3	40	1	948

Appendix II- Sample localities

Five of the samples collected in the field were used for drilling core plugs, and further used for determining the porosity and permeability by gas-transfer techniques. Additional a smaller sample (1B) was used for making polished thin section, determining the porosity and permeability using image analysis (ImageJ and MATLAB). GPS coordinates are presented in Table 2.1 and plug details in Table 2.2.

Table AII.1: Sample localities within the Middle Globigerina Limestone Member

Sample number (plugs)	GPS- Coordinates	Description
2	N35° 49.246 E14° 26.851	Host rock
11	N35° 49.193 E14° 27.000	Host rock
12	N35° 49.264 E14° 26.829	Host rock
16	N35° 49.196 E14° 27.001	Deformation band + host rock
37 (A & B)	N35° 49.201 E14° 26.935	Deformation band + host rock
Sample number (thin section)	GPS- Coordinates	Description
1B	N35° 49.264 E14° 26.829	Deformation band + host rock

Table AII.2: Plug details

Sample number	Plug length (cm)	Plug diameter (cm)	Pressure applied (bar)	Permeability (mD)	Porosity (%)
2	5.80	2.50	18	3.121	17.20
11	5.80	2.50	18	2.423	25.78
12	6.80	2.50	18	7.401	24.84
16	6.30	2.50	18	1.023	22.71
37A	7.00	2.50	18	1.746	19.76
37B	7.40	2.50	18	0.533	18.32

Appendix III- Fault dip

Table AIII.1: Average dip of the measured faults in the study area

Fault	Average dip (°)	Max (°)	Min (°)	Number of measurements
IBF1	60	72	47	54
IBF2	61	74	52	42
IBF3	55	64	47	37
IBF4	71	84	57	56
MF1	66	76	55	76